Ministry of Higher Education and Scientific Research

University of Baghdad

Institute of Laser for Postgraduate Studies

The Effect of Manipulating Working Parameters on the Efficiency of Laser Shock Peening for Aluminum Alloy6061-T6

A Thesis Submitted to the Institute of Laser for Postgraduate Studies, University of Baghdad in Partial Fulfillment of the Requirements for the Degree of Master of Science in Laser / Mechanical Engineering

BY

Ali Mohammed Khudair

B.Sc. Mechanical Engineering 2002

Supervisor

Asst. Prof. Dr. Furat Ibrahim Hussein

2022AD **1443 AH**

بِسْمِ اللَّهِ الرَّحْمَنِ الرَّحِيمِ

يَرْفَعِ اللَّهُ الَّذِينَ آمَنُوا مِنكُمْ وَالَّذِينَ أُوتُوا الْعِلْمَ
دَرَجَاتٍ ۚ وَاللَّهُ بِمَا تَعْمَلُونَ خَبِيرٌ

صدق الله العظيم

سورة المجادلة – الآية ١١

Certification

I certify that this thesis was prepared under my supervision at the Institute of Laser for Postgraduate Studies, University of Baghdad, as a partial fulfillment of requirements for the degree of:

"Master of Science in Laser \ Mechanical Engineering.".

Signature:
Name : **Dr. Furat Ibrahim Hussein**
Title : **Asst. Prof.**
Address : Mechatronics Engineering Department,
Al-Khawarizmi College of Engineering, University of Baghdad.
Date: / / 2022
(Supervisor)

In view of the available recommendation, I forward this thesis for debate by Examining Committee.

Signature:
Name : **Dr. Hanan Jaafar Taher**
Title : **Asst. Prof.**
Address : Head of the Scientific Committee,
Institute of Laser for Postgraduate Studies, University of Baghdad.
Date: / / 2022

Examination Committee Certification

We certify that we have read this thesis "The Effect of Manipulating Working Parameters on the Efficiency of Laser Shock Peening for Soft Metals" and as examining committee we examined the student in its content and in our opinion it is adequate with standards as a thesis for the degree of "Master of Science in Laser \ Mechanical Engineering".

Signature:
Name: Dr. Ziyad Ayad Taha
Title: Assistant Professor
Address: Institute of Laser for Postgraduate Studies, University of Baghdad.
Date: / / 2022
(Chairman)

Signature:
Name: Dr. Ahmed Riedh Abbas
Title: Assistant Professor
Address: Laser and Optoelectronic Eng. Dep., College of Engineering, Al-Nahrain University
Date: / / 2022
(Member)

Signature:
Name: Dr. Kareem Neamah Salloomi
Title: Lecturer
Address: Automated Manufacturing Engineering Department, Al-Khawarizmi College of Engineering, University of Baghdad.
Date: / / 2022
(Member)

Signature:
Name: Dr. Furat Ibrahim Hussein
Title: Assistant Professor
Address: Mechatronics Engineering Department, Al-Khawarizmi College of Engineering, University of Baghdad.
Date: / / 2022
(Supervisor)

Approved by the Deanship of Institute of Laser for Postgraduate Studies, University of Baghdad.

Signature:
Name: Prof. Dr. Hussein A. Jawad
Title: Dean
Institute of Laser for Postgraduate Studies, University of Baghdad.
Date: / / 2022

ACKNOWLEDGEMENT

I would like to acknowledge my supervisor ***Asst. Prof. Dr. Furat Ibrahim Hussein*** for his guidance and support in the development of this Dissertation. Without his support, this work would be impossible.

My sincere gratitude and great appreciation to ***Prof Dr. Hussein Ali Jawad*** Dean of Institute of Laser for Postgraduate Studies, University of Baghdad, for his great support and encouragement during the period of my work.

My deep appreciation and thanks go to ***Asst. Prof. Dr. Ziad Ayad Taha***, for his great assistance and encouragement to me.

I would like also gratefully acknowledge ***Prof. Abdul Hadi Al-Janabi*** for giving me the opportunity to join his lab and for his great efforts to provide me all the facilities. I am much indebted to him for his valuable assistance.

Eng. Atheer really deserves great thanks for his supporting and efforts during the most important stage of this work. I have deeply benefitted from his knowledge and advice.

I cannot end without once again thanking ***Asst. Prof. Dr Hanan Jaffar Tahir*** and ***Asst. Prof. Dr. Muhammad Kareem*** for their unflinching support and guidance, throughout the course of my study and research. I will always be grateful to them in every possible way. Last but not least I am also thankful to my friends and family for supporting me and encouraging me to obtain this degree.

ABSTRACT

Laser shock peening (LSP) is a cold work processing technique for surface treatment of materials in order to improve their characteristics such as fatigue resistance, wear, aberration resistance and corrosion. LSP founds their applications in different fields such as turbines, fans, compressor blades, aircraft some parts and in automobiles are treated as well. In LSP plastic deformation is imparted at the material surface to a certain depth due to laser matter interaction and many associated physical phenomena. In simple words, the material surface is covered with an ablative layer which in turn is covered with a transparent confinement layer. The intensive incident laser beam ablates the absorbing layer the radiation forming an expanded plasma plume confined by the transparent layer. As a result, the expanded plasma exerts a huge pressure on the material surface causing local plastic deformation and compressive residual stresses along the material section.

According to literature, many process parameters contribute to the quality of LSP such as laser power density, pulse duration, wavelength, pulse repetition rate, and spot geometry. The objective of the current study is to apply LSP technique on a soft thin sheets of Aluminum metal grade 6061-T6 in order to enhance its fatigue performance under cyclic loading.

The results of treated specimens with LSP show two grades of enhancement in the fatigue life represented by *noc* compared with the untreated specimens. The first grade can be considered normal for the most treated specimens at different sets of parameters were recorded an average increase in fatigue life of approximately 175%. The second grade of results appears for two groups of specimens where the increase in fatigue life is highly significant represented by the highest *noc* at *PRR* of 22.5 kHz, ω of 0.04 mm and at both *v*'s of 200 and 500 mm/sec. With these two mentioned sets of parameters, the

maximum percentage increase in the fatigue life is 505.25% when *v* equals 500 mm/s and 477.81% at 200 mm/s. These two groups show surface free defects when imaged with a scanning electron microscope (SEM). X-ray diffraction (XRD) analysis indicates a reduction in grains size, an increase of 28.56% in the lengths of dislocations, and the formation of effective compressive residual stress at the surface and beneath reaches to 700 μm.

Table of Contents

Chapter One: Introduction and Basic Concepts

Chapter Two: Materials and Methods

List of Abbreviations

3D	three-dimensional graphs
Adeq	Adequate Precision
Al	Aluminum
ANOVA	Analysis of variance test
BBD	Box–Behnken design
CW	Continuous Wave
DOE	design of experiments
EBSD	electron back-scattered diffraction
EDS	Energy-Dispersive Spectroscopy
GaAs	gallium arsenide
HAZ	heat affected area
HPDL	High Power Diode Lasers
LPB	Low Plasticity Burnishing
LSA	Laser assisted absorption
LSP	Laser shock peening
Nd:YAG	Neodymium Aluminum Garnet
noc	number of cycles
OFAT	one factor at a time
OV	overlap
SEM	Scanning electron microscope
SP	Shot peening
TEM	transmission electron microscopy
UIP	Ultrasonic Impact Peening
UTS	Ultimate tensile Strength
WJP	Water Jet Peening
XRD	X-ray diffraction

List of Symbols

σ_r	Residual stresses……....	*Mpa*
2θ	peak position……..	Rad
d	d-Spacing……..…….	nm
D	grain size……	nm
E_{pulse}	Pulse energy……...	*J*
E_{pulse}	pulse energy ……..	J
$FWHM$	Full width at half maximum……...…...	*rad*
I	Intensity ……	W/cm^2
N	number of overlapping spots for one joint spot….	n spots
OV	spots overlapping percentage…..……...	%
p	induced pressure……	*Mpa*
P_{av}	Average power …….	W
P_p	peak power ……...	kW
PRR	pulse repetition rate …….	Hz
PRT	pulse repetition time …….	s
v	scanning speed ……..	mm/s
Z	Reduced shock impedance…….	$kg/m^2.s$
λ	Wavelength …….....	nm
$\mu\varepsilon$	Strain…….	unit less
τ	pulse duration ……...	ms
ω	spot size ……	mm

Lists of Tables

Lists of Figures

Chapter One

Introduction and Basic Concepts

1.1 Overview

Engineered components have a wide range of uses in the environment around us, many of which are vital. These components are frequently subjected to different types of loading and stresses during regular operation and repetitive cyclic stress is one of them [1]. As a result, flaws and cracks initiate and spread across the section of the component resulting in sudden failure of the component [2]. Such breakdown which is due to fatigue stresses is sudden, unexpected, catastrophic, and occurs without pre-warning [3]. Mitigating fatigue failure in designed components is critical to ensure the overall safety of the element and lower the cost of component manufacturing and replacement [4]. It has been proven that the state of the surface for an engineering component has a significant impact on extending its fatigue life under cyclic loading. Surface defects are considered a fertile environment for cracks initiation and concentration and surface hardening is a crucial factor in disrupting their propagation [5]. In addition, introducing residual compressive stresses at the surface and beneath layers halts crack propagation and improves the performance under cyclic loading resulting in an increase in the lifetime of components [6]. This can be improved through many traditional and non-traditional techniques [7]. One of the latter techniques is the Laser shock peening process (LSP) in which the fatigue life can be improved by introducing residual stresses. In non-traditional techniques such as shot peening, the induced residual stresses caused in mild metals like aluminum alloys are limited in depth rarely exceeding 0.25 mm [8]. In addition, the process outcomes are accompanied by a major disadvantage, especially in softer metals, represented by yielding surfaces of high roughness after treatment [9]. For commercially aluminum alloys, LSP causes a higher residual stress depth of more than 1 mm and has been demonstrated to improve the fatigue performance of designed components [10, 11]. The surface quality of the peened component

is likewise minimally affected by LSP without noticeable thermal or surface condition changes at the surface as a result of the treatment procedure [12]. LSP has been adopted as a method for supporting the strength and lifetime of components that have been partially degrade in service owing to cracking, corrosion, or other defects [13]. The dislocation defects of partial fatigue damaged components may be effectively "healed" by LSP, hence prolonging the component's fatigue life. Engineered components are normally replaced after a pre-determined service time interval or when a fatigue crack is discovered [14]. This operation may be time-consuming and costly. To avoid expensive costs due to replacing of components LSP may be applied to the already tired components.

The current chapter introduces, in Sections 1.2 presents the and essential components the fiber laser. The fundamentals concepts of laser matter interaction are depicted in Section 1.3. Section 1.4 focuses on aluminum alloys properties and grades. The general mechanical properties of engineering materials are described in Section 1.5. The traditional and non-traditional surface treatment techniques were introduced in Section 1.6. The principles of laser shock peening technique in improving the performance of components are described in Section 1.7. Section 1.8 introduce a comparison of laser shock peening technique with the traditional conventional shot peening techniques. Section 1.9 depicts the advantages and disadvantages of laser shock peening. The process working parameters of laser shock peening process and their effects on the quality of the process are discussed in Section 1.10. Section 1.11 talks about the application of laser shock peening in industry and engineering applications. Section 1.12 gives theoretical description of experimentation techniques one factor at a time method (OFAT) and design of experiments (DOE).

1.2 Fiber Lasers

A fiber laser is considered an ideal type compact structured solid-state laser. It is characterized by excellent beam quality, reliability, large electrical and optical efficiencies and high peak power. As shown in Figure 1.1, an optical fiber of 1.1 µm diameter is used as a gain medium in which a specific wavelength is amplified [15]. The core, which has the highest refractive index, in the center of the fiber is doped with Ytterbium (Yb). As shown in Figure 1.6a the laser obtained inside the core by pumping light from a diode laser or a flash lamp into one end of the fiber. A highly reflective cladding surrounds the core with a usual diameter of 125 µm and a lower refraction index than the core [16]. Pump light also travels through the inner cladding that surrounds the core. Because of the two cladding layers, the inner cladding is encompassed by the outer cladding, resulting in a double-clad fiber [17].

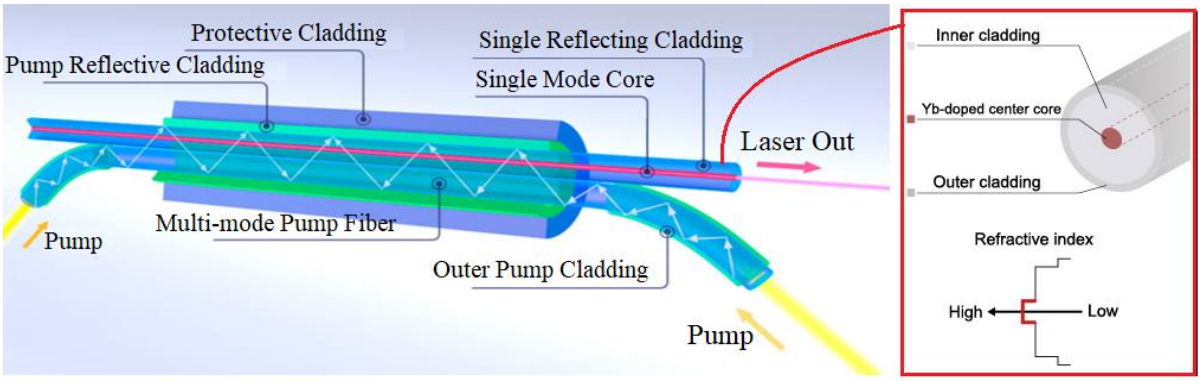

Figure 1.1: Generated laser in pumped fiber [17].

The doped fiber is often several meters long, resulting in a substantial surface-to-volume ratio that makes removing the generated heat simple. Single-fiber configurations may achieve laser outputs of up to 3 kW; however, power scaling can be done by coupling numerous fibers to a passive transport fiber with a larger core diameter [18]. This can enable laser outputs of up to 100 kW to achieve a wall-plug efficiency of up to 40%. This virtue of guidance also

allows the generated laser to have several results that can readily switch between fibers.

Table 1.1 presents a general comparison between a numbers of the widely used lasers in industrial applications.

Table 1.1: Comparison between four types of lasers system used in industry [4, 19, 20].

Property	CO_2	Nd: YAG Lamp Pumped	Nd: YAG Diode Pumped	Fiber Laser	diode Laser
λ- Wavelength (μm)	10.6	1.06		1.070	1.65
Laser Medium	CO^2 (gas)	Nd:YAG rod (solid)		Doped fiber	semiconductor
Pump Mechanism	Electrically excited gas discharge	Light		Light	electrical
Operating modes	continuous, pulsed, TEA	continuous, pulsed		Nano second pulse	continuous, pulsed
Typical applications	welding, drilling, heat treating	welding, drilling, trimming, marking		welding, drilling, trimming, marking LSP	fiber optic communications, barcode readers, laser pointers
η-Efficiency electrical/optical	5 – 10 %	1 – 3 %	10 – 12 %	20-30%	>60%
Max. Power (KW)	40	5		Up to 20	1.5–2
Average Power density	10^{6-8} W/cm^2	10^{5-7} W/cm^2	10^{6-9} W/cm^2	>1013 W/cm^2	950 W/cm^2
Beam Parameter Product No. (mm x mrad)	12 (Excellent)	25 – 45	12 (Excellent)	20	2
Beam guidance	Lenses and mirrors	Lenses, mirrors and optical fiber		Fiber, lens	Lenses glass
Lens material	Special glasses	Zinc selenite, gallium arsenide and germanium		glass	element glass

Fabrication and running cost	High	High	Moderate	Moderate	minimize cost

1.3 Laser Matter Interaction

1.3.1 Interaction with CW or Long Pulsed Laser

The interaction of light and matter provides the foundation for laser applications in materials processing. When a laser beam incident on a target, its energy absorbed by free electrons at the surface and then propagates through the electron-lattice subsystem. Later on, the absorbed energy transferred to the material bulk, as illustrated in Figure 1.2 [21].

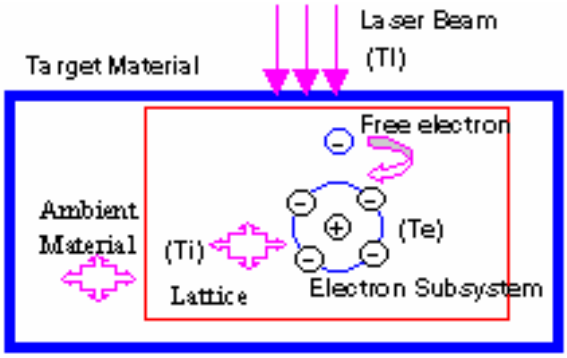

Figure1.2: Laser energy absorption by a target material [22].

Several physical processes and related the interactions take place during irradiation of an intense laser beam with a solid target as depicted in Figure 1.7. When an intensive Gaussian laser beam irradiated the surface absorption of optical energy starts. The absorbed energy accumulated at the surface then followed by thermal conduction allowing thermal energy to penetrate the bulk of the target (Figure 1.3a). When the surface reaches the melting temperature the material begins to evaporate (Figure 1.3b) as the irradiation continues and a hole begins to be drilled (Figure 1.3c). Absorption of laser by the blown material produces a hot dark plasma if the radiation is high enough. A

phenomenon known as a laser-assisted absorption (LSA) wave occurs when a hot dark plasma shields a target. The latter occurs noticed when the plasma that forms above the target travels backward along the beam path toward the laser accompanied with a loud noise and a dazzling flash of light (Figure 1.7d).

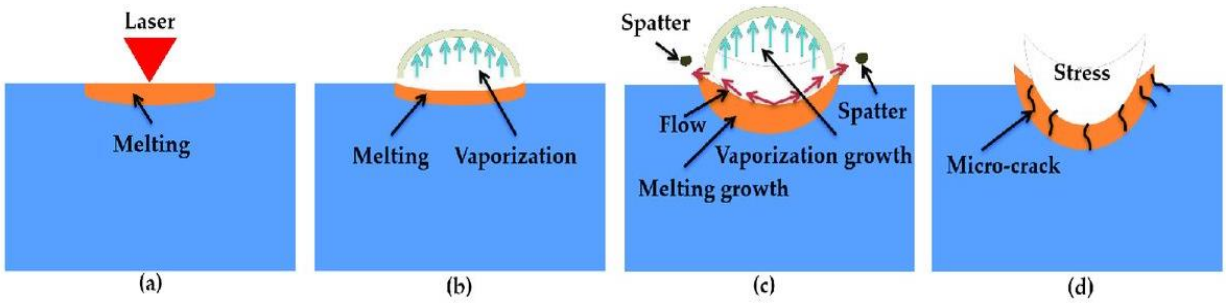

Figure 1.3: Schematic diagram for the interactions between an intense laser beam with a solid target [23].

1.3.2 Interaction with Intense Laser Short Pulses

Switching from CW or long pulsed lasers towards shorter pulsed laser beams such as nanosecond, picosecond and femtosecond change the nature of interaction with the matter [24]. In that case the associated physical processes and interaction differs moves from the thermal modes and became nonthermal. Even interaction with short pulsed lasers there is obvious difference in the interaction outcomes where it became highly athermal towards picosecond and more in femtosecond lasers [25]. The interaction nature between an intense laser pulse and target depends on type of the material and its related time scale. For metals, the energy exchange from optical to thermal occurs in a sharp period of 10^{-13}s. In nonmetals the process occurs in a range of 10^{-12}–10^{-6}s [26]. The manner of interaction depends on three-time scales namely: pulse width (τ), electron cooling time (t_e) and lattice heating time (t_l). Accordingly, the width of the laser pulse (nanosecond, picosecond or femtosecond) imposes the nature of interaction [24].

When a high fluence short width laser pulse incident on a material surface, different interactions may take place. Figure 1.4 shows that longer pulse

duration leads to more thermal effect on the target where after 1 ps the energy transformation from electron to lattice system and heat the interaction zone. Some thermodynamic processes, such as heat diffusion, fusion, and explosion, will take place after 10 ps. In longer laser pulses, after 1 ns, thermal heating and phase transformation can take place [24]. The pulse width has a direct relationship with heat penetration and ablation of materials. Processing with shorter pulses such as picosecond and femtosecond significantly reduces the dissipated heat inside the material resulting effective and more precise ablation as seen in Figure 1.5.

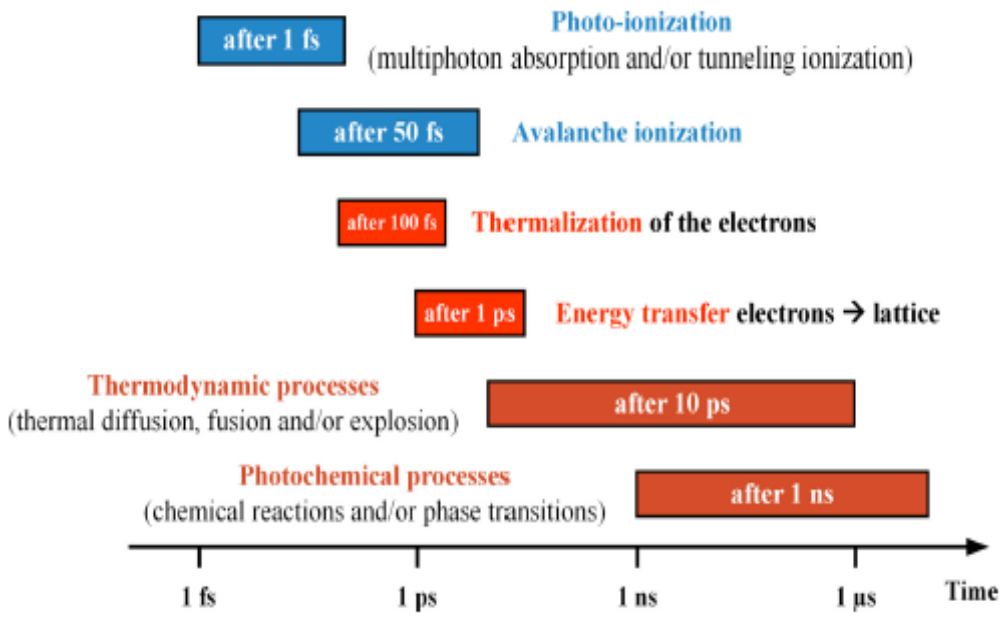

Figure 1.4: In interaction between laser and matter, different physical phenomena occur after time periods [24].

material interaction, modified

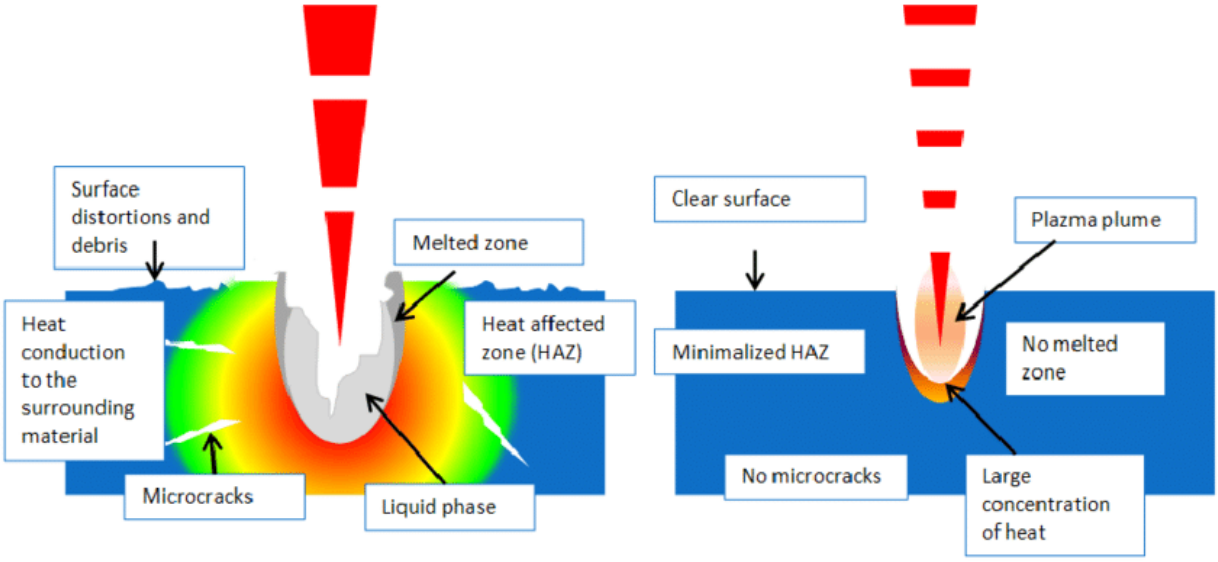

Figure 1.5: Interaction with Intense Laser Short Pulses [24].

1.4 Aluminum Alloys

Aluminum (Al) alloy alloys in which is the predominant metal is aluminum are characterized by the combinations of unique properties such as electrical and thermal conductivity, highly ductility, strength to weight ration and corrosion resistance [26]. These properties make Al and its alloys the most attractive, versatile and economical kind of metals for different engineering applications [27]. Al alloys occupy the second position in the structural applications after steels [28]. Under cyclic loading, aluminum alloys exhibit less fatigue life than steel alloys of similar strength and this is considered as Achilles's heel of such alloys [29]. Because of aluminum's lightweight and the development of aluminum fabrication methods, several industries are working to improve its mechanical qualities and use it as a substitute for steel in various applications. Alloying elements including copper, manganese, silicon, magnesium, and zinc are used to improve aluminum's mechanical qualities. Aluminum can be cast or wrought, and the addition of various primary alloying elements is classified into different series, as shown in Tables 1.2 [30].

Table 1.2 The main alloying element in the aluminum wrought alloy series [31].

Aluminum Alloy Series	Predominantly alloying element
1xxx	- cannot be heat treated therefore it is hardened by cold working to enhance the mechanical qualities. - contains at least 99% Al were considered commercially pure. - It has excellent corrosion resistance, electrical and thermal conductivity, and formability.
2xxx	- Cu is the most common alloying ingredient. - They can be heat treated and precipitation hardened for increasing strength. With yield strengths of up to 455 MPa, they offer exceptional strength at room and higher temperatures.
3xxx	- Mn is the main alloying element. - Strain hardening is used to increase strength. - They have medium strength and are very formable and corrosion-resistant. - its applications in architectural, beverage and food containers.
4xxx	- Si is the main alloying element. - They have a reasonable flow rate and a medium strength. - Commonly used for soldering and brazing because of their excellent flow properties.
5xxx	- Mg is the main alloying element. - Strain hardening is used to increase strength. - Have high corrosion resistance, strength, toughness, and weldability. When exposed to high temperatures for lengthy periods, they are vulnerable to intergranular assault. - Commonly utilized in marine applications.
6xxx	- Mg an Si are both important alloying constituents. - They have good extrudability, corrosion resistance, and strength. - Used in Architectural and automotive extrusion components.
7xxx	Zn is the primary alloying element. - They are mechanically bonded together and have exceptional strength and hardness.
8xxx	- Other elements that aren't addressed in other series are the main alloying elements. - They have high strength, hardness, and conductivity and can be heat treated.

1.5 Mechanical Properties

The mechanical properties are physical properties defines the behavior of a material or component when subjected to external loads. A broad spectrum of properties defines a material benefit to predict the material behavior in surface and the kind of predicted failure.

1.5.1 Properties Extracted from Tensile Test

Tensile tests are carried out for extracting important information about some characteristics that frequently needed during processing of materials with different techniques. Tensile test graph shown in Figure 1.6 reveals a number of important mechanical properties will be discussed below:

1. Elastic limit: Is the maximum stress exhibits elastic behavior where the material restores its dimensions without plastic deformation when the applied load is removed [32].

2. Modulus of elasticity (*E*): Also called Young's modulus, is the slope of the stress-strain curve in the elastic region which represents the stiffness or rigidity of a material whereby a material returns to its original dimensions and shape once the load is removed [33].

3. Yield Strength: Is the maximum stress can be applied before the material begins to distort plastically. Strain hardening occurs at this point due to plastic deformation resulting increase in the material strength [34].

4. Ultimate tensile Strength (UTS): Is the greatest stress a material can withstand when stretched under loading without fracture. Ultimate tensile strength is often referred as tensile strength tensile strength is a commonly used to describe the strength of metals and alloys. The associated elongation from the yield point and UTS is uniform [35].

5. Fracture Strength: Is the stress at which the material fails. Fracture strength is the ability of a material to withstand failure, and it is categorized according to the mode of applied stress, such as tensile, compressive, or bending [36]. The elongation between the UTS and fracture strength in no uniform and accompany by sever decrease in the cross-section.

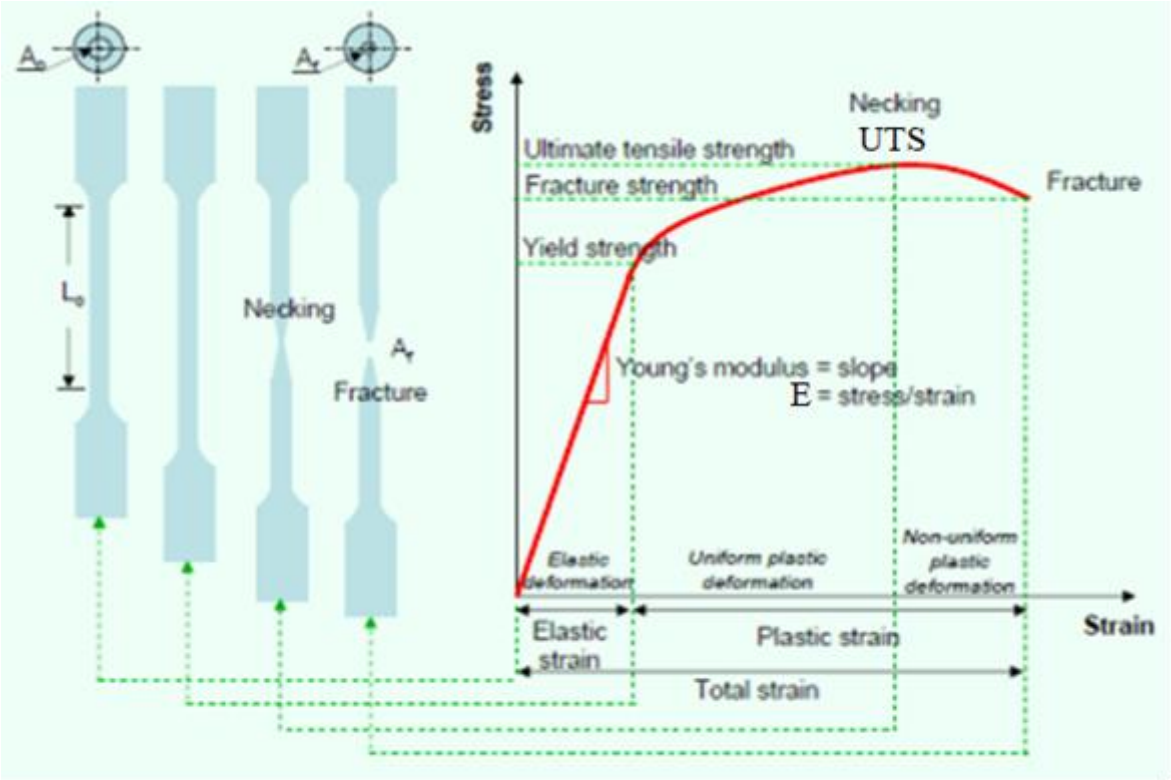

Figure 1.6: Stress-strain curve [38].

1.5.2 Hardness

Hardness describes a substance's resistance to permanent deformation such as abrasion, scratching and wear. Such tests are largely nondestructive and less time-consuming Today [37]. A variety of hardness tests are used, all of which involve pushing a specially dimensioned and loaded item, known as an indenter, into the being tested surface. The formed depth or size due to indenter penetration are used to determine a material's hardness. Rockwell is the hardness test that utilizes the depth of indenter penetration. Vickers, Knoop and

Brinell are examples of other tests that use the size of the indenter's impression [39]. Pyramid static indentations made with loads smaller than 1 kg are used in microhardness tests. The procedure is substantially the same as a standard Vickers hardness test is done on a much smaller scale using more precise instruments. For the surface being tested, a metallographic finish is normally required; the smaller the load used, the higher the surface polish required [40].

1.5.3 Fatigue

Fatigue failure of an engineering component happens due to microcracks formation and propagation when due to a repetitive or cyclical load. This kind of failure is considered catastrophic in engineering applications because it happens suddenly and is unpredictable especially when the applied stress is stilled much less than the strength of the material obtained from mechanical tests. Under cyclic loading cracks initiation and propagation are the two stages of fatigue cracking. The graph in Figure 1.7 shows the crack phases through the entire fatigue life of a designed component that may be considered as the time spent for a crack initiating, propagating and ending with rapid and catastrophic fracture. The critical crack length is the required length for rapid fracture [41].

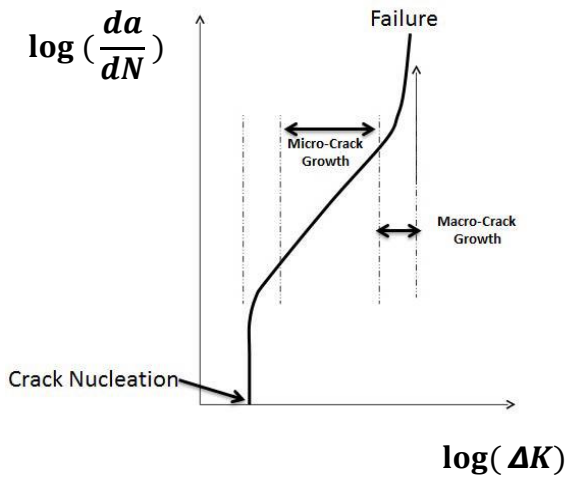

Figure 1.7: A crack phases through fatigue failure [41].

1.5.4 S-N Curves

An S-N curve is a logarithmic scales plot for the value of alternating stresses versus the number of cycles until failure. The relationship between the applied bending stress and the number of cycles is called Basquin's equation can be expressed as:

$$\sigma_f = A\, N_f^b \ldots\ldots\ldots\ldots\ldots (1.1)$$

where σ_f is the reversed stresses (MPa), A (MPa) and b are fitting coefficients related to bending strength in a static condition and N_f is the number of cycles until failure.

Fatigue testing with mild amplitudes is often stopped at 10^6 to 10^8 cycles. Curve A in Figure 1.8 is a typical S-N curve for a ferrous material. Testing in this area takes a long time, and the S-N curves frequently approach a constant value called the endurance limit as seen. Endurance limit is expresses as the stress below which a component can bear an infinite number of repeated load cycles without cracking or failure [42]. The endurance limitations of several non-ferrous metals and alloys, such as aluminum, magnesium, and copper, are not well characterized as Curve B implies, these materials have a constantly declining S-N response. In such instances, a fatigue strength for a specific number of cycles must be specified. The stress that produces failure at 1×10^8 or 5×10^8 loading cycles is commonly used to determine a practical fatigue life for certain materials [43].

Most fatigue tests use cyclic bending to apply alternate tensile and compressive pressures. The mean stress in this scenario is zero. Materials may, however, be subjected to cyclic stresses in service, which are superimposed over a steady-state focus. This is depicted in Figure 1.9 and the numerous terminologies used to define the pressures. The algebraic mean of max and min in the cycle is defined as the mean stress [39]:

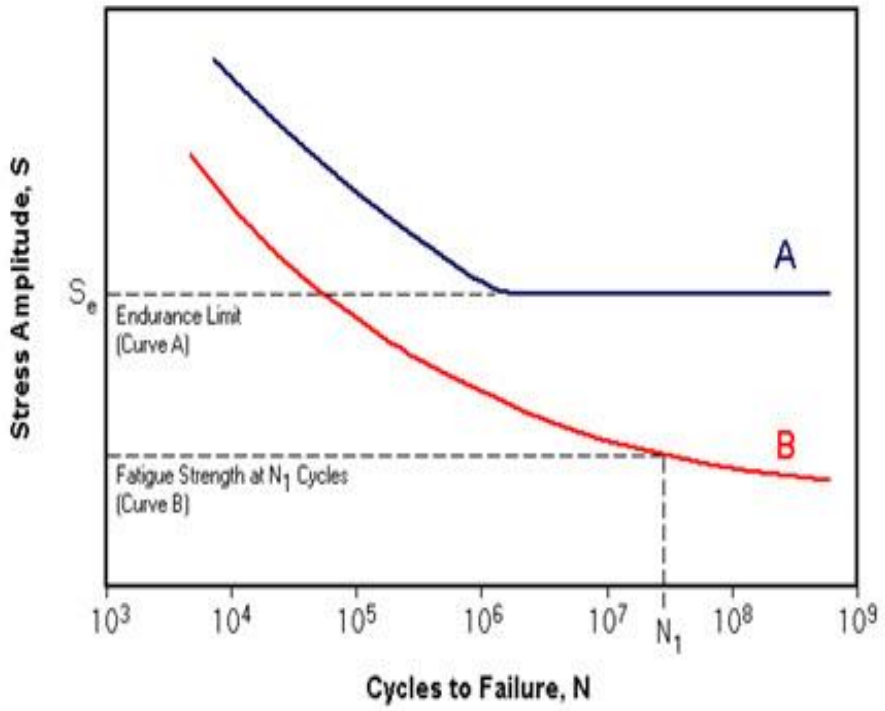

Figure 1.8: S-N curves with and without fatigue limits [39].

$$\sigma_m = \left(\frac{\sigma_{max} + \sigma_{min}}{2}\right) \ldots\ldots\ldots\ldots\ldots (1.2)$$

where σ_m is the mean stress (MPa), σ_{max} is the maximum stress (MPa) and σ_{min} is the minimum stress (MPa).

The alternate amplitude, a, is half the cycle's stress range:

$$\sigma_a = (\sigma_{max} - \sigma_{min}) \ldots\ldots\ldots\ldots\ldots (1.3)$$

The stress range (Δσ) is the algebraic difference between the maximum and minimum stress levels :

$$\Delta\sigma = 2\sigma a \ldots\ldots\ldots\ldots\ldots (1.4)$$

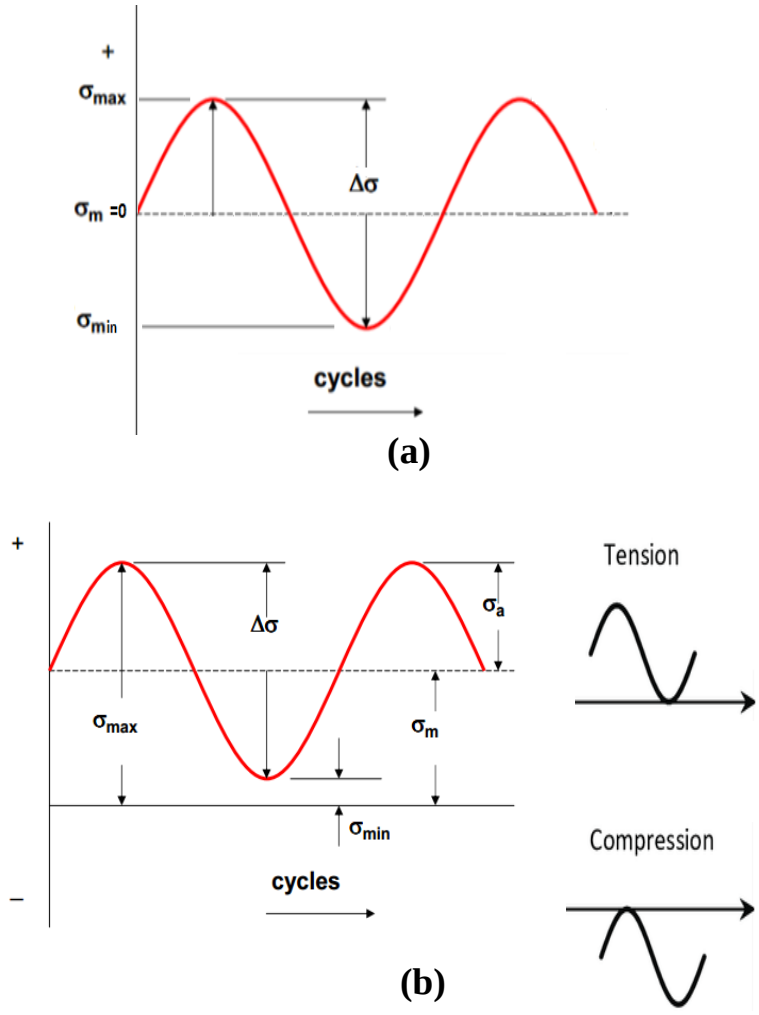

Figure 1.9: Graphic of stress cycles: (a) reverse stress cycle (R=-1), and b) repeated stress cycle (R=0 or R=1) [44, 39].

The important stress ratio (R) which is the maximum to the minimum stresses of a fatigue cycle important in determining the kind of loading as below [42, 44]:

$$R = \frac{\sigma min}{\sigma max} \dots\dots\dots\dots\dots (1.5)$$

R = 1 means the loading is static tensile,

R= 0 is for tension release.

R = -1 is corresponds to completely reverse loading.

1.5.5 Residual Stresses

Residual stresses are those stresses that remain in the material after removing the loads beyond the elastic limit resulting in plastic deformation, thermal gradients or other causes [45]. They result in significant plastic deformation, leading to undesirable effects such as warping and distortion or increased susceptibility to fracture and fatigue of components. Residual stresses caused due to many reasons some of they are as a results of manufacturing processes such as welding, brazing or heat treatments [46]. Mechanical loading and processes also contribute in initiation of residual stresses. Many procedures are utilized to reduce the side effect of residual stresses contained within a component such as heat treatments or mechanical processing. For example, heat treatments after welding of components are important to relieve or redistribute the residual stresses. On the other hand, residual stresses are sometimes desirable in some applications [47]. LSP process introduces beneficial compressive residual stresses on the surface and to a certain depth of the body of components. For example, introducing residual stresses to fan blades for turbine engines contributes to increasing scratch resistance and enhancing the fatigue life through obstructing cracks initiation and halting propagation [48].

In LSP a pressure pulse is generated by the formation and expansion of plasma plume over the surface resulting in extremely high-pressure shock. The impact of the shock waves on the target surface causes pure uniaxial compression stresses in the impacted volume. A compressive stress field is formed in the impacted volume as a result of the response in the zones around the shock peening impact, while the underlying layers are in a smaller magnitude tensile condition [49]. Figure 1.10 is a graph for experimental results demonstrates the effect of LSP on Al 2024-T351 test specimens where residual stresses introduced into treated components [50]. Plastic deformation happens

as the shock wave travels through the material to the point where the peak stress no longer exceeds the material's Hugoniot elastic limit. [87] Hugoniot elastic limit is related to dynamic yield strength as follows [51]:

$$HEL = \frac{(1-\nu)\sigma_y}{(1-2\nu)} \dots\dots\dots\dots\dots (1.6)$$

where *HEL* is Hugoniot Elastic Limit (MPa), ν is the Poisson's Ratio, and σ_y is the dynamic yield strength at high strain rates (MPa).

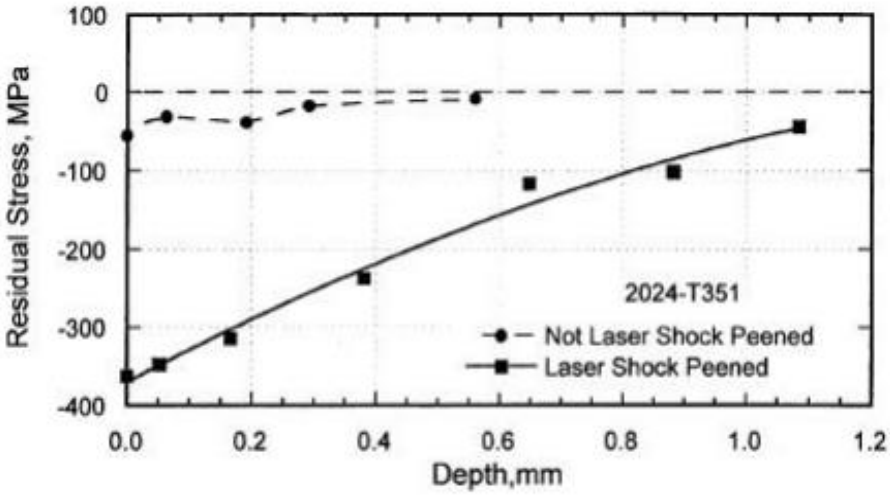

Figure 1.10 Residual Stress Profiles before and after LSP [50].

As previously stated, residual stress distributions are highly influenced by laser intensity and pulse repetition. With repeated laser shocks, the amount of surface and subsurface residual stresses inside a component grows until a saturation threshold is achieved [52].

1.6 Surface Treatment Techniques

Surface treatments are broad range of different processes applied to the surface of materials for the purpose of adding or enhancement of variety of functions such as mechanical properties, appearance, corrosion and wear resistance [53]. Surface treatment application can be classified into two types:

thermal or mechanical treatments applied in traditional and nontraditional techniques. Figure 1.11 presents a classification for surface treatments utilized by laser classified into two main subcategories thermal and mechanical. Laser thermal surface treatments involves metallurgical changes for a layer of the surface due to sufficient heating or melting by laser [54].

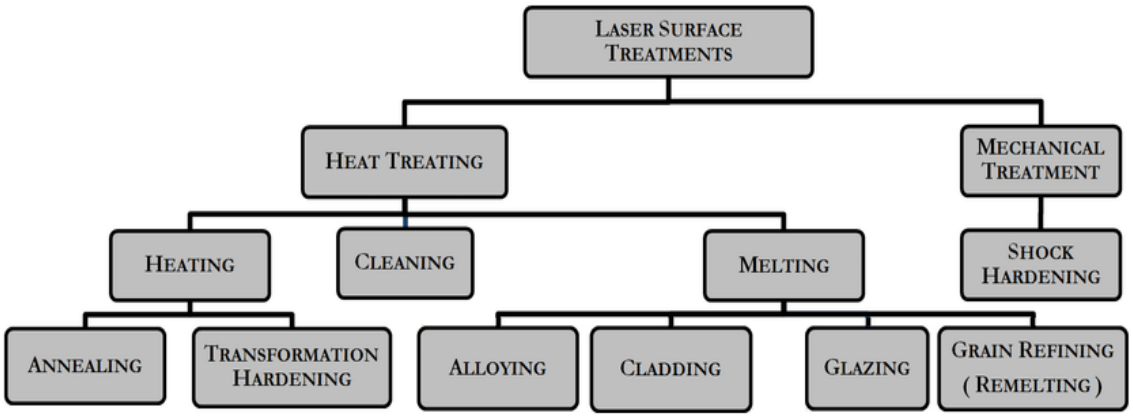

Figure 1.11: Classification of laser surface treatments [55].

Mechanical treatments used to reinforce a certain depth of a surface layer for the workpiece by achieving local plastic deformation which leads to compressive residual stresses. This class involves traditional and nontraditional techniques**.**

1.6.1 Traditional Mechanical Techniques

1. Shot Peening (SP): SP is a surface improvement process has been used for over six decades. Figure 1.12 illustrates a schematic diagram for SP technique which utilize small, spherical metal or ceramic balls blasted on a target to peen its surface. The plastic deformation causes a low depth of compressive stresses on the outside and tensile stress on the inside. Multiple spherical shots create overlapping dimples and residual stresses throughout the surface [56]. It is not controllable and hence cannot produce uniform residual stress distribution. The surface finish is compromised, and therefore it is not suitable for all

applications. The impact of blasting balls on the surface of a component yields a roughened surface. This effect is more pronounced in soft materials. Therefore, it may not be the best procedure if a product's surface polish is critical [57].

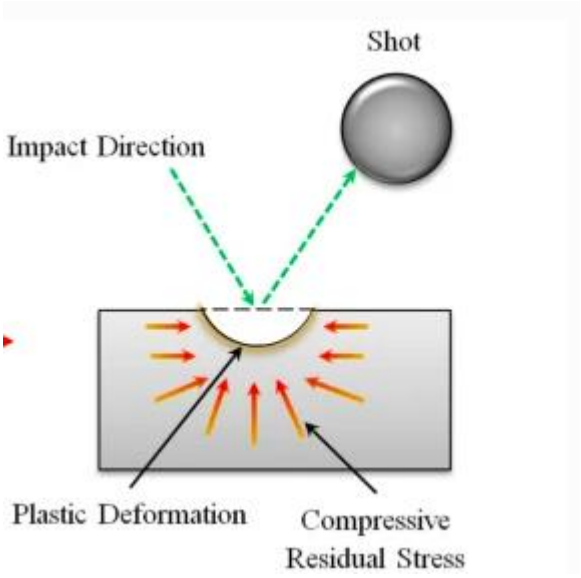

Figure 1.12: Illustration of shot peening and generation of residual stresses [58].

2. Low plasticity burnishing (LPB): LPB is a surface improvement process developed in 1998. LPB procedure entails rolling a high-modulus ball or roller across the component's desired surface as shown in Figure 1.13. This technique changes the mechanical properties depending on the governing parameters [59]. Low-cold working has the same effect on the material as SP; this is a low-cost option. LPB technique has a simple setup and produces a higher surface polish compared to SP [60]. This technique has the advantage of being carried out in any numerically controlled environment. The ball finish used in the LPB process determines the surface finish attained; the ball is a wear-prone component. Similar to SP, contact between the burnishing ball and the surface

causes elastic and plastic deformation. The LPB technique has the drawback of being difficult to apply to curved or complicated shapes [61].

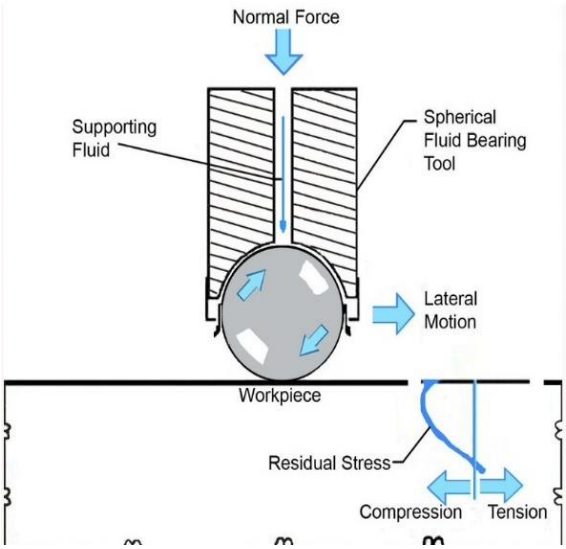

Figure 1.13: Low plasticity burnishing process representation [62]

1.6.2 Non-traditional Mechanical Techniques

1. Ultrasonic Impact Peening (UIP): UIP is a work hardening technique that uses a hard metal tip of high-frequency and high-velocity impact to plastically deform a material in order to produce advantageous compressive residual stresses (Figure 1.14). Work hardening creates residual compressive stresses in metal surfaces in order to replace remaining tensile stresses [63]. UIP device is small and lightweight. Although the residual pressures are greater than those caused by SP, the surface more roughened. Because of handheld instruments, consistency and flexibility are difficult to achieve [64].

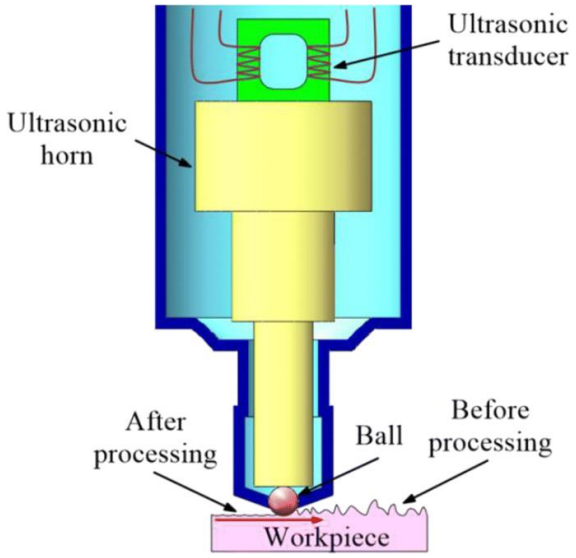

Figure 1.14: Schematic diagram of surface micro-structures process using UIP [65].

2. Water Jet Peening (WJP): WJP technique high pressure water is jetted into the water at high speed from a special cavitation-promoting (air bubble) nozzle to cause cavitation, and GPa class impact force when bubbles collapse near the workpiece produces a peening effect (Figure 1.15). This approach has many advantages over other current technologies, including low cost, lake of heat that can damage the area, and a spotless surface. WJP process is a physically complex procedure that requires additional investigation [66].

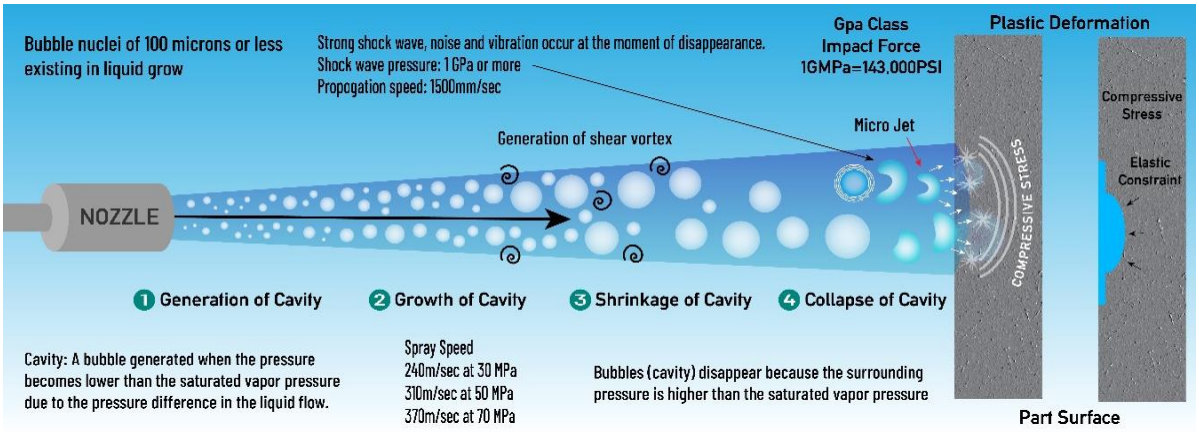

Figure 1.15: The schematic diagram of WJP process [67].

3. Laser shock peening (LSP): LSP is a novel non-traditional mechanical technique for surface treatment used to improve the fatigue life of components under cyclic loading [68]. The process imparts compressive residual stresses on and beneath the treated surface of materials that are mechanically caused due to a high magnitude of shock waves induced inside in the processed material [69]. LSP employs an energetic short pulse laser beam to produce high level compressive residual stresses of more than 1 mm in depth which four times deeper than standard SP [70-72]. Where the latter has used industry used for over a century to improve the surface and fatigue resistance of metallic components [73].

LSP has been widely discussed in researches that show increase the resistance to fatigue failures, stress corrosion cracking and wear resistance of metals [74]. As shown in Figure 1.16, LSP process can be accomplished by ablation of a sacrificing layer overlaid on the treated metal by Q-switched short pulses of laser radiation of peak intensity greater than 1-10 GW/cm^2 [75-77]. Due to ablation, the expanded high-pressure plume exerts stresses on the metal surface. When the induced stresses exceed the yield stress of the metal, plastic deformation occurs and a hard surface layer is formed that can effectively resist crack initiation, spreading and propagation [78]. The improvement in the performance of the treated metal is related to the formation of residual stresses created by plastic deformations [79]. The optimal LSP process is characterized by plastic deformation which mitigates surface tensile stresses and introduces preferable beneficial compressive residual stresses [80].

When the peak stress of the shock wave is greater than the material's yield strength, plastic deformation occurs [81]. As the shock wave penetrates further into the fabric, deformation occurs until the peak stress value of the shock wave diminish below the material's yield strength [82].

Localized plastic deformation induces strain hardening and residual compressive stress at and below the surface of the laser peened component. [83]. It may be necessary to repeat the number passes with laser from 2 to 4 over the same region in order to replace the opaque layer in that area [84]. However, this repetition may have no effect on the component's residual stress levels [85]. However, this repetition has little effect on the component's residual stress levels [86]. LSP intensity can be regulated and monitored, allowing the process to be adapted to specific service, manufacturing, and geometrical needs [87]. Several materials have been successfully peened, demonstrating the efficiency of LSP and the resulting residual stresses. Materials laser peened include various steel grades, titanium alloys, copper alloys, aluminum alloys, zinc alloys, brass, magnesium alloys, nickel-based alloys, super alloys, bulk metallic glass, and other materials. [88].

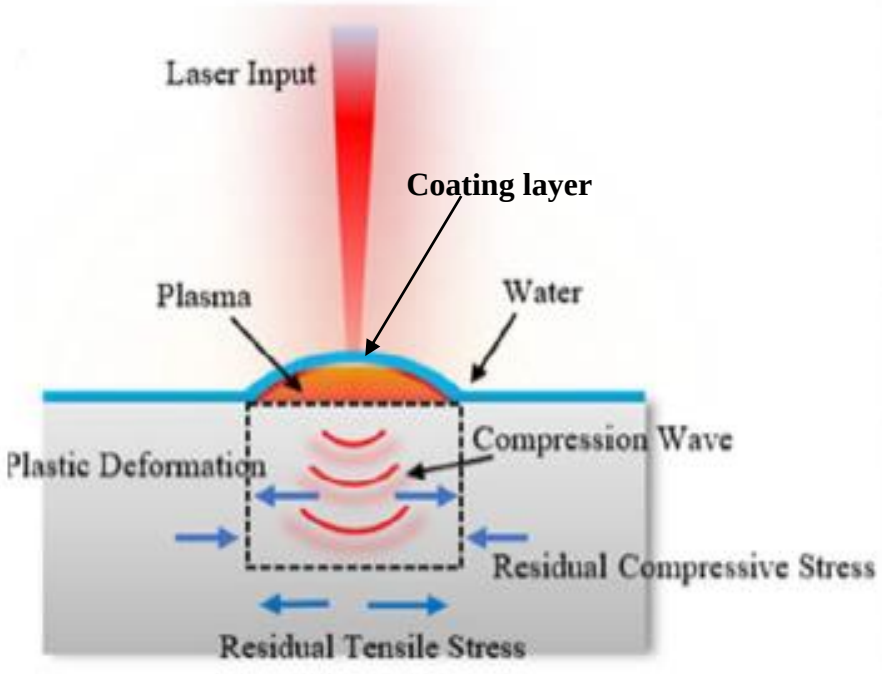

Figure 1.16: A Schematic diagram of laser peening process setup [85].

1.7 LSP versus Conventional SP

LSP consistently outperforms SP when it is associated with introducing beneficial compressive residual stresses comes in order to enhance the material properties. Table 1.3 lists a comparison between the nontraditional LSP versus the traditional technique SP.

Table 1.3: A comparison between LSP and SP processes [41,89]

LSP	SP
LSP is said to be preferable for thin parts.	Because of the risk of damage from SP, it is not viable to utilize it on thin parts.
In general, LSP produces fewer rough surfaces compared with Sp.	SP, in particular, creates a rough surface with significant increases in mean and peak roughness. This is good for paint adhesion, but it hurts the wear and fatigue resistance.
LSP induced stresses can range in depth from 0.5mm to over 1mm.	In mild metals such as aluminum alloys, the SP depth is usually less than 0.25 mm, and in tougher metals, it is less than 0.25 mm.
In LSP there are minor surface stress gradients, which considered an advantage because it is essential in minimizing or eliminating cyclic stress relaxation.	Since the relaxation is associated with dislocation movement, it is then correlated to the plastic strain. Example plastic strain in LSP is 10^6 and SP is 10^4 (s^{-1}).
The magnitude of compressive stress at the surface (or just below the surface): nearly the same in LP or SP, about 60% of the elastic limit.	
In some grades of Al alloys, LSP provides about 22% increase in fatigue strength compared with untreated metals.	In some grades of Al alloys, SP provides about 11% increase in fatigue strength compared with untreated metals.
The duration for inducing peak pressure in is 10 - 20 times longer than in the case of SP.	
The LSP treatment, residual stresses tend to relax more slowly than SP.	The significant disadvantage is the contact between the blasting ball and the surface causes residual stresses, which tend to release fast after repeated loading.

Figure 1.17 illustrates the most significant characteristics that make LSP more preferable in applications than traditional SP. LSP are characterized by more treatment depth where the residual stresses induced, significant better enhancement of fatigue life, precision when processing local areas and stability of peened areas at high temperatures.

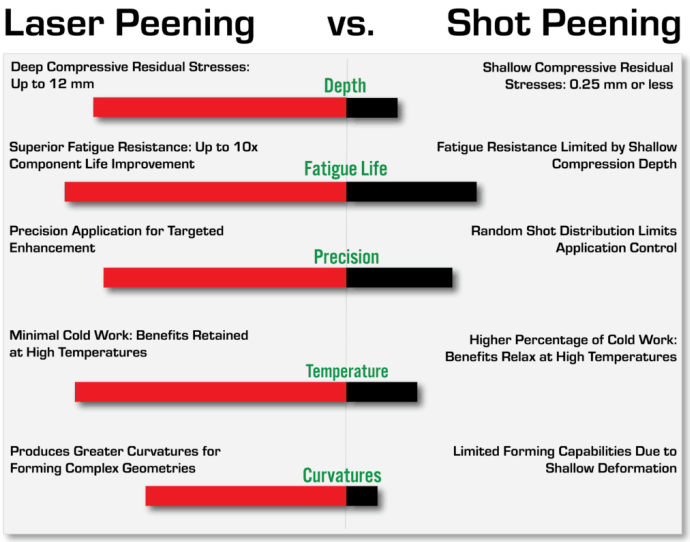

Figure 1.17: Why LSP is more preferable than SP [6].

Figure 1.18 shows an experimental comparison for the induced residual stresses caused by LSP in Inconel 718 alloy processed with SP and LSP processes. It is clear the residual stresses are much higher in LSP than in ordinary SP. Table 1.4 shows a comparison between the loading conditions of both processes [90].

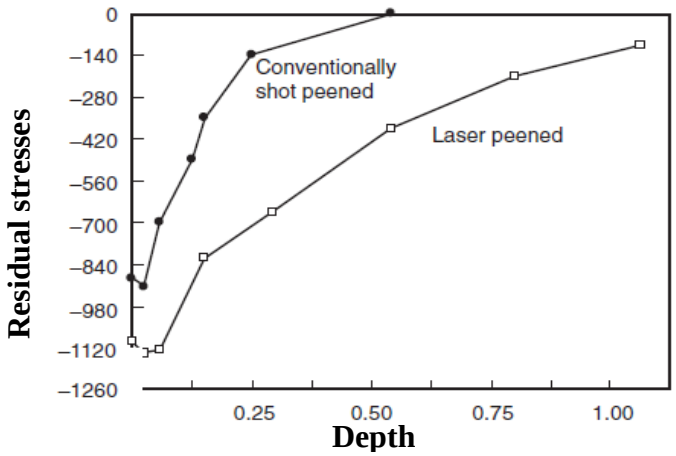

Figure 1.18: Residual stresses in the surface of Inconel 718 induced by laser peening and conventional shot peening [41].

Table 1.4: Comparative loading conditions induced by LSP and SP [41].

Process	Peak pressure (GPa)	Diameter of impacts (mm)	Pressure duration (μs)	Mechanical impulse (GPa μs)	Strain rate (s^{-1})
LSP	0–6	1–15	0.05	0–0.3	10^6
SP	3–10	0.2–1	0.5–1	1–10	10^4

1.8 Advantages and Disadvantages of LSP

LSP offers a reliable solution that is unrivaled by current technology. In a wide range of ferrous and non-ferrous metals such as steel and stainless-steel alloys, aluminum alloys, titanium alloys and soft alloys LSP has enhanced fatigue strength. The brief laser pulse offers accuracy, depth, and power to high-fatigue regions of components. The following are the benefits and drawbacks of the LP method:

1. Advantages of LSP

- When residual stresses are treated with LSP, they tend to release more slowly, which improves fatigue characteristics [41].

- There is no physical instrument used in the LSP procedure to produce residual stress.

- Because a laser is a light beam that may reach any complex position within a complicated designed equipment, LSP's adaptability to difficult geometries is a unique benefit.

- LSP is a unique repeatable and controllable procedure.

2- Disadvantages of LSP

- LSP produces non-uniform residual stress across the laser point, despite being a controlled process. The metallurgical qualities of the peened component determine this non-uniformity.

- The cost of LSP is rather costly; but, as laser technology progresses, the cost should reduce.

1.9 Process Parameters and Quality

The purpose of LSP is to create compressive residual stresses in components. The quality of the process is highly correlated with the control of the process parameters and the amount and condition of released energy by the laser. In addition, the nature of the interaction between the energetic pulse laser beam and the treated surface are the two critical criteria that affect the process [85].

1.9.1 Transparent and Absorbent Coating Layers

The transparent overlay layer is utilized as a pressure confining barrier benefit in keeping the built pressure at its generated value. Many types of substances, that considered transparent to the applied laser beam, are utilized for the process like water, glass, fused quartz, and acrylic [91]. This restricting overlay captures the quick increase of plasma on the metal surface, causing plasma pressure to climb significantly higher than in the absence of the layer. A term called the impedance effect can be defined as the resistance of a material against ultra-acoustic waves passing through it. The impedance effect depends the confining medium type, density and acoustic velocity [92]. Higher impedance effect of a matter, which measured in kg/m^2s, requires more laser intensity to produce higher shockwave transmitted through fabric. Water is more in use since it is relatively inexpensive and eliminates any heat generated

by the laser peening process [93]. The absence of a transparent overlay layer, cause the induced plasma formed by vaporizing of the opaque coating extends freely from the component's solid surface. As a result, the generated pressure shockwave will be insufficient to produce compressive residual stresses in part being treated [74]. For example, a Hadfield steel specimen showed weak results when peened without a transparent overlay [94].

The absorbent sacrificial layer employed on the component being treated affects the mechanical consequences of the laser-caused shock waves in a metallic element [95]. When a sufficiently intense laser pulse irradiates a metallic target coated with an absorptive layer, vaporization takes place and a plasma created [96]. The hydrodynamic expansion of heated plasma in the confined zone between the metal target and the transparent overlay produces a high-amplitude, short-duration pressure pulse [97]. The treated metal absorbs a portion of this energy as a shock wave. When the shock wave's pressure exceeds the metal's dynamic yield strength, plastic deformation occurs, altering the treated metal's near-surface microstructure and characteristics [98]. The thermal effect occurs only in the coating layer if the metal surface is coated with an absorbent protective layer such as organic paints (black paint), black tape, adhesives, metallic foils (aluminum foil). In addition to increase the intensity of the generated shockwave the important function of absorbent sacrificial layer is to protect the treated surface from laser ablation or melting [99].

When LSP applied without a sacrificial layer, the surrounding material compressively plasticizes the heated zone created by the laser's thermal effect during dilatation [100]. After cooling, tensile stresses and strain may arise. Excessive surface roughening is also induced [101]. Tensile residual stresses imposed into the treated component without an absorptive layer is comparable to that caused with an absorptive coating at very depths [102]. This does not

utilize a porous layer, while the laser energy intensity regulates LSP and thermal side effects such as ablation or local melting. This can be observed in Figure 1.19 based on tests conducted by Peyre et al. [103] on 55Cl steel test samples with various coatings. The coated specimens showed highest compressive stresses, whereas those without absorbent layer recorded the highest tensile stresses. The latter could be attributable to the LSP process's laser ablation effect [104].

1.9.2 The Process Parameters of LSP

The most important parameter in LSP is the power density (intensity) which related with the laser spot size and accessible power [105]:

$$I = \frac{P}{\pi\omega^2} \dots\dots\dots\dots (1.7)$$

where I is the power density (GW/cm^2), P is the peak power (GW) and ω is the spot size (cm).

The most common laser spot shape is round, some studies demonstrated that a square-shaped laser beam with enhanced characteristics can be used [106]. The residual stresses at the spot's center can be unstable when using circular spot shapes. The spot size of the laser in practice ranges from 6 to 10 mm, but it can be adjusted because it is only limited by the selected intensity. Residual stresses are produced significantly deeper beneath the surface of a treated material with larger spot sizes than with smaller ones [41].

In addition to the laser intensity Figure 1.20 illustrates a number of process parameters that are considered in any application of laser material processing. The parameter pulse duration (τ) which is the time measured across one pulse life at full width half maximum (FWHM) is considered an important factor in determining the regime of interaction between laser and the material. The pulse repetition rate is the reciprocal of the time between two identical points for two sequential pulses called pulse repetition time :

$$\tau = \frac{1}{PRR} \dots\dots\dots\dots (1.8)$$

where *PRR* pulse repetition rate (Hz), and *PRT* is the pulse repetition time (s).

The pulse energy is the optical energy content in one pulse. The pulse energy equals the shaded area, which is equivalent to the area covered by diagonal hash marks in the figure [105].

$$E = P_p . \tau = \frac{P_{av}}{PRR} \dots\dots\dots\dots (1.9)$$

where E is the pulse energy (J), P_p is the peak power (W) of the pulse and P_{av} is the average power (W).

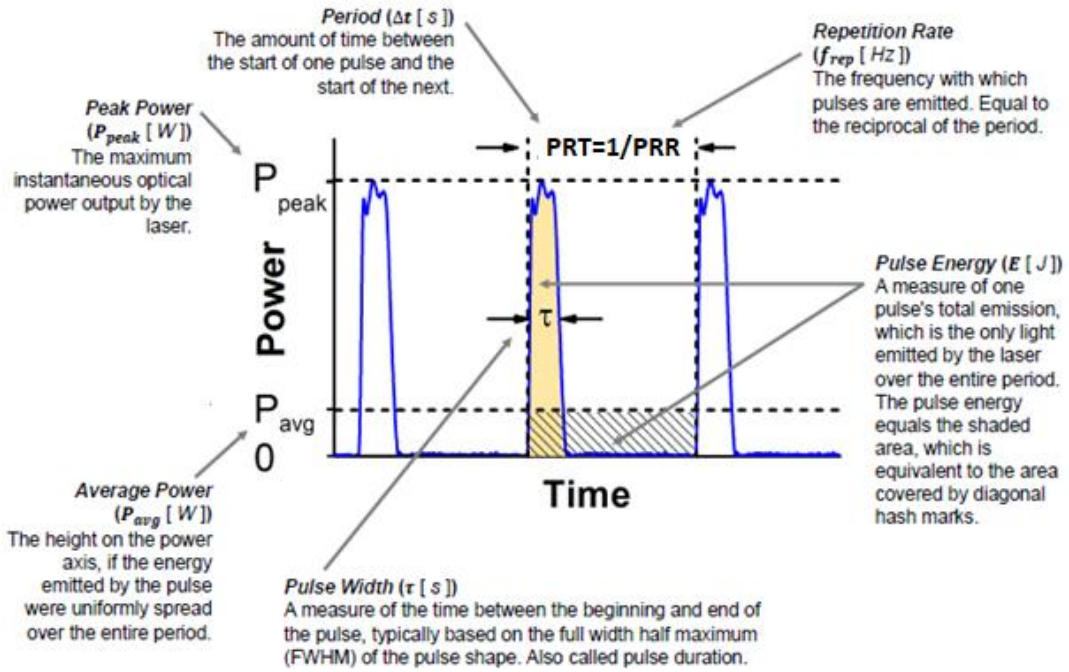

Figure 1.19: Laser Pulse Parameters [105].

1.9.3 LSP Calculations

LSP process parameters must be adjusted to yield laser intensity sufficient to produce the required induced pressure to cause plastic deformation[107]:

$$I = \frac{P_{av}}{\pi\ \omega^2 \tau\ PRR} \qquad (1.10)$$

where I is the laser intensity (W/cm^2), P_{av} is the average laser power (W) and τ is the pulse duration (ns).

Introducing compressive residual stresses on the metal to a certain depth imposes the achievment of sufficient induced pressure capable to deform the metal beyond the doubled value of elastic limit stress. The induced pressure can be estimated according to the hypothesized empirical equation by Fabro et al.:

$$p = 0.25\sqrt{I\ \mathrm{M}\ \mathrm{A}\ \mathrm{Z}} \qquad (1.11)$$

where P is the induced pressure (Mpa), A is the absorption coifficent for the black pain, M is the transmission coefficent of water layer and Z is the reduced shock impedance between the metal and the transmission overlay (kg/m^2.s).

The laser intensity value should range between two lower and upper limits. According to the above condition and Equation 1, the minimum required laser intensity (I_{min}) to result in effective plastic deformation is expressed as below:

$$I_{min} = \frac{64\ \sigma_{Dy}^2}{MAZ} \qquad (1.12)$$

where σ_{Dy} is the elastic limit stress (N/m^2).

In LSP many things should be avoided such as excessive deformation, surface ablation and plasma shielding which inhibits laser pulses from the surface of the specimen. This requires the induced pressure should be less than the double of the dynamic ultimate tensile strength (UTS) value of the metal (σ_{DU}) and, accordingly, the maximum value of laser intensity (I_{max}) is as follows [17]:

$$I_{max} = \frac{64\ \sigma_{DU}^2}{MAZ} \qquad (1.13)$$

According to the above considerations, the calculated useable laser intensity to apply LSP for Al 6061-T6 was deduced to be within the range as below:

$$I_{max} = 1.8\ GW/cm^2 > I > I_{min} = 3.8\ GW/cm^2$$

The percentage of overlap between sequential pulses and the number of accumulated pulses per spot of the laser beam are the most operating parameters that are related to the *v* has effect in LSP [108]:

$$OV\ (\%) = 1 - \frac{v}{2\omega\ PRR} \times 100 \ldots\ldots\ldots\ldots\ldots (1.14)$$

$$N\left(\frac{pulse}{spot}\right) = \frac{1}{(1 - OV)} \ldots\ldots\ldots\ldots\ldots\ldots (1.15)$$

where v scanning speed (mm/s).

1.10 Applications of LSP

In aviation and power generation industries, among other parts LSP is used to treat the roots of turbine blades, fans, compressors, engine parts, fastener holes and fasteners, brakes, welded aircraft parts, and wheels. Also, it is utilized to increase orthopedic implants' fatigue performance in the medical field. It is benefit in the treatment engine parts, gears, transmission axles, and other components in automotive industry. It is used to treat drill bits and other machine tool components in the tooling business.

Beyond improved wear resistance and fatigue life, LSP has shown to be an adequate procedure in a variety of performance-related applications:

1- At higher temperature ranges, compressive residual stresses are retained.

2- Crack growth rates (da/dN) are being reduced.

3- Increasing the longevity of welded components.

4- Damage resistance to fretting has been improved.

5- Increased resistance to galling.

6- Increased resistance to spallation.

7- Increased resistance to stress corrosion [109-111].

1.11 Experimentation Techniques

1.11.1 One Factor at A Time Technique

One factor at a time (OFAT) method is the oldest experimentation technique that still frequently in use [112]. It could be inefficient and unreliable resulting in false ideal circumstances. Furthermore, it may involve a great deal of trial and error, relying on luck, intuition, judgment, and experience to succeed [113]. On the other hand, this technique does not necessitate advanced statistical understanding, data analysis and processing [114]. When it comes to conducting experiments, many organizations still choose this method to identify the significant factor of a process. . In a sequential procedure, in OFAT method the impact of each factor on the response is discovered by altering it while keeping the other factors constant. In such method, the number of experiments to be conducted can be decided without an idea about the nature of interactions among the factors. OFAT is a low precision process accompanied with chances of false and misleading. Like the Domino effect, if one experiment goes wrong resulting in Inconclusiveness results. In such technique is that if the factors interact, that is, if the influence of one element is dependent on the setting of another, the ideal locations will be missed (s) [5]. This implies that there is a connection. It denotes the existence of a link between the independent variables. For example: assuming Z is the event of stirring a cup of coffee and Y is adding sugar to a cup of coffee. The influence of these elements on the sweetness of the coffee is proportional to their levels. Neither piece affects its own, but they produce a sweet coffee when combined factors Z and Y interact with one another. This interaction is calculable. When fertilizer

and water are mixed, another form of interaction occurs. The combined effects are more significant than the sum of the individual products. Because there is no information, the interaction between components cannot be predicted using the OFAT approach, which might lead to the process's optimal conditions being misled [113].

1.11.2 Design of Experiments (DOE)

Design of experiments (DOE) is a method for planning, carrying out, analyzing and interpreting experiments in a systematic way. DOE employs statistical tools to analysis the effect of input variables and their interactions on a response or group of responses. This approach decreases the number of experiments required to develop an experimental model that can be used to investigate the effect of process factors and their interactions on the response [115, 116]. Manipulating of input variables at the same time is possible with DOE to identify the important interactions that may be not observed when applying experiments with one factor at a time method [117].

Response Surface Methodology (RSM) is a collection of mathematical and statistical methodologies for modeling and evaluating problems in which a response of interest is influenced by a variety of variables, with the goal of improving and optimizing the response [118]. RSM technique strategy is to investigate the space of process or independent variables (x1, x2, x3, …etc.) and use empirical statistical modeling to establish an approximation relationship between response and process variables [119]. The objective is to search for the optimum set of process variables that produce the best response (y) values (Figure 1.22).

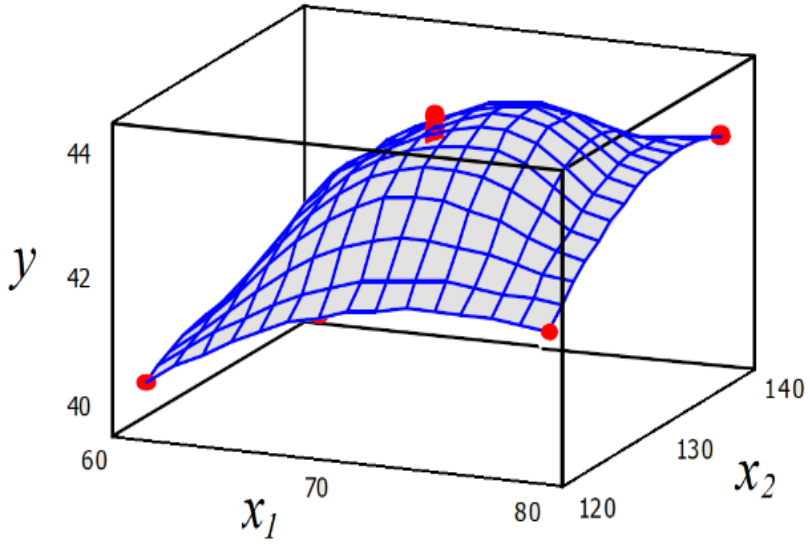

Figure 1.20: Response surface plot ($y = f(x_1, x_2) + e$) [119].

If the relationship between y and x's is not discovered, the response function's approximation $y = f(x1, x2,\ldots,xq) + e$ using RSM will be useful. Variables x1 and x2 are independent variables that influence the response y. The response y is a function of the process variables (x1, and x2) and the experimental error (e). Two important goals of RSM; the former is to find the optimum dependent variable (response) and the latter is to understand the direction of response changes by adjusting the design through manipulating one or more variables [120, 121].

1.11.3 Box-Behnken Design (BBD)

Box–Behnken design (BBD) is an experimental technique for RSM developed for modeling of the response surface through a smaller number of runs than the normal factorial design [122]. As shown in Figure 1.23, BBD utilizes twelve middle edge nodes and three center nodes to fit a 2nd order equation [123]. Conducting experiments requires placing each input factors (or independent variable) in three levels which means at three equally spaced values. In this way a quadratic model is well fitted including both the square effects and the effect of interaction between input factors [124].

Run	x_1	x_2	x_3
1	−1	−1	0
2	−1	1	0
3	1	−1	0
4	1	1	0
5	−1	0	−1
6	−1	0	1
7	1	0	−1
8	1	0	1
9	0	−1	−1
10	0	−1	1
11	0	1	−1
12	0	1	1
13	0	0	0
14	0	0	0
15	0	0	0

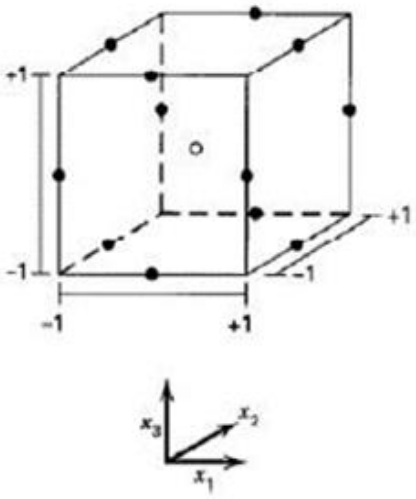

Figure 1.21: Box–Behnken design [122].

1.12 Literature Survey

A number of studies published recently revealed different researches concerned with LSP applied for different materials and conditions using an appropriate and intensive laser beam with a suitable setup. **Nie et al.** (2014) Investigated the influence of LSP on the high cycle fatigue parameters of the TC6 titanium alloy and connected discovered that the microstructure distribution to the LSP-induced fatigue improvement. Their findings showed that LSP-treated refined grains prevented fatigue crack initiation on the surface, while high-density dislocations prevented fracture propagation in the subsurface. May conclude that the LSP-induced CRS and microstructure are responsible for fatigue improvement [125].

Ren et al. (2015) examined the distribution of microstructure in an LSP-treated AZ91D magnesium alloy. The findings showed that nano-crystallines developed on the top surface. High-density dislocation structures such as tangles and cells formed on the subsurface, while high-density dislocation

tangles and partial twins formed adjacent to the matrix. Several earlier investigations have found that mechanical factors influence the gradient microstructure [126].

Lu et al. (2017) examined the microstructure response of titanium and aluminum treated with LSP .The LSP-induced twins and dislocations significantly reduced with increasing depth in pure titanium. The LSP-treated microstructure in the LY2 aluminum alloy was split into severe plastic deformation (SPD) areas, mild plastic deformation (MPD) sites, and substrates. There were a lot of dislocation walls and tangles in the SPD layer, but just dislocation lines in the MPD layer [127].

Marco Pavan (2017) applied LSP to middle crack tension specimens M(T), which are mostly typical of aircraft wing bottom coverings. Because these structural components are primarily intended to meet fatigue standards, increasing their fatigue and damage tolerance performance might result in lower maintenance or weight savings. LSP enhanced the fatigue life of unpeeled samples by up to fourfold, and a completely compressive residual stress profile was produced across the thickness along the crack opening direction [128].

J.T. Wang et al. (2017) investigated the effect of intense LSP on the microstructure and high-temperature fatigue characteristics of Al 7075 alloy at various elevated temperatures. Scanning electron microscopy (SEM) and transmission electron microscopy (TEM) were used to characterize the treated material's microstructure. At 150 °C, the sample showed a 110% increase in fatigue performance under high-temperature working circumstances. SEM imaging was used to detect grain refinement, work hardening, and precipitates. Significant changes in surface morphology were investigated after LSP in three phases of high-temperature fatigue. The findings indicated that a dense dislocation structure with large compressive residual stresses was formed, which improved fatigue performance at high temperatures [129].

Hao Wang et al. (2017) studied the effect of LSP on abrasion resistance in artificial seawater and corrosion resistance in a 3.5% NaCl solution for Al7075 alloy. The result shows when specimens were treated once and twice with an intensity of 7.17 GW/cm^2, the abrasion loss reduced by 43.75% and 46.09% compared to untreated. In addition, the corrosion rate is reduced by 50.32% [130].

Booba N. Aravamudhan (2018) This study is an investigation for LSP as a mitigation technique to improve corrosion and stress corrosion cracking resistance of Al 7075 - T6 alloy. LSP leads to a 14% increase in yield strength of the alloy, which contributes to the improvement in stress corrosion cracking resistance of the material in the sodium chloride environment. The increase in yield strength and corrosion resistance, along with microstructural changes induced by LSP, could have a combined effect in improving the SCC resistance. Thus, LSP is effective in improving the corrosion and stress corrosion cracking resistance of Al 7075 alloy [131].

Peng Liu et al. (2018) apply LSP to treat the weld surface of friction stir welded joints of Al 7050-T7451 alloys. The average hardness increased to 9 HV. The fatigue life after applying the process increased by 30%, 27%, and 5% when the loading stresses are 200MPa, 250MPa, and 300MPa respectively. The residual stresses in weld nugget zone, thermo mechanically affected zone (TMAZ) and heat affected zone (HAZ) shows significant value of 100 MPa after the process [132].

J.T. Wang et al. (2018) studies the impacts of LSP treatment on the creep characteristics and microstructural development of the Al7075 alloy's surface. The findings showed that LSP increased steady-stage creep life by 97% at 350 MPa/200°C, 307% at 350 MPa/200°C, and 120% at 300 MPa/200°C. TEM observation was used to investigate the mechanism for enhanced creep qualities of the alloy. The results show a significant improve the creep resistance of 7075 aluminum at high temperatures and operating stresses [133].

Chen et al.(2018) Examined LSP-induced grain refinement and the LSP-induced grain refinement was ascribed. Dislocation transitions or dynamic recrystallization are examples of grain refining. Their findings revealed a substantial number of dislocations. LSP generates dislocation cells, which are then converted. With increased deformation, dislocation of walls, and subgrains Because of dislocation-induced lattice flaws, large compressive residual The CRS is formed at and around the LSP-treated surface [134].

Gaurav Vilas Inamke (2019) This study is concerned with investigating the effects of warm laser shock peening (LSP) on the enhancement of mechanical performance of laser welded joints of AA6061-T6 and TZM alloy LSP demonstrated an enhancement in strength by about 30%. Lap welds showed an increase in joint force by 22% [135].

Junsu Park et al. (2019) experimentally studied the effect of LSP on the friction properties of JIS-AC8A aluminum-silicon alloy that used in pistons material for automobile engines. An Nd: YAG laser (wavelength=532 nm, pulse width=8 ns) was used to perform LSP with a laser intensity of 4 GW/cm^2, an overlapping ratio of 50%, and a spot diameter of 2.06 mm with no protective coating. Surface hardness rose by 22% after LSP, and compressive residual stress was significantly improved [136].

Binod Dhakal et al. (2020) used LSP to investigate the mechanical properties and microstructural development of Al 6061-T6 alloy utilizing a variety of characterization methods. Residual stress analysis, surface roughness, Vickers microhardness, tensile testing, X-ray diffraction (XRD), transmission electron microscopy (TEM), and electron back-scattered diffraction are some of the techniques used (EBSD). With a considerable increase in cross-sectional microhardness of up to 33.04 percent, a work hardened layer of ∼1500 μm depth is achieved. In laser peened specimens, a beneficial compressive residual stress of up to -273 MPa was created, with the total effect depth of around 100 μm along the effective depth zone [137].

Xian-kai Meng et al. (2020) utilized a nanosecond laser to enhance the strength Al 2024-T351 alloy. As a consequence, the treated alloy's microstructure, residual stress, nano hardness, and surface roughness data revealed refined grains in the peened surface. The residual pressure measured by LSP was 141 MPa, with a nano hardness of 3.1 GPa. They discovered that increasing grain boundaries resulted in a decreased rate of fracture start and a longer life. The crack growth rate was slowed and the crack growth life was extended due to the compressive residual stress. As a result, laser shock peening extends overall vibration fatigue life by 63.5 percent [138].

Ahmed R. Alhamaoy et al. (2020) experimentally investigate the effect of applying LSP on the fatigue performance for Al 6061-T6 alloy rotary shafts using Q-switched pulsed Nd:YAG laser. The effect of two pulse energies as operating parameters 500 mJ and 600 mJ were employed in this investigation. The other parameters are pulse duration of 12 nanoseconds, and the pulse repetition rate of 10 Hz. For the cyclic fatigue test, LSP is applied at the waist of prepared Al shafts. The results reveal that providing 500 mJ pulse energy has a considerable effect on increasing the needed number of cycles to fracture the shaft through fatigue failure, hence boosting fatigue strength. Furthermore, raising the pulse energy from 500 mJ to 600 mJ has a considerable influence on developing a semi-endurance limit for the samples [139].

1.13 The Aim of the Work

The objective of the current project is to investigate the effect of LSP at different levels of some working parameters on the fatigue life for the Al 6061-T6 thin plates. The investigation is carried out with two experimentation techniques the OFAT and DOE based on BBD. Unlike most previous works in that field, the process was applied with a small spot size ranging from 0.02-0.04 mm, high repetition rate and high scanning speed reaching to 500 mm/s.

Chapter Two

Materials and Methods

2.1 Introduction

This chapter addresses materials, their preparation, specimen's configuration, equipment and processing steps for achieving LSP process on thin sheets of Al 6061T6 in order to enhance their performance under cyclic loading. The procedures utilized throughout the experimentation are described in depth in the current chapter. The sequential processes for the experimental part is revealed in Section 2.2. The utilized metal and its chemical analysis are presented in section 2.3. Section 2.4 describes preparation of specimens for the mechanical tests. The characteristics of the laser system is defined in section 2.5. LSP process parameters and employed LSP process are identified in Section 2.6 and 2.7 respectively. The utilized experimentation techniques in the current study OFAT and BBD are illustrated in section 2.8. The experimental imaging techniques for specimens before after treatment with LSP are presented in Section 2.9. Finally, Section 2.10 and 2.11 demonstrate the X-Ray diffraction analysis and its related calculations which is the basis for the calculations of the induced residual stresses in the specimens after treatments with LSP.

2.2 The Experimental Part Steps

This section provides a summary of the steps that are attempted and used in pursuing scientific research. The experimental phase passes through the following procedures:

1. Selection and preparation of the metal.
2. Analysis of the chemical composition for the metal.
3. Preparation of the specimens for the tensile tests.
4. Extract the mechanical properties from the tensile test.
5. Preparation of the specimens for the fatigue tests.
6. Building LSP process setup and apply experiments.

7. Fatigue test for the untreated and treated specimens.
8. SEM and EDS for different specimens as well as untreated ones.
9. XRD test for the untreated and treated specimens.
10. Calculation of Induced residual stresses.

Many fundamental procedures are essential to realize LSP. Figure 2.1 represents a flowchart for the sequence of achieving the process starting from materials selection ending with specimens production and testing. Also, the flowchart presents the employed systems in this project.

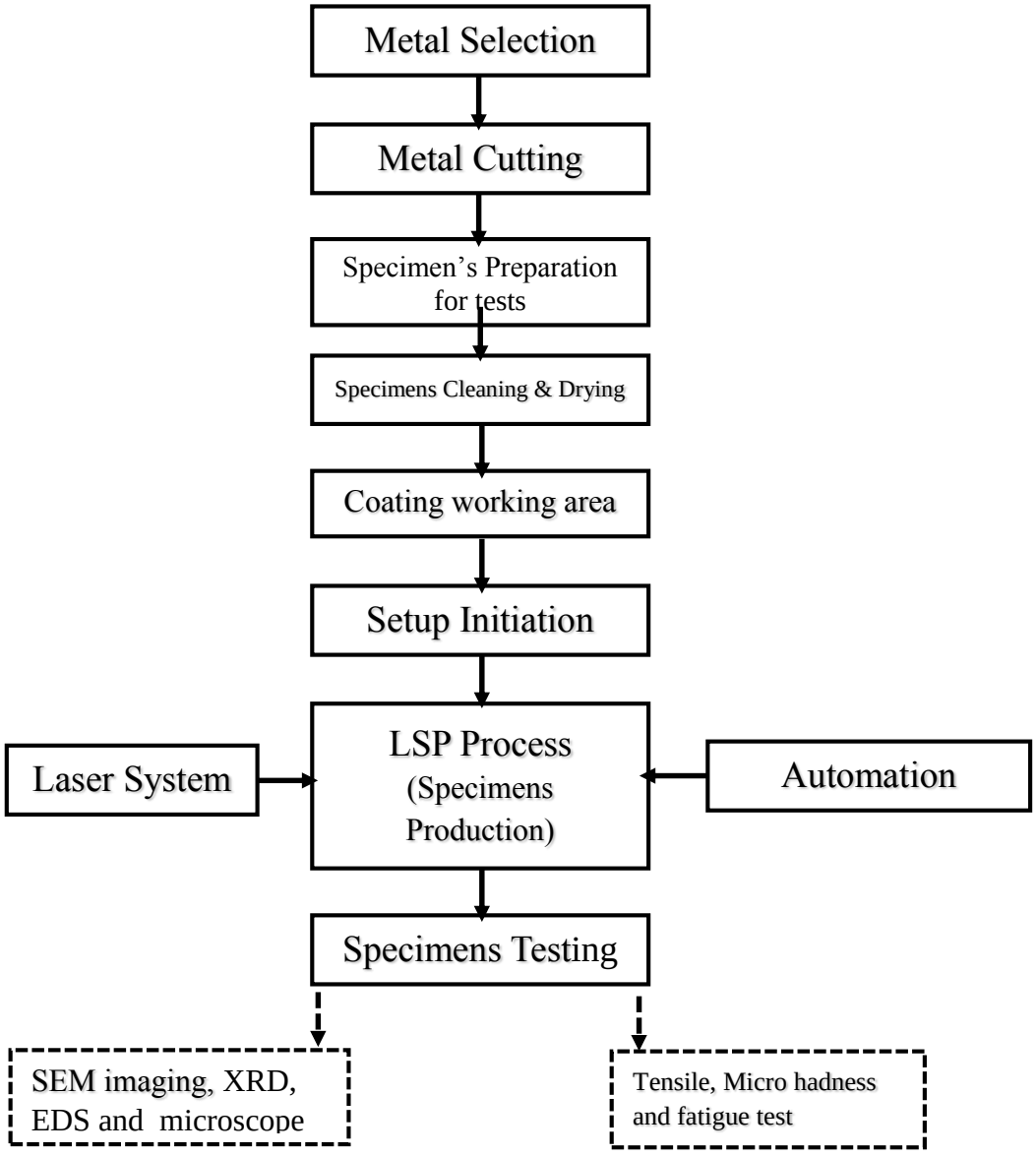

Figure 2.1: A flowchart for the experimental steps.

2.3 Metal Selection and Chemical Composition

Aluminum alloy 6061-T6 was selected in the current study due to their common use soft metal after steel in wire range of engineering and structural applications. In addition, one of their strengthen mechanism is the cold working and this can be accomplished through LSP. Table 2.1 shows the chemical composition for the employed alloy conducted in Baghdad laboratory of the General Company for Engineering Examination and Qualification (SIER).

Table 2.1: The Chemical Composition of Employed Aluminum 6061-T6 Alloy.

Si %	Fe %	Cu %	Mn %	Mg %	Cr %	Zn %	Ti %	P %	Pb %	Al %
0.677	0.548	0.236	0.131	0.844	0.179	0.0046	0.0787	0.0012	0.0094	97.2

Table 2.2: Chemical compositions of Aluminum 6061-T6 Alloy standards according to ASTM [140]

Si %	Fe %	Cu %	Mn %	Mg %	Cr %	Zn %	% Other	Al %
0.4-0.8	≤ 0.7	0.15-0.4	≤ 0.15	0.8-1.2	0.04-0.35	≤ 0.25	≤ 0.15	Reminder

2.4 Preparation of Specimens

Raw thin plates of Al6061-T6 were prepared in order to produce the required number of specimens for the mechanical tests of the current project.

2.4.1 Tensile Specimens, Production and Test

The tensile specimens were cut and prepared for the tensile test in order to extract the mechanical properties of the employed alloy. The specimen axis was chosen to be aligned with the material rolling direction, forging grain model. The profile and dimensions of specimens are according to the standard test methods for tension testing of metallic materials ASTM E8 as shown in Figure 2.2 [141]. The tensile test was performed under plane stress conditions at a speed of 2 mm/min using a 100 kN Universal Testing Machine type Tinius

Olsen-H100kU\USA (Figure 2.3). The water jet technique was used for specimens cutting the sheet metal into the determined shape to the required number of tensile specimens test. Table 2.3, tabulates the extracted mechanical properties from the performed tensile test.

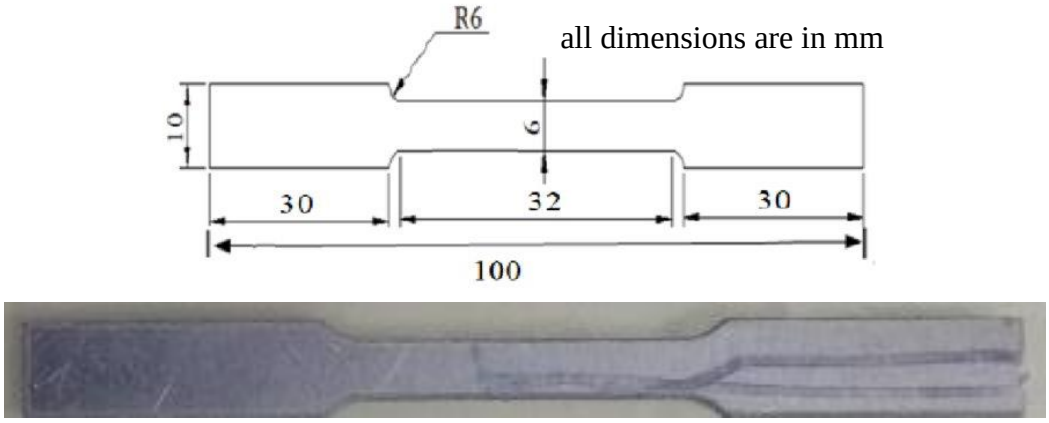

Figure 2.2: Geometry of a tensile specimen according to ASTM E8 [142].

Table 2.3: Tensile test results of Al 6061-T6 alloy.

Property	Yield Stress, (MPa)	Ultimate Stress, (MPa)	Elongation%	Modulus of elasticity, E (GPa)	Passion ratio
Experimental data	277.6	319.8	11%	69.8	0.3

(a)

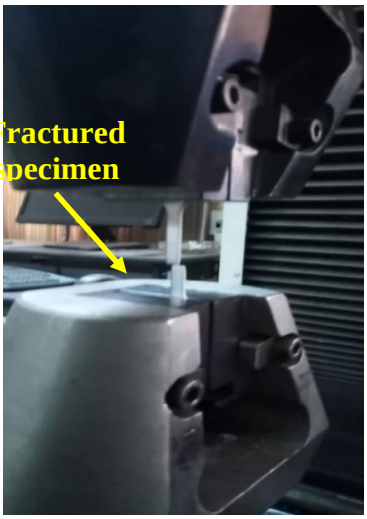

(b)

(c

Figure 2.3: a) Universal Testing Machine type Tinius Olsen-H100kU/USA, b) A fractured specimen at the end of tensile test.

2.4.2 Fatigue Specimens, Production and Test

The fatigue test specimens were cut and prepared to evaluate the fatigue life of specimens under cyclic loading. Like tensile test specimens, water jet technique was used to cut the fatigue specimens in a profile and dimensions according to the requirements of the manual of the fatigue test device shown in Figure 2.4 and Figure 2.5a. A number operations are considered essential for preparation of specimens. Grind the specimen's faces and sides with grinding papers (silicon carbide). Polishing faces and sides of specimens in order to remove any possible scratches and flaws by using a polishing alumina powder tool. Then, the specimens washed with water and soap before the step of cleaning with alcohol to prepare working areas for painting. Finally, cleaning the sample with a soft silky fabric until it has a high surface gloss (Figure 2.5b). The working area where the LSP applied at this part of specimen is coated with black paint to a thickness of 140 μm to work a sacrificing ablation layer during LSP process as seen in Figure 2.5c.

The Fatigue test was carried out at the Department of Materials Engineering/Al-Mustansiriyah University, Baghdad using the fatigue test machine type HI-TECH HSM20\ England illustrated in Figure 2.6a. The specimen is attached to the fatigue-controlled stress device as a cantilever which fixed in one end and free at the other. By applying a bending constant load at the free end of the specimen, the device impart a continuous stress and deflection to the end the specimen life Figure 2.6b. The deflection is measured by a dial gauge fixed on a stand as shown Figure 2.6c. Appendix A presents the procedures for determining the value of applied bending stress. The test was conducted at room temperature with zero mean tension (R=-1) and frequency is 25Hz. The produced groups of specimens are classified according the employed set of process parameters of LSP. Each set was subjected to six fatigue tests of different applied stresses 263, 235, 222, 217, 210 and 205 MPa.

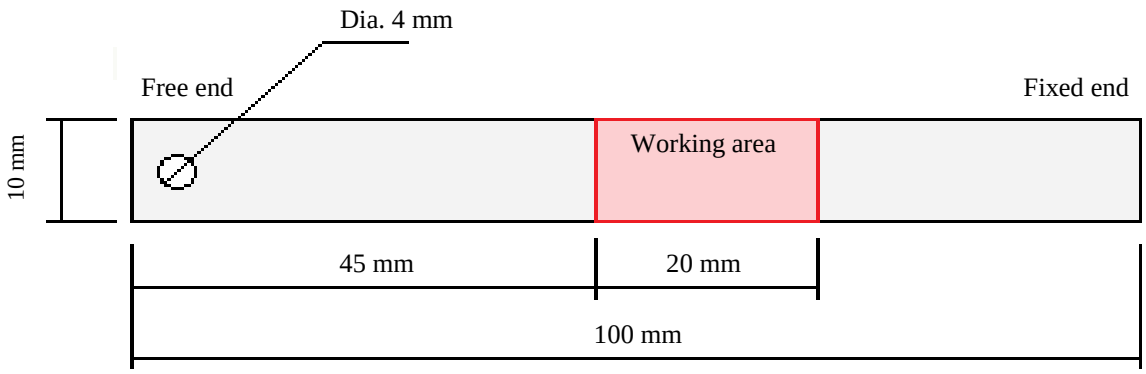

Figure 2.4: Fatigue test specimen final dimensions and state.

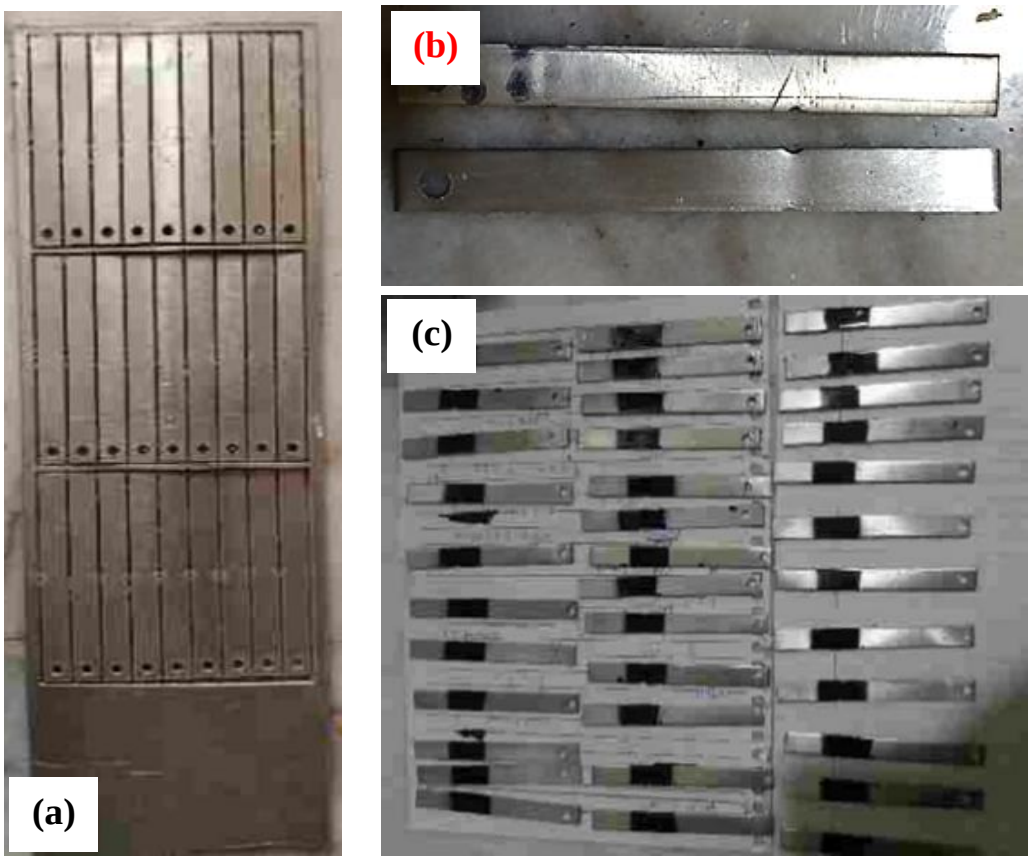

Figure 2.5: Steps of specimen's preparation for the fatigue test: a) after cutting with water, b) after polishing process and c) after coating the working area with black paint.

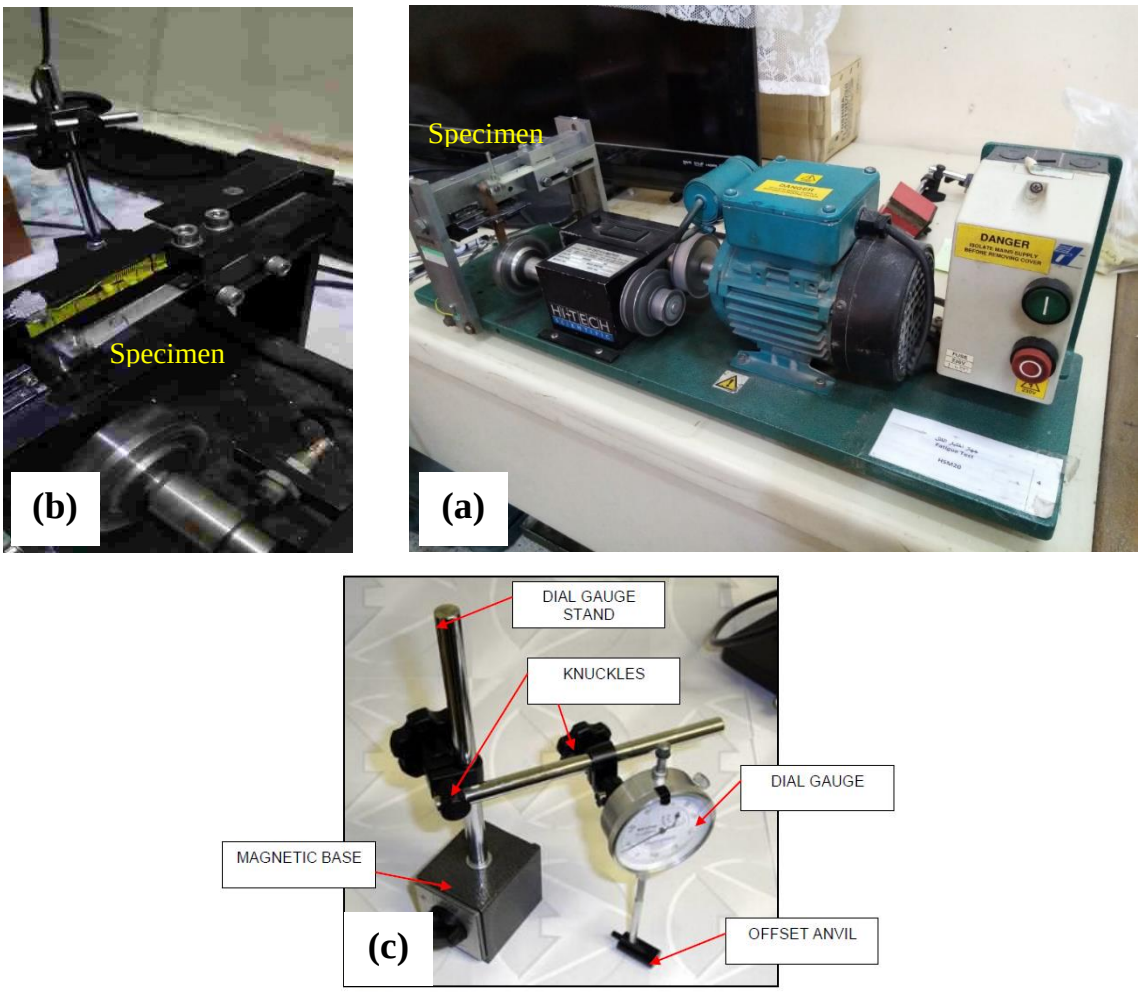

Figure 2.6: Bending- alternating fatigue device HSM20.

2.5 Fiber Laser System

A Q-Switched nanosecond pulse fiber laser type RFL-P (China) characterized by its high peak power, high pulse energy value and variable spot size was utilized in applying LSP process (Figure 2.7). It characterized by the stable performance and low-cost operation. The specification of this laser makes it suitable for some applications such as precise marking, engraving of graphics for different types of non-ferrous like aluminum, copper, silver and gold as well as stainless steel materials. Table 2.3 tabulates the important characteristics of the employed fiber laser. The laser beam is automated through

two Galvano mirrors facilities the laser spot to scan the x-y plane of the specimen's with a high speed reaches to 2000 mm/s.

Table 2.4: Employed fiber laser characteristics.

No.	Characteristics	Unit	Value
1	Average power (Pav)	W	100
2	Spot size (ω)	μm	10 - 3000
3	Pulse Width (τ)	ns	81
4	Operating Voltage (V)	V	24
5	Pulse repetition rate (PRR)	kHz	10 - 100
6	Wavelength (λ)	nm	1064± 4

Figure 2.7: Q-switched nanosecond fiber laser type RFL-P (China).

2.6 LSP Process Parameters

A number of employed parameters were employed in the process namely the pulse repetition rate (*PRR*), spot size (ω) and scanning speed (v). A number of pilot experiments were carried out before determination the requested

experiment range based on the criteria of avoiding specimens surface ablation. Table 2.4 presents the minimum and maximum range of each parameter.

The laser spot scans the working area (Figure 2.8a) on a 2D plane through Galvano mirrors with variable speeds ranging from 200 to 500 mm/s. To achieve a degree of homogeny in the applied induced pressure density on the metal surface, scanning the working area was conducted with an overlap ratio between sequential pulses. This overlap is of variable value along the scanning speed vector (*x*-axis) axis and constant equals 10% between two adjacent paths (*y*-axis) as seen in Figure 2.8b.

Table 2.5: Process Parameters ranges.

Parameter	Ranges	
PRR (kHz)	20.00	25.00
ω (mm)	0.02	0.04
v (mm/s)	200.00	500.00

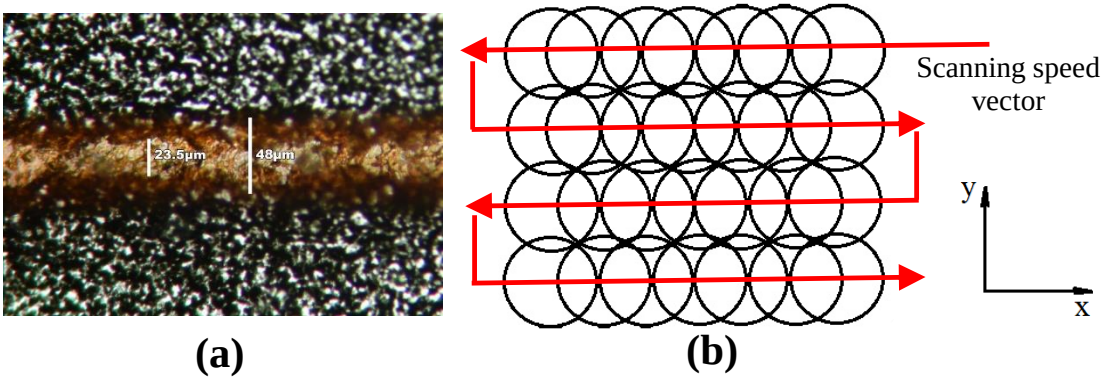

Figure 2.8: a) The fiber laser spot diameter, b) The scanning pattern and pulses overlap.

2.7 LSP Process

As mentioned before LSP process requires the presence of two layers, the ablative sacrificing layer which cover the treated area and the confining layer of water above the first layer to maintain the induced pressure in the interaction zone. The sacrificing layer was created on both sides of each specimen by

spraying the working area with a fixed thickness of 140 µm black paint. The water layer was established by immersing sample in water at a depth of around 2-3 mm beneath the liquid surface. The laser beam transmits through the water and focused on the ablative layer via a focusing lens of 100 mm focal length to produce a plasma plume and protect the metal surface from possible ablation thermal effects. By the water layer, the built plasma pressure intensifies and significantly reduces the increase in temperature that may occur. Figure 2.9a illustrates a schematic diagram for the built setup of the current study. All the describe components of the process were placed inside an aluminum pane fabricated for that purpose as shown in Figure 2.9b.

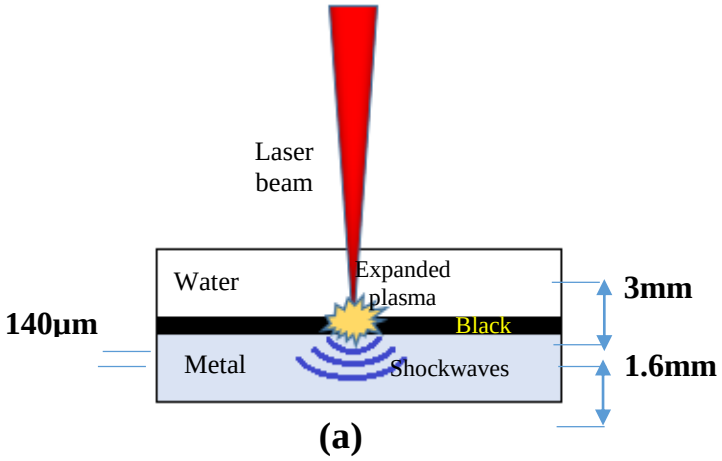

(a)

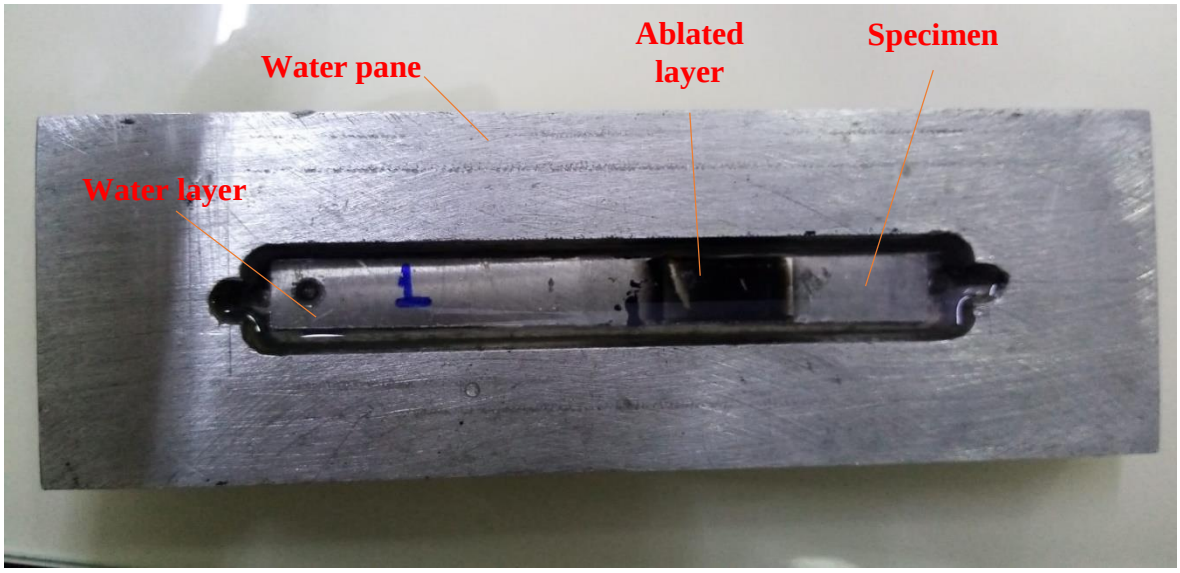

Figure 2.9: a) A schematic diagram of LSP process, b) The experimental setup.

2.8 Experimentation Techniques

2.8.1 One factor at a time (OFAT)

OFAT method is still in use and does not necessitate an advanced statistical understanding of data analysis and execution. LSP experiments were applied according to OFAT method to investigate the effect of process parameters on fatigue life until failure which expressed by the number of cycles (*noc*). The process parameters and their ranges are as follows: the pulse repetition rate (PRR) 20 kHz to 25 kHz, spot size (ω) 0.02 mm to 0.04 mm and scanning speed (v) 200 mm/s to 500 mm/s. With OFAT experiments the produced specimens were grouped to different sets of process parameters. Each set was applied to fatigue tests under five of different applied stresses: 263, 235, 222, 217, 210 and 205 MPa.

2.8.2 Design of Experiments (DOE)

DOE is a planning method, carrying out, analyzing and systematically interpreting experiments. DOE employs statistical tools to investigate the effect of input variables and their interactions on a response or group of reactions. This approach decreases the number of experiments required to develop an experimental model that can be used to investigate the effect of process factors and their interactions on the response [143, 144].

Design-expert v13 software package was used in the current study to perform DOE, analyze data, build the RSM model, and optimize the process through Box-Behnken design (BBD). Optimization was beneficial for predicting the optimum process variables that yield the best fatigue life. In RSM, the general second-order polynomial model was used as a functional link between the independent variables and the response surface [145]:

$$Y = b_o + \sum_{i=1} b_{ii}\, x_i^2 + \sum_{i=1}^{n}. \sum_{j=i+1}^{n} b_{ij}\, x_i x_j + e \text{.....(2.1)}$$

where Y is the response, the set b_o, b_{ii} and b_{ij} are linear, quadratic and interaction regression coefficients, x_i and x_j are the independent variables and e is the experimental/residual error.

BBD was utilized for three independent input variables, *PRR*, ω and v on the dependent response fatigue life. The range of input variables was designed and defined for the software to suggest the number and set of input variables for each experiment. Table 2.5 lists each input variable's range lower and higher range and corresponding coded levels. The experiments were carried out to obtain the response values, which were inserted into the software later. The experimental design considered three levels, three independent input parameters (*PRR*, ω, and v), and seventeen experiments. Table 2.5 presents the average fatigue life value of six specimens for each set of parameters group subjected to different loads and the raw metal *noc* values.

Table 2.6 Input parameters ranges and their coded levels.

Variable	**Actual values range at coded levels**		
	-1	**0**	**+1**
PRR (kHz)	20.00	22.5	25.00
ω (mm)	0.02	0.03	0.04
v (mm/s)	200.00	350	500.00

Figure 2.10 represents RSM modeling approach. According to this approach, RSM was applied for the DOE purpose and analyzed the response by developing the mathematical models that help predict the optimum mentioned responses as a function of selected input working parameters. The key to operating parameters selection and ranges values determination is the first step in Design Expert® software processing. The more realistic results eliminated extreme parameter values of no joining or high polymer degradation inferred from OFM tests.

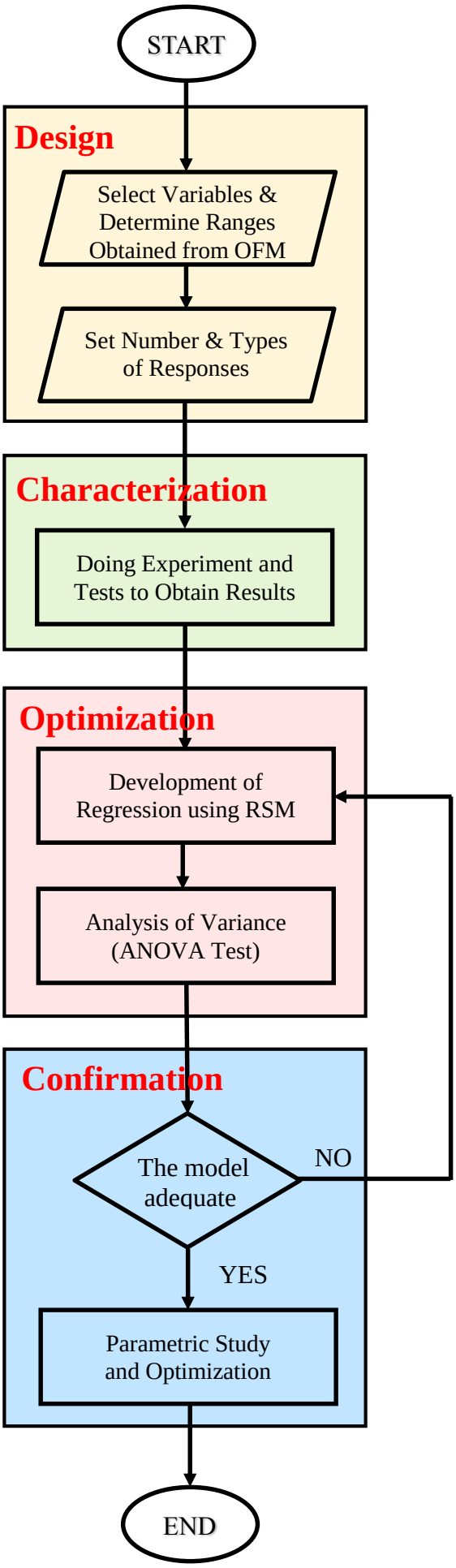

Figure 2.10: BBD based on DOE approach flowchart.

2.9 Specimens Surface Observations and Analysis

A number of tests was applied for the specimens surfaces in order to investigate the effect of LSP on the samples in term of chemical composition and structural changes. A modern optical microscope was used to magnify the cross section of some fractured specimens up to 1500 times with a spatial resolution of 0.2 μm. Figure 2.11a shows the microscope used for imaging type Lomo/Russia that supplied with a camera type Sony A7RII which employs the focus stacking optical technique through the Zerene Stacker software. Scanning electron microscope (SEM) imaging uses a focused beam of electrons to create images for a sample. When electrons interact with a material, they generate a variety of signals that can be detected by electron microscope detectors, providing information about the sample's surface topography and composition. The chemical analysis of surfaces was utilized through energy dispersive spectroscopy (EDS). SEM and EDS inspections were carried out by SEM-EDS device type Inspect™\ Netherland as shown in Figure 2.11b. INspectF50A device is a general-purpose field-emission for high-resolution SEM imaging employed for imaging as well as EDS analysis for the untreated and peened specimens.

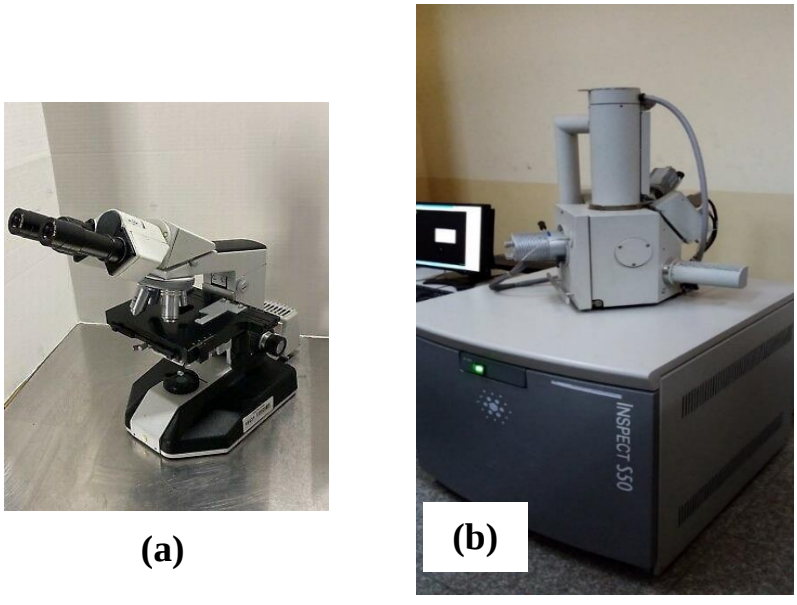

Figure 2.11: Specimens Surface Observations: a) Optical microscope type Lomo™, b) SEM-EDS device type Inspect™.

2.10 X-Ray Diffraction Analysis

XRD analysis is a nondestructive technique that was used to investigate the crystallographic structure of the specimens. It was done by irradiating a specimen surface with incident X-rays followed by measuring the scattered intensities as well as angles of the radiation from the specimen surface. Figure 2.12a shows the setup of XRD technique where X-ray radiation focused on the surface of a specimen that fixed on the axis of the spectrometer. The rotation angles are measured, recorded, and plotted against the diffracted radiation. The result is referred to as the specimen X-ray diffraction pattern. Qualitative analysis, lattice constant determination, and/or stress assessment of specimens may all be done using computer analysis of the peak locations and intensities associated with this pattern. The peak angles and profiles are used to determine crystallographic information and structural analysis. Figure 2.12b shows the XRD diffractometer device model XRD-6000/Japan that used in alayzing different specimens in the current project.

The diffracted peaks position (2θ) was employed to study the modification in the structural characteristics such as grain size, lattice parameters (d spacing), dislocation, strain and residual stresses by means of Williamson-Hall plot method [146]:

$$\beta T = \beta D + \beta\varepsilon \dots\dots\dots\dots\dots\dots\dots\dots\dots\dots (2.2)$$

βT :

broading totla due to broding crystallites size and broding strain

βD: *broding crystallites size*

$\beta\varepsilon$: *broding strain*

SFrom Scherer equation $D = \frac{K\lambda}{\beta \cos\Theta}$ ..... (2.3)

Where **βD** is FWHM in radians?

K: shape factor = 0.9

λ: 0.15406 nm in the wavelength source XRD

D: $crystallites\ size$

Θ: Peak position readies

The micro strain give equation

$$\beta\varepsilon = 4\varepsilon \tan\Theta \dots\dots\dots\dots\dots (2.4)$$

Putting eq 2 and 3 in eq 1

$$\beta T = \frac{K\lambda}{D\cos\Theta} + 4\varepsilon \tan\Theta \dots\dots\dots\dots\dots (2.5)$$

As we know $\tan\Theta = sin\theta/cos\vartheta$

Rewrite equation 4 we get

$$\beta T = \frac{K\lambda}{D\cos\Theta} + 4\varepsilon \frac{sin\theta}{cos\vartheta} \dots\dots\dots\dots\dots\dots (2.6)$$

Multiply equation 5 both side $cos\vartheta$

$$\beta T\, cos\,\Theta = \varepsilon(4sin\theta) + \frac{K\lambda}{D} \dots\dots\dots\dots\dots\dots\dots (2.7)$$

Equation 3.7 represent straight line, in which ε is gradient (slope) the line and $\frac{K\lambda}{D}$ is represent the Y intercept.

Consider stander equation straight line represented

$$Y = mx + c \dots\dots\dots\dots (2.8)$$

m: is slope and

c: is intercept **y**

From equation 3.9 calculate grain size **(nm)**

$$c = \frac{K\lambda}{D} \dots\dots\dots\dots (2.9)$$

From equation 3.10 calculate dislocation **(nm^{-2})**

$$\delta = \frac{1}{D^2} \dots\dots\dots\dots (2.10)$$

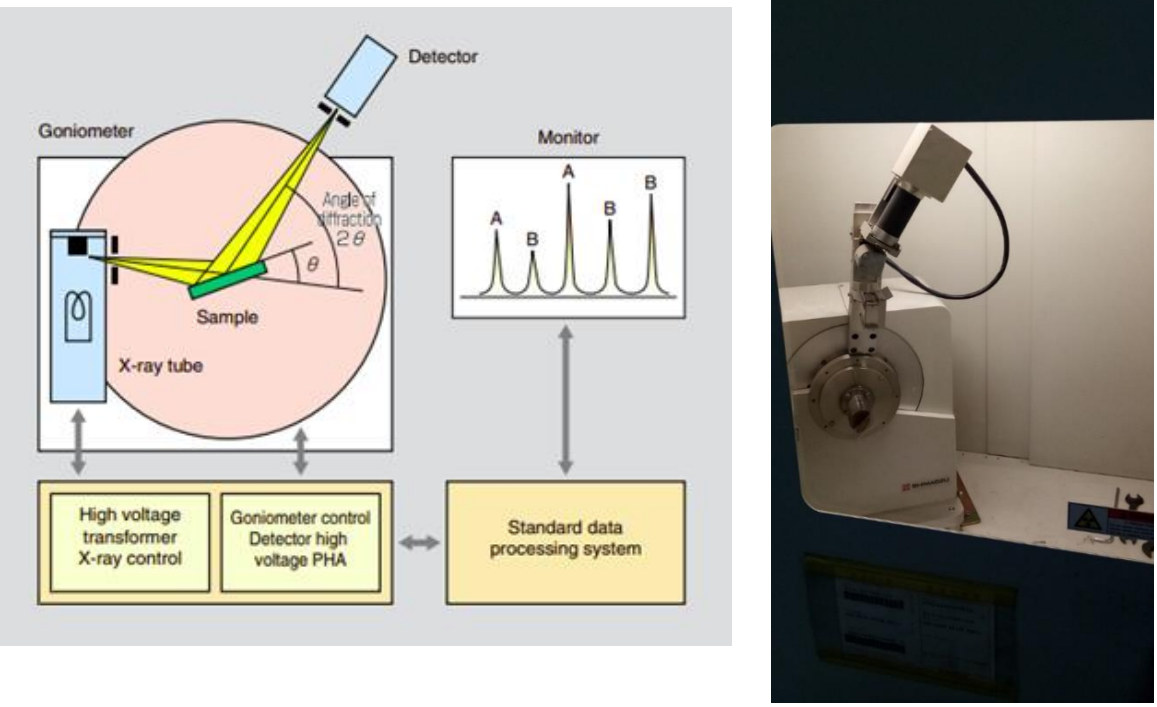

(a) **(b)**

Figure 2.12: a) XRD test setup, b) The (XRD) device type Shimadzu XRD-6000 X-ray diffract meter\Japan.

2.11 Residual Stresses

LSP induces cold working and plastic deformation in the processed zones and this creates beneficial compressive residual stresses. The induced residual stresses contribute in increase the fatigue life and disrupt microcracks initiation and propagation. Residual stresses (σ_r) values were computed according to the following equation [147]:

$$\sigma_r = \frac{\varepsilon}{d}\left(\frac{E}{1+\nu_p}\right) \dots\dots\dots\dots\dots\dots (2.11)$$

where ε is the average strain, E is the modulus of elasticity (MPa), d (nm) is the crystallographic spacing of the un-peened specimen, and ν_p the Poison ratio.

Chapter Three

Results and Discussion

3.1 Introduction

Experimental results including the mechanical tests, imaging observations and structural analysis for the specimens produced by LSP are presented in this chapter. The experimental results were extracted using two methods OFAT and the multi-factor at a time by using BBD based on DOE. Section 3.2 reviews OFM results where the working parameters effects are investigated individually. Section 3.3 reviews BBD results where the effect of two or more working parameters at a time as well as their interaction are investigated. The performance of specimens under cyclic loading were presented by S-N curves in Section 3.4. The built of experimental model and related extracted data are presented in Section 3.5. Based on the built model, the suggested optimization data of LSP process was demonstrated in Section 3.6. The imaging observation for the treated and untreated specimens were demonstrated in Section 3.7. Structure analysis through XRD and induced residual stresses for the treated specimens with LSP and untreated ones were discussed in Sections 3.8.Finally Section 3.9 described the facture status in the cross section for three specimens, the untreated, treated and the optimum specimen.

3.2 One Factor at a Time Results

The obtained results reveal the rise in fatigue life is linked with two considerations. The first is setting the optimum process parameters to build the highest adequate pressure to attain the optimum plastic deformation; this will discuss in the next two section. The second one is the chosen set of process parameters should not yield ablation for the surface of the metal and consequently several unwanted side effects. The induced defects due to improper selection of the optimum process parameters set definitely contributes stress concentrations at the produced defects resulting in early failures. These

defects that yield from laser ablation may be of one or more type such as deposits, pitting, flaws, and solidified particles.

Table 3.1: OFAT results. Input parameters ranges.

Experiments groups	Process parameters ranges			*noc* at different applied stresses (cycle) × 10^4					
	PRR **(kHz)**	***ω*** **(mm)**	***v*** **(mm/s)**	***noc*** **at 263 (Map)**	***noc*** **at 235 (MPa)**	***noc*** **at 222 (MPa)**	***noc*** **at 217 (MPa)**	***noc*** **at 210 (MPa)**	***noc*** **at 205 (MPa)**
Untreated specimens				4.2730	9.2291	10.7492	12.2868	15.0774	18.5082
***PRR*-Group**	20	0.03	350	4.8345	11.0110	20.4176	30.2142	40.2173	42.7030
	21	0.03	350	8.5676	15.7694	21.8180	30.6874	43.4127	51.5210
	22	0.03	350	6.0519	13.0977	20.2323	30.2295	43.8992	49.8992
	22.5	0.03	350	5.6366	9.6338	18.4682	28.0781	38.7946	58.6980
	23	0.03	350	4.7001	10.7170	20.3806	30.2661	41.8734	57.3130
	24	0.03	350	4.6751	10.9021	21.9473	31.2840	41.0226	51.2320
	25	0.03	350	4.7010	10.7176	20.3812	30.2679	41.8743	41.6190
***ω*-Group**	22.5	0.02	350	4.7231	10.8880	20.2106	30.1751	41.9124	62.8245
	22.5	0.03	350	6.0528	13.0981	20.2330	30.2263	43.9007	57.1980
	22.5	0.04	350	4.3779	9.5688	20.1910	30.1435	31.7262	66.8670
***v*-Group**	22.5	0.04	200	10.6520	20.4280	31.2010	40.2430	64.0100	106.9421
	22.5	0.04	250	8.4398	32.1075	39.0646	53.8312	59.1123	81.2572
	22.5	0.04	300	6.3087	12.3049	19.0102	23.7937	29.9368	67.9780
	22.5	0.04	350	5.7584	10.3352	24.0605	31.0834	46.7133	65.9365
	22.5	0.04	400	7.3588	22.3049	37.0135	43.3650	59.3663	77.0027
	22.5	0.04	450	9.1866	39.8145	46.0111	53.4144	69.7188	98.3471
	22.5	0.04	500	13.1230	20.9040	32.6100	43.4310	73.3530	112.0210

The improvement of fatigue life by manipulating the process parameters pulse repetition rate (*PRR*), spot size (ω) and scanning speed (v). The following subsections illustrates the effect of each process parameter individually on the fatigue life represented by the number of cycles under cyclic loading (noc) for a descending spectrum of bending stresses 263, 235, 222, 217, 210, and 205 MPa. Table 3.1 tabulates the results obtained from OFAT method where the specimens are grouped into to three groups based on the varied process

parameter. Also, the table provides a comparison between the treated specimens with LSP and the untreated. The latter is considered a reference for the degree of improvement in noc at different levels of applied stresses.

Under different applied loading from heaviest stress 263 MPa to the lightest one 205 MPa the behavior is almost same. Therefore, discussion of data in the next subsections takes the lightest applied stress 205 MPa where the colored blue column in Table 3.1.

3.2.1 The Effect of Pulse Repetition Rate

The effect of *PRR* on *noc* is outlined by Figure 3.1, the best recorded fatigue life value is 58.698×10^4 cycles when the *PRR* equals 22.5 kHz, at constant values of 0.03 mm and 350 mm/s for ω and v respectively. This optimum value yields a maximum percentage increase in *noc* by 217.15% when compared with the un-peened specimen, which recorded *noc* value equals 18.508×10^3 cycles. The drop in *noc* values at both ends of the curve is related to the intensity approach towards the minimum intensity (I_{min}=1.8 GW/cm^2) and the maximum intensity (I_{max}=2.3 GW/cm^2) at the right end and left end, respectively. Towards I_{min} the laser beam be insufficient to produce the required plasma capable to impart plastic deformation in the metal structure.

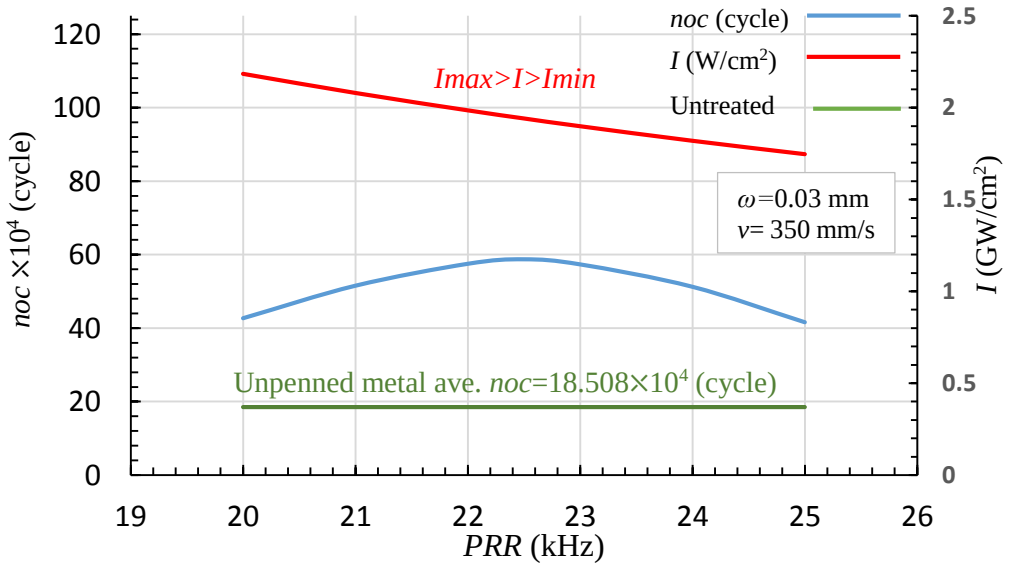

Figure 3.1: The effect of manipulating the *PRR* on the fatigue life at the applied fatigue stress 205 MPa.

3.2.2 The Effect of Spot size

The effect of ω variation on the *noc* show weak effect at constant values for *PRR* and *v* equal to 22.5 kHz and 350 mm/s respectively as seen in Figure 3.2. A slight increase in the *noc* can be observed when the spot size is 0.04 mm, as the percentage increase in *noc* concerning the previous parameter is 261.2%. It is well noticed when the intensity of the laser beam decreases due to larger spot size, the fatigue life be better and this can be related to the absence of the side effect of laser ablation defects which degrades the specimen dynamic performance.

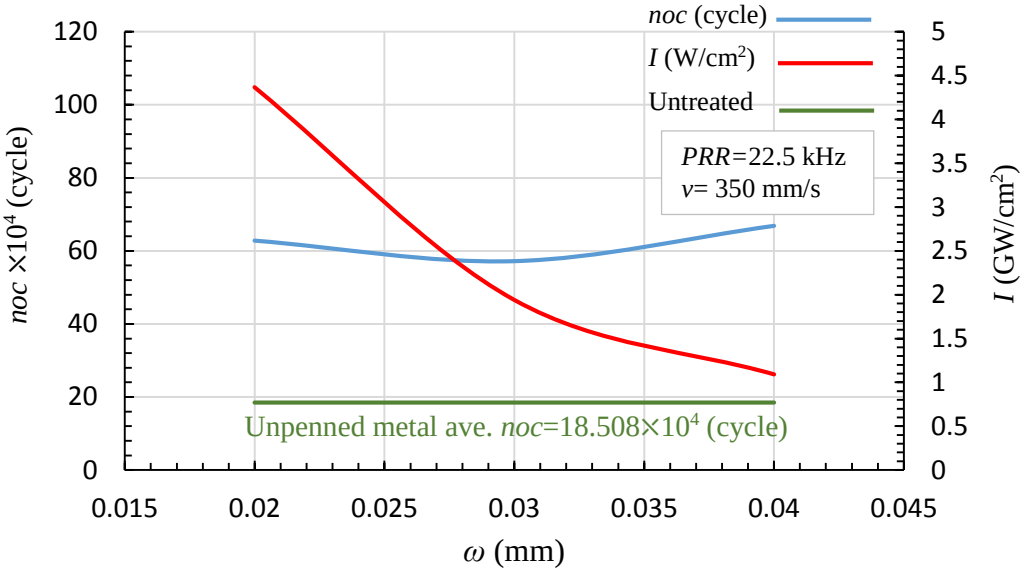

Figure 3.2: The effect of manipulating the ω on the fatigue life at the applied fatigue stress 205 MPa.

3.2.3 The Effect of Scanning speed

The effect of v variation on the *noc* shows a significant effect when the other two parameters *PRR* and ω are at their optimum obtained values to 22.5 kHz and 0.04 mm respectively as seen in Figure 3.3. It can be seen the fatigue life increases significantly as the scanning speed moves towards the minimum or maximum values. When the laser spot scans the working area on the specimen at the lowest or highest speeds, 200 mm/sec or 500 mm/sec, respectively, the

fatigue life is maximized significantly. This behavior can be related to the nature of the laser light interaction with the target at those mentioned speeds. Towards the lower values of *v*, the pulses overlap (*OV*), and the number of pulses per single spot *N* increases, resulting in a lower ablation threshold and an increase in the ablation depth. Such a condition causes complete removal for the black coat resulting in high induced pressure and substrate plastic deformation. On the other side, switching towards higher values of *v* consequently lowers *OV* and *N*, lead to an increase in the ablation threshold, smaller ablation depth and higher black paint removal rate due to a larger ablated transverse area per single pulse [148]. Thus, higher induced pressure is associated with high plastic deformation for the metal surface. The drop in the graph between the maximum and minimum ranges of v is related to the ablation side effect on the base metal, as will be revealed in sections 3.7 and 3.8 .

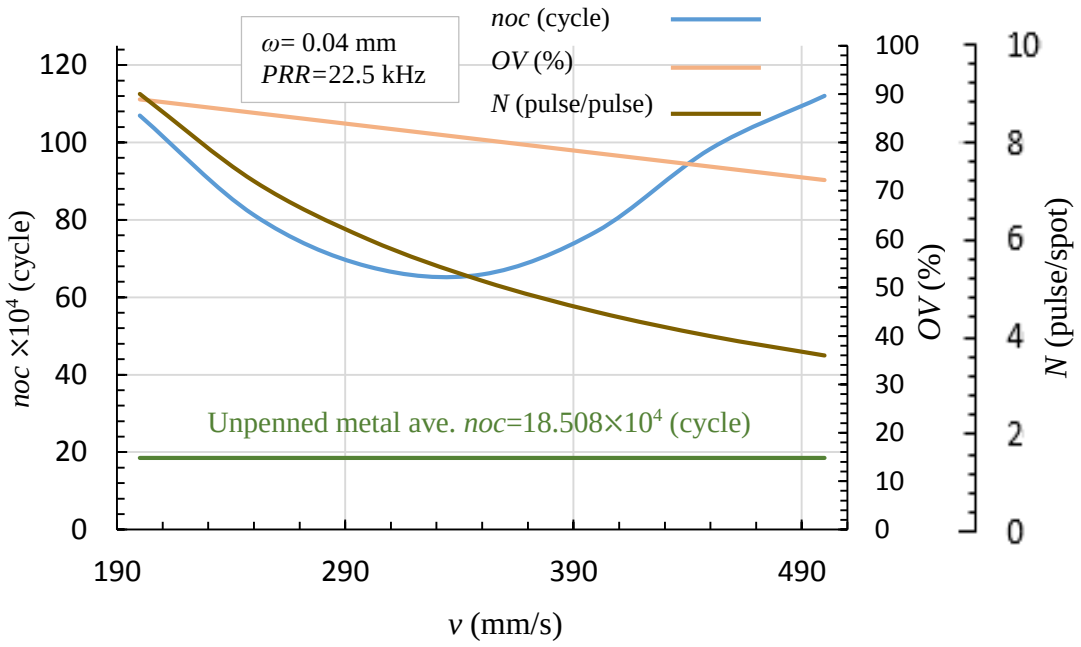

Figure 3.3: The effect of manipulating the *v* on the fatigue life at the applied fatigue stress 205 MPa.

3.2.4 Graphical Demonstrating of Groups

3.2.4.1 Bar Charts

The bar chart shown in Figure 3.4 offers data comparison between the three process parameters among groups of *PRR*, *ω* and *v* as well as untreated group. The high speed scan of the laser spot on the working area on the specimen both sides when the other parameters are set on their optimum values yield the highest fatigue life at all. The percentage increase in the fatigue life when the untreated specimen considered as a reference is illustrated in Figure 3.5

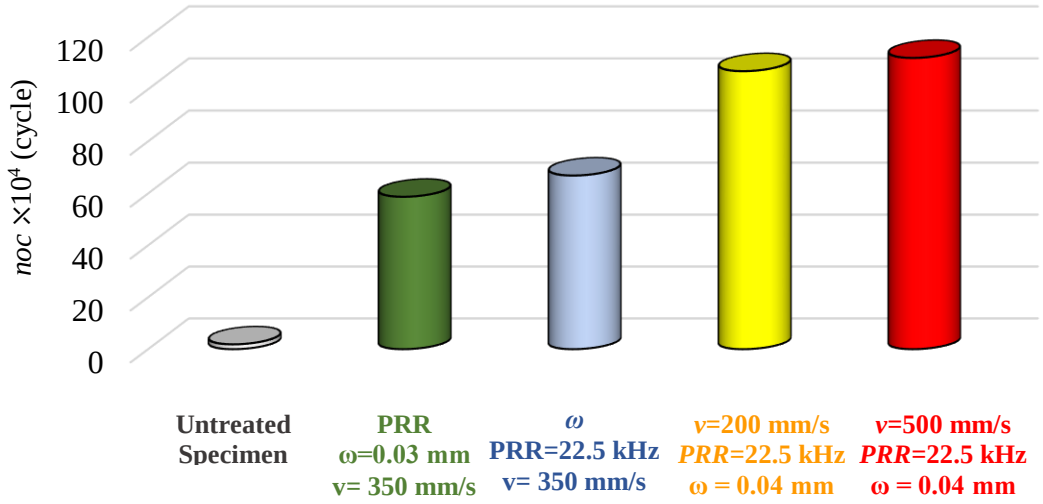

Figure 3.4: The total effect of *v* on noc compared among other effects of process parameters at the applied fatigue stress 205 MPa.

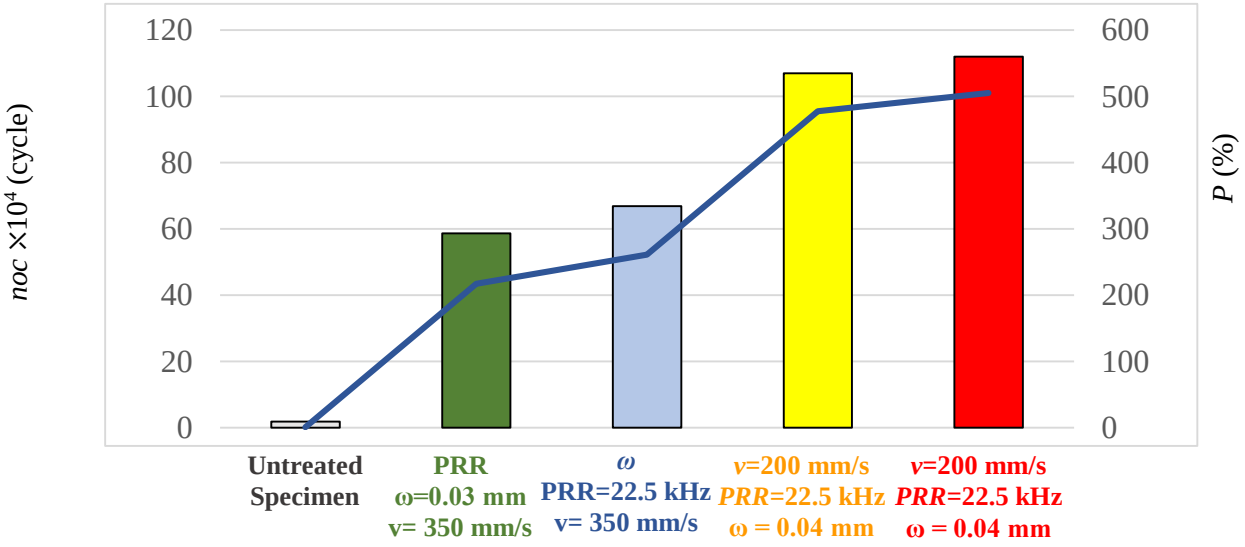

Figure 3.5: The percentage increase in the fatigue life when the untreated specimen considered as a reference at the applied fatigue stress 205 MPa.

3.2.4.2 Box Plot Graph Analysis

The box plot graph in Figure 3.6 displays the variability, outliers, symmetry of data, and distributions between the three groups of process parameters of LSP data. The absence of overlap between the three boxes of data (*PRR*, ω and *v*) indicates variability and differences in the obtained data, which is considered good. The more extended box and wider whiskers of group *v* mean the data is dispersed noticeably dispersed compared with the two other boxes. Box ω is shorter in terms of box length and range of whiskers, meaningless dispersed data and the lowest impact on results. For the three boxes, the whisker's height is shorter than 1.5 times the interquartile range, which indicates there is no exist for outlier data. The groups PRR and ω show the unsymmetrical data distribution where the median and the whiskers are approximately the same on both sides. Unlike the latter groups, group v shows the asymmetrical, positively skewed data distribution. The median is closer to the bottom of the box, and the whisker is shorter on the lower end of the box.

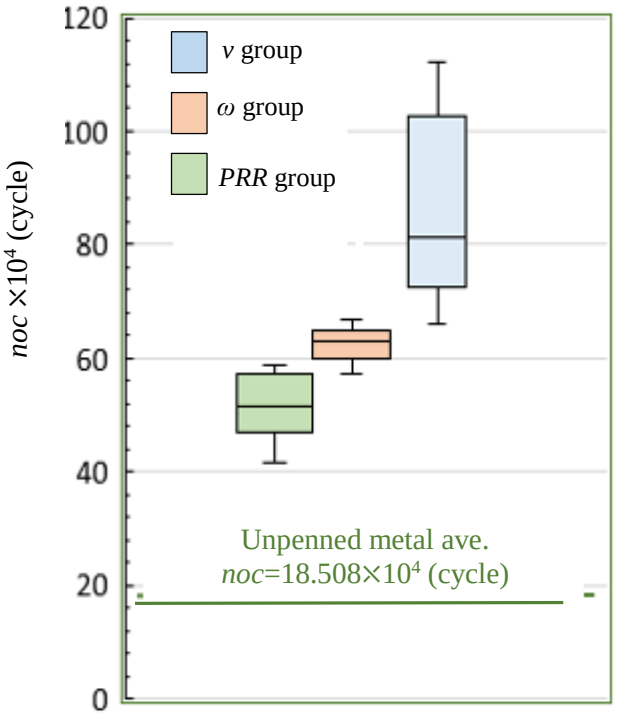

Figure 3.6: Data analysis via boxplot graph extracted at applied fatigue stress 205 MPa.

3.3 The Results of BBD Based on RSM

The objective of employing BBD in the current study is to attain many goals especially apply mathematical and statistical analysis for the process parameters and their interactions, build an experimental model and optimize the process. The experimental design considered seventeen experiments of three levels for the three independent input parameters (*PRR*, ω, and *v*).

Among the seventeen experiments. Table 3.2 presents the average fatigue life value of six specimens for each set of parameters group subjected to different loads as well as the raw metal noc values two of them show significant fatigue life namely experiments 6 and 16. It could be deduced from both experiments the *PRR* of 22.5 and ω of 0.04 mm are the optimum operating conditions at the upper and lower scanning speed *v* values of 200 mm/s and 500 mm/s. Compared with untreated specimens, *noc* for these two sets of parameters recorded a percentage increase in fatigue life of 505.25% and 477.81% for experiments 6 and 16, respectively, as seen in Figure 3.7

Table 3.2: BBD for extraction the response values for fatigue life.

Experiment No.	Parameters values (Coded values)			Responses: Average fatigue life (noc) × 10^4 (cycle)					
	PRR **(kHz)**	***ω*** **(mm)**	***v*** **(mm/s)**	**noc at 263 (Map)**	**noc at 235 (MPa)**	**noc at 222 (MPa)**	**noc at 217 (MPa)**	**noc at 210 (MPa)**	**noc at 205 (MPa)**
	Raw specimens (not processed)			4.273	9.229	10.749	12.286	15.077	18.508
1	22.5 (0)	0.03 (0)	350 (0)	5.636	9.633	18.468	28.078	38.794	46.812
2	22.5 (0)	0.03 (0)	350 (0)	6.052	13.098	20.233	30.226	43.900	57.098
3	25 (1)	0.04 (1)	350 (0)	4.701	10.717	20.381	30.267	41.874	57.619
4	25 (1)	0.03 (0)	500 (1)	8.568	15.770	21.818	30.688	43.413	51.920
5	25 (1)	0.03 (0)	200 (-1)	4.676	10.903	21.948	31.284	41.023	51.164
6	22.5 (0)	0.04 (1)	500 (1)	13.123	20.904	32.610	43.441	73.353	112.021
7	22.5 (0)	0.02 (-1)	500 (1)	3.760	9.598	19.013	24.047	30.297	38.351
8	20 (-1)	0.04 (1)	350 (0)	4.834	11.011	20.417	30.214	40.217	50.703
9	22.5 (0)	0.02 (-1)	200 (-1)	4.746	10.433	20.812	29.850	40.661	50.106
10	22.5 (0)	0.03 (0)	350 (0)	6.052	13.098	20.233	30.230	43.900	57.098
11	22.5 (0)	0.03 (0)	350 (0)	62.112	10.343	18.757	26.992	36.890	51.329
12	22.5(0)	0.03 (0)	350 (0)	5.120	11.250	13.601	22.551	31.489	50.226
13	20 (-1)	0.02 (-1)	350 (0)	4.378	9.569	20.191	30.144	31.727	54.378
14	20 (-1)	0.03 (0)	500(1)	4.046	10.253	19.050	23.986	34.063	44.319

15	20 (-1)	0.03 (0)	200 (-1)	4.691	11.914	22.453	29.870	40.263	49.000
16	22.5 (0)	0.04 (1)	200 (-1)	10.652	20.428	31.201	40.243	64.010	106.942
17	25 (1)	0.02 (-1)	350 (0)	4.378	9.569	20.191	30.144	31.723	54.378

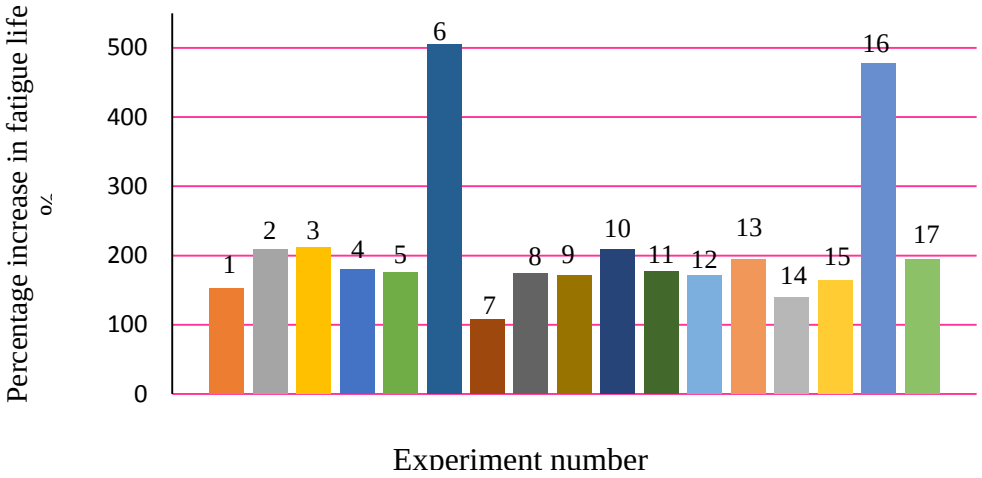

Figure 3.7: The percentage increase in fatigue life for the processed specimens at an applied stress of 205 MPa.

The experimental data was represented on boxplot graphs to discover their variability or dispersion, outliers and symmetry of the process parameters at their three levels determined by the software. Boxplots graph in Figure 3.8 show the impact of each input parameter at its three levels on data characteristics and distribution. The high level of ω demonstrates more different amounts when compared with the other two parameters *PRR* and *v*, as seen in Figure 3.8a. On the other hand, the other two levels of ω exhibit no effect of variability of the response and shorter whiskers. The more significant variability for *noc* data and wider whiskers can be observed at least for two levels of the *v* parameters as shown in Figure 3.8b. No outlier was observed where the whiskers length is shorter than the 1.5 times the interquartile range. The longer boxes of low and high levels for *v* indicates wider distribution, that is, more scattered data. Figure 3.8c demonstrates less distribution and outlier data for the three levels of the parameters *PRR*. The median lines of the three boxplots overlap with their adjacent boxplots, and then there is likely to be no

effective differences between the three levels. For all three graphs, it can be seen that most of the boxplots for the three parameters are skewed (asymmetric) and don't follow a normal distribution.

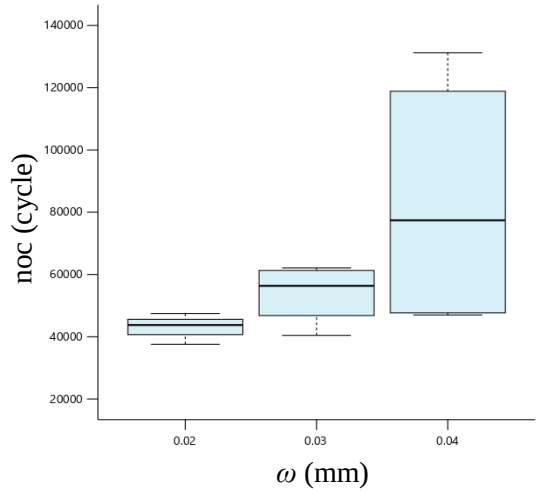

(a)

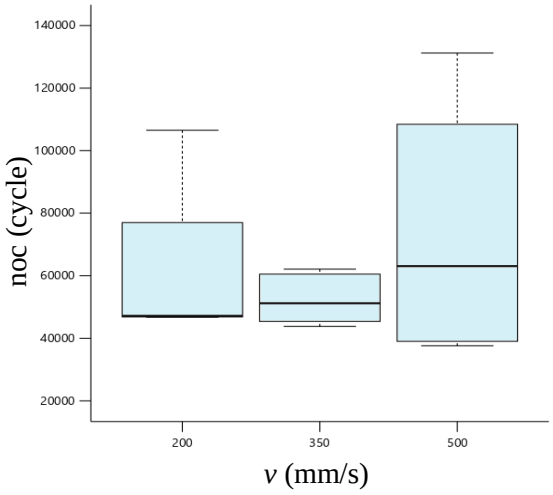

(b)

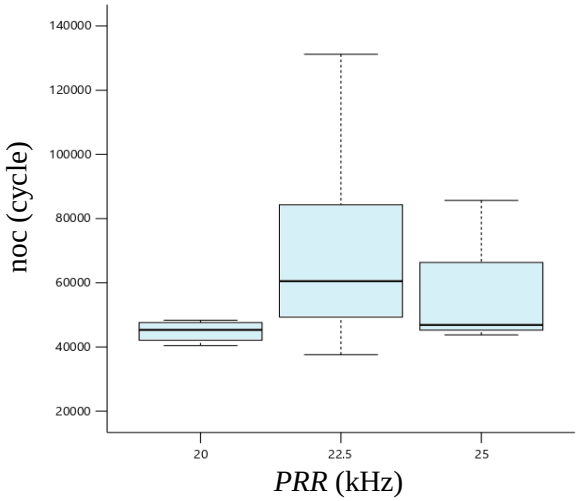

(c)

Figure 3.8: Boxplots representation for the distribution of data at three levels for each input parameter: a) *ω*, b) *v* and c) *PRR* at an applied stress of 205 MPa.

3.4 Experimental S-N Curves

The fatigue test was applied using the alternating bending device for 306 the untreated and peened specimens classified into 18 groups by applying a bending load at their free end. Each group of process parameters was divided into six subgroups to load it with different predefined fatigue stresses. Namely, fatigue stresses 263, 235, 222, 217, 210 and 205 MPa. Figure 3.9 presents the S-N curves data for the fatigue life represented by *noc* versus the applied stress of 205 MPa for the untreated and peened specimens processed by different sets of process parameters. It is seen that the untreated samples have limited life compared with treated samples by any group of process parameters. Figure 3.9a shows manipulating the PRR value has a good enhancement in *noc*, especially at 22.5 kHz; however, it is still considered limited for any value of *PRR*. Variation of ω shows convergent results for noc at different applied loads as Figure 3.9b depicts. The significant impact factor on the fatigue life is the *v* when it sets at a low value of 200 mm/s and becomes better at the higher value of 500 mm/s, as shown in Figure 3.9c.

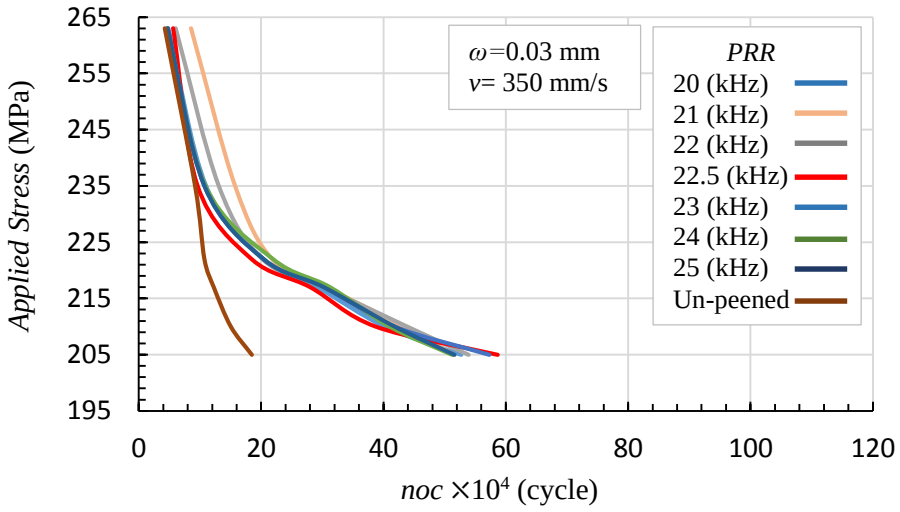

(a)

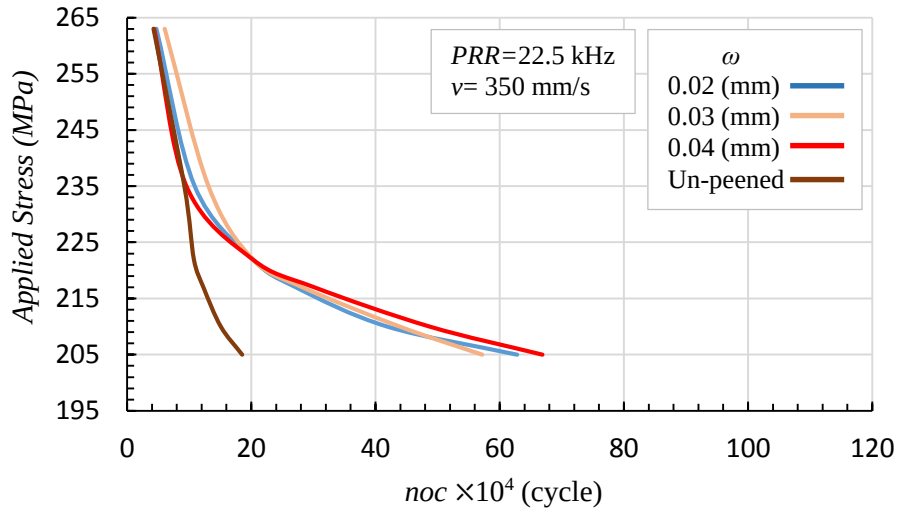

(b)

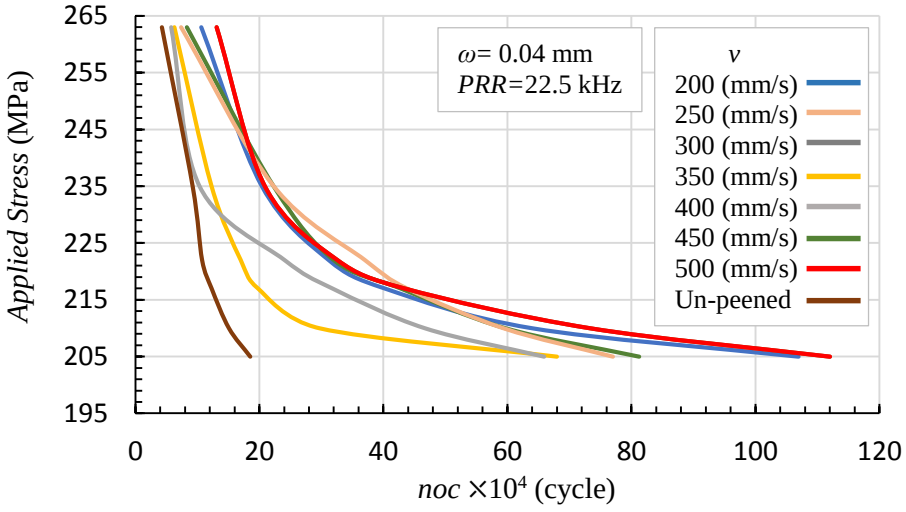

(c)

Figure 3.9: S-N curves for the three varied parameters: a) PRR, b) ω, and c) v.at the applied fatigue stress 205 MPa.

3.5 Model Analysis

BBD based on RSM with three independent parameters as input variables and their interactions was utilized to develop the response surface models and their interactions. The response surface was tailored to fit the experimental results obtained from the executed experiments. The models predict found the responses *noc* at the various combination of working parameters *PRR*, ω and *v*. The adequate model without aliased terms after eliminating some combinations of nominal and weird words.

Axiomatically, all of the responses for *noc* at different applied stresses show different values but approximately the same behavior when modelled. Thus, one of these models will be presented in the current section is enough to reflect the general conduct of fatigue lives at different applied stresses. The following analysis for the obtained model and optimization is related to the response at the applied pressure of 205 MPa. It is worth to mention the quadratic model was failed to represent the significance of the build model and its related input parameters. This may be related to the nature of obtained data in term of two significant results among almost the same level of data for the others. The cubic model handles the situation after elimination some diagnosed aliased combinations of input parameters. The mathematical model that benefits for predicting the response *noc* as a function of a set of the input parameters *PRR*, ω and *v* is as follow:

$$noc = -2.13 \times 10^{6} + 1.52 \times 10^{5}\, PRR + 7.72 \times 10^{6}\, \omega + 5.05 \times 10^{3}\, v - 114.11\, PRR.v - 89.3 \times 10^{3}\, \omega.v - 3.05 \times 10^{3}\, PRR^{2} + 1.7 \times 10^{8}\, \omega^{2} - 8.76\, v^{2} + 0.206\, PRR.v^{2} - 3 \times 10^{5}\, \omega^{2}.v + 161\, \omega.v^{2} \ldots\ldots\ldots (3.1)$$

One-way Analysis of variance test (ANOVA) was applied for the reduced cubic model given in Table 3.3 to test the null hypothesis and analyze the statistically significant differences between the means of variables. The F-value of 58.36

for the developed model implies the model is significant. There is only a 0.01% chance that this large F-value occur due to noise. The observed significant p-value of 0.0001 makes both terms of the model are significant. Among the duration of three input parameters, the *v* is found effective for both F-value and p-value. Likewise, the combinations of input parameters were found significant except the term $\omega.v^2$ was insignificant where the p-values greater than 0.10. The Lack of Fit F-value of 0.0228 implies that the Lack of Fit is unimportant relative to the pure error. There is a 88.73% chance that a Lack of Fit F-value this large could occur due to noise. Non-significant lack of fit is a good value to the model fit.

Table 3.3: ANOVA test for noc at applied stress of 205 MPa.

Source	Sum of Squares	df	Mean Square	*F*-value	*p*-value	
Model	1.013×10^{10}	11	9.207×10^{8}	58.36	0.0001	significant
PRR	4.469×10^{5}	1	4.469×10^{5}	0.0283	0.8729	
ω	1.514×10^{7}	1	1.514×10^{7}	0.9593	0.3723	
v	2.637×10^{8}	1	2.637×10^{8}	16.71	0.0095	
$PRR\,.\,\omega$	5.146×10^{8}	1	5.146×10^{8}	32.62	0.0023	
$\omega\,.\,v$	2.984×10^{8}	1	2.984×10^{8}	18.91	0.0074	
PRR^2	1.533×10^{9}	1	1.533×10^{9}	97.16	0.0002	
ω^2	1.870×10^{8}	1	1.870×10^{8}	11.85	0.0184	
v^2	1.063×10^{9}	1	1.063×10^{9}	67.36	0.0004	
$PRR\,.\,v$	2.691×10^{8}	1	2.691×10^{8}	17.06	0.0091	
$\omega.v^2$	3.896×10^{7}	1	3.896×10^{7}	2.47	0.1769	
$\omega^2 v$	2.624×10^{9}	1	2.624×10^{9}	166.3	<0.0001	
Residual	7.889×10^{7}	5	1.578×10^{7}			
Lack of fit	4.469×10^{5}	1	4.496×10^{5}	0.0228	0.8873	not significant
Pure error	7.844×10^{7}	4	1.861×10^{7}			
Cor Total	1.021×10^{10}	16				

The fit statistics reveal an R^2 value of 0.9923 close to unity and has good agreement with an adjusted R^2 value of 0.9753. The Adequate Precision (Adeq) value measures the signal to noise ratio. The model shows an Adeq Precision value of 28.049, where a ratio greater than 4 is desirable. This can give an indication that the model could be used to navigate the design space. Figure 3.10 shows the distribution of the actual data points of the response depicted

by the experiments on each run versus the predicted values evaluated by the model. It can be seen data points distributed along the 45° line indicating good agreement of experimental and expected results by the model.

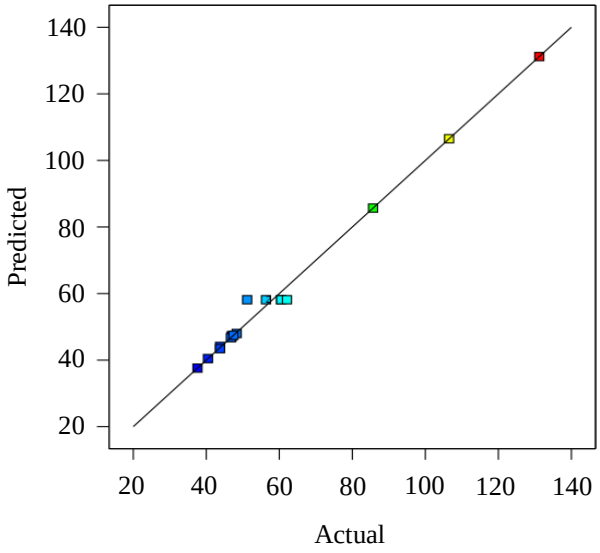

Figure 3.10: Plot of predicted vs. actual data of the modified model in *noc*.

According to the experimental results and statistical analysis, RSM plots are obtained for the three-dimensional graphs (3D) of the response *noc* as a function of two or more input parameters. Figure 3.11 defines in 3D graph and contour plot the values of *noc* at a combination of two input parameters for a certain set value for the third one. The effect of *PRR* and ω for a fixed value of v=200 mm/s is illustrated in Figure 3.11a. The impact of *PRR* and ω on the fatigue life indicated that *noc* was maximum at ω=0.04 mm and PRR= 22.5 kHz. It is clear that *noc* has increased with increasing ω and *PRR* towards the maximum and moderate values respectively. For the same graph, if v switched to average values of 350 mm/s, the response surface decreases before increasing to the maximum at v=500 mm/s. High scanning speed results in a high cooling rate and low interaction time with the target, resulting in less roughness and high hardness. Appendix B presents the 3D response plots at the other applied stresses: 263, 235, 222, 217 and 210 MPa.

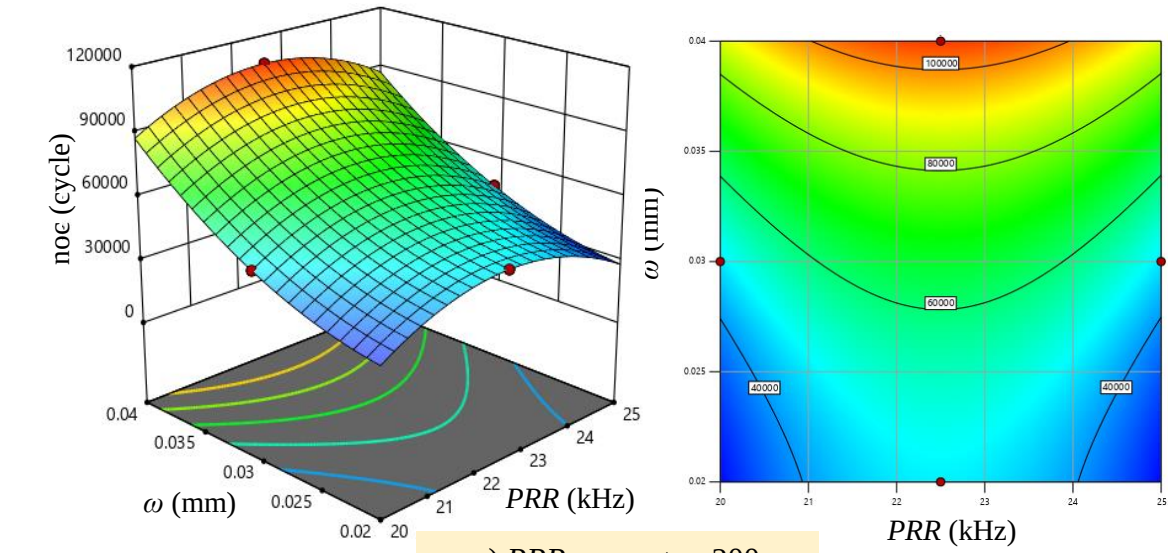

a) *PRR* vs. ω at v=200

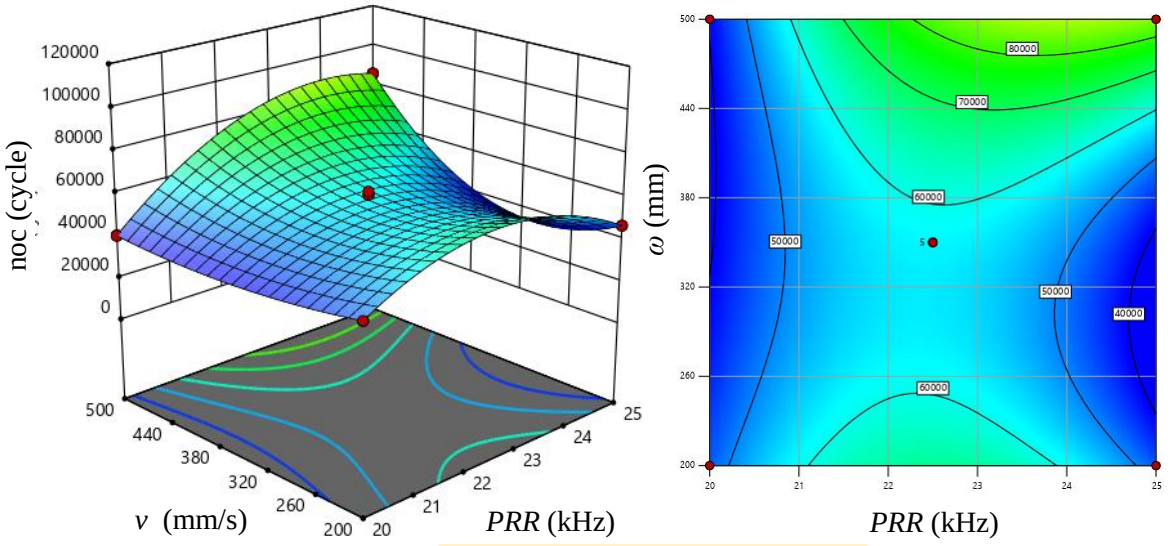

b) *PRR* vs. v at ω=0.03 mm.

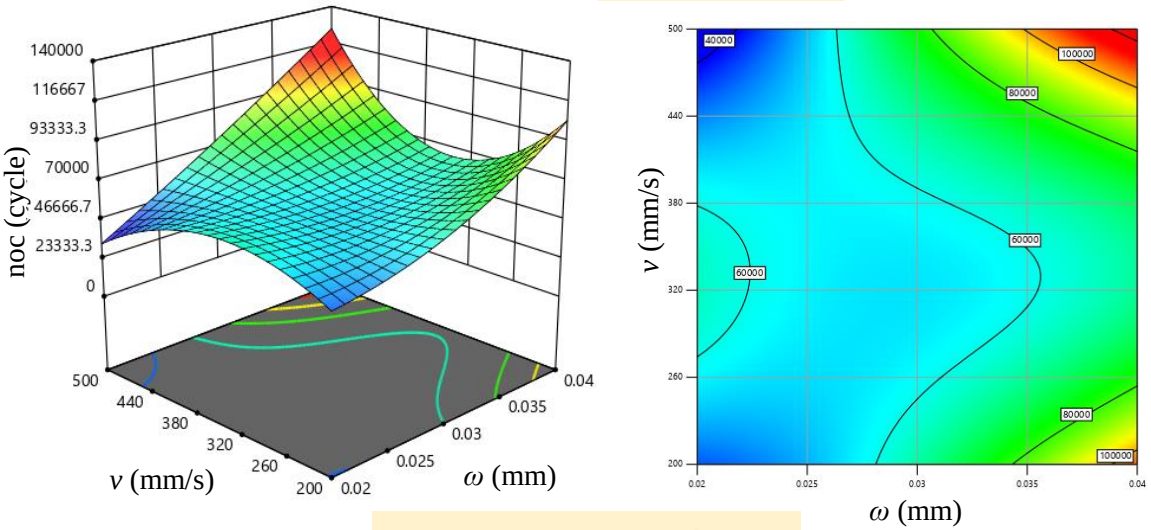

c) ω vs. v at *PRR*=22 kHz.

Figure 3.11: 3D response plots for noc at applied stress of 205 MPa.

When the speed declines, the interaction time increases, and the cooling rate decreases, resulting in increased surface roughness accompanied by lower hardness [149]. The effect of *PRR* and *v* on the response, at fixed value of ω=0.03 mm, is depicted in Figure 3.11b. Moving *PRR* from the moderate to high values gives higher values of *noc* at the terminals of *v* equals to 200 mm/s and 500 mm/s. Changing the value of ω to the minimum lowers the response surface down and vice versa. The induced compressive residual stresses at the surface obviously increases for a certain depth with increasing ω [148].

The effect of ω and *v* on the *noc* when the *PRR* at 22 kHz is shown in Figure 3.11c. The *noc* shows two significant peaks when ω= 0.04 mm and *v* is at the maximum or minimum values. Lowering the value of *PRR* lowers the response surface and keep the same pattern. This may be related to plasma formation rule related to the laser intensities value. At low intensity of less than 1 GW/cm^2 LSP is not verified. At moderate range of 1 GW/cm^2 to 7 GW/cm^2, the plasma pressure reaches its maximum limit. When the intensity increases above 7 GW/cm^2, plasma saturation and light shielding occur [150].

3.6 Optimization of LSP Process

To enhance the fatigue life efficiency, the optimum suggested operating parameters were introduced by the model as shown in Figure 3.12. In the criteria of optimization, three optimized conditions were extracted out by setting three different criteria:

a) Maximum response could be attained for *PRR* range of 22 - 25 kHz and ω range of 0.35 – 0.04 when the experiment operates at *v* of 500 mm/s as shown in Figure 3.12a.

b) Figure 3.12b shows it is possible maximize the response through two conditions at constant value of ω equals to 0.04 mm and *PRR* range of 21 – 25

kHz. The highest one is when *v* equals 500 mm/s and the lowest one at *v* equals to 200 mm/s.

c) To maximize the response Figure 3.12c reveals two sets optimized conditions at PRR of 25 kHz. The largest one when the *v* equals 500 mm/s and ω=0.04 mm and the smaller one when the *v* equals 200 mm/s for same value of ω.

3.7 SEM images and EDS Analysis

SEM images and EDS analysis results for the surfaces of three types of processed specimens: untreated specimens, the optimum among all peened specimens of all groups and an inferior specimen that failed at moderate *noc* are shown in Figure 3.13. An SEM image for the texture of an untreated specimen where all illustrations share the same appearance before applying LSP as shown Figure 3.13a. The selected optimum specimen was elected on the condition of the maximum conducted fatigue life, the highest microhardness of about 75.15 HV and conditioned by ablation defect-free metal surface as the SEM in Figure 3.13b illustrates. The EDS test for the optimum specimen shows that aluminum is still the dominant element on the metal surface, reflecting evidence for no phase changes.

On the other hand, Figure 3.13c shows the opposite features for the optimum specimens in terms of noticeable surface ablation, which is considered the defect behind the moderate fatigue life. Surface ablation induces flaws and micro-cracks or other minor flaws (pits and voids) that reduce specimens' performance under cyclic loading during a fatigue test. The EDS analysis shows a severe reduction in the aluminum element at the metal surface, indicating phase changes at the surface.

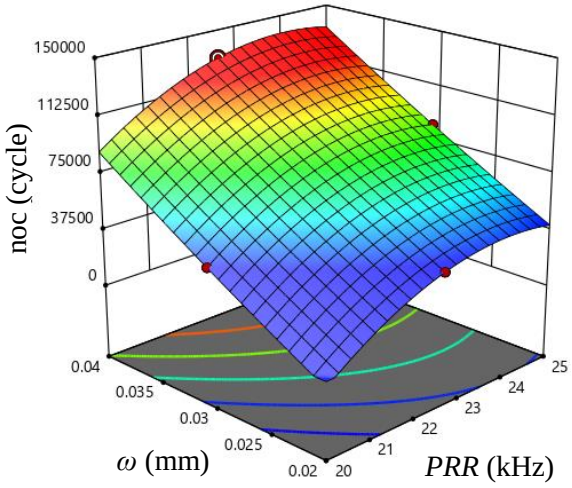

(a) *PRR* vs. ω at v=500 mm/s.

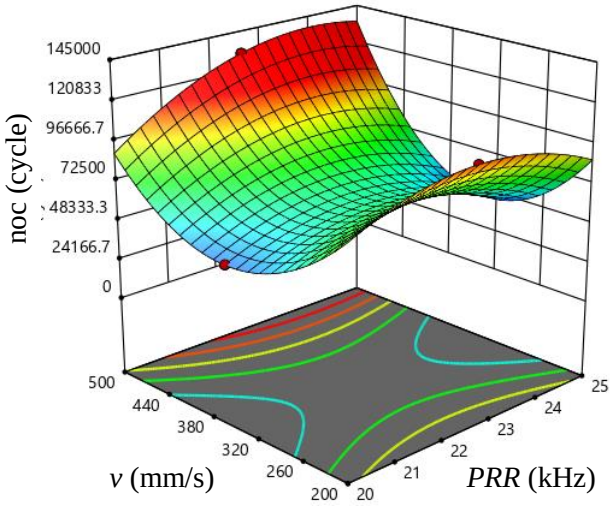

(b) *PRR* vs. v at ω=0.04 mm.

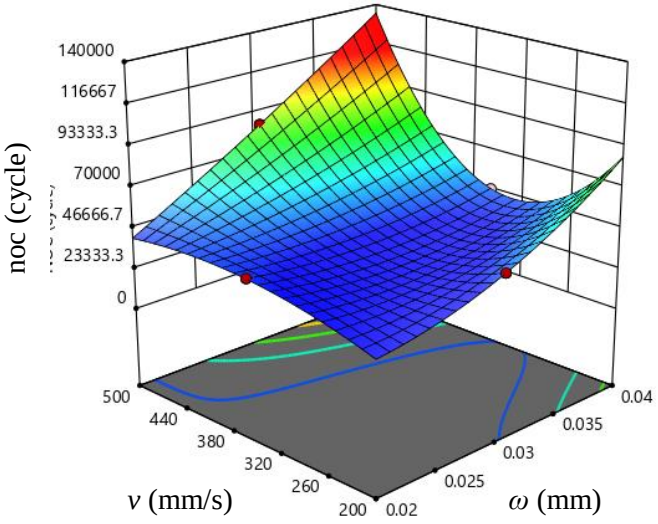

(c) v vs. ω at *PRR*=25 kHz.

Figure 3.12: 3D response plots for desired response values.

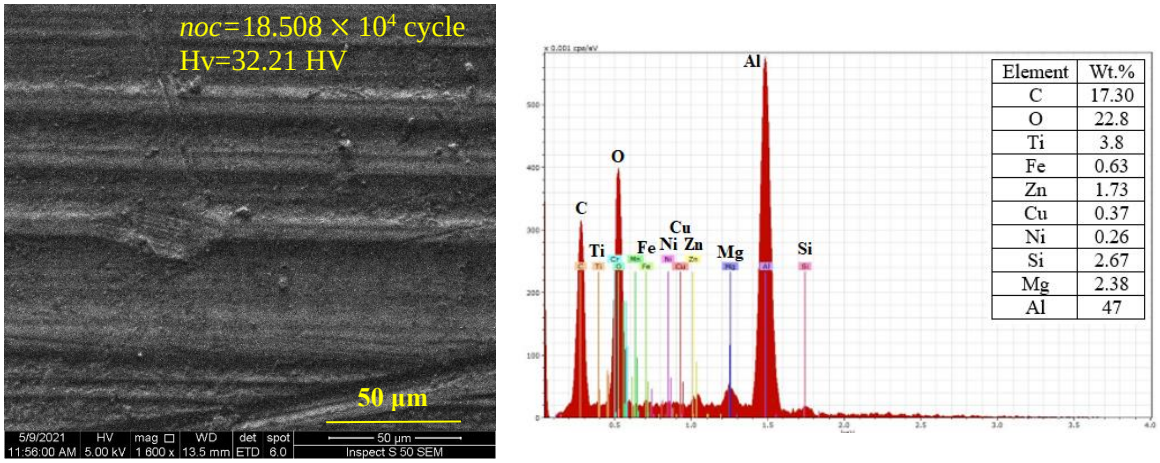

Element	Wt.%
C	17.30
O	22.8
Ti	3.8
Fe	0.63
Zn	1.73
Cu	0.37
Ni	0.26
Si	2.67
Mg	2.38
Al	47

(a) Untreated Specimen

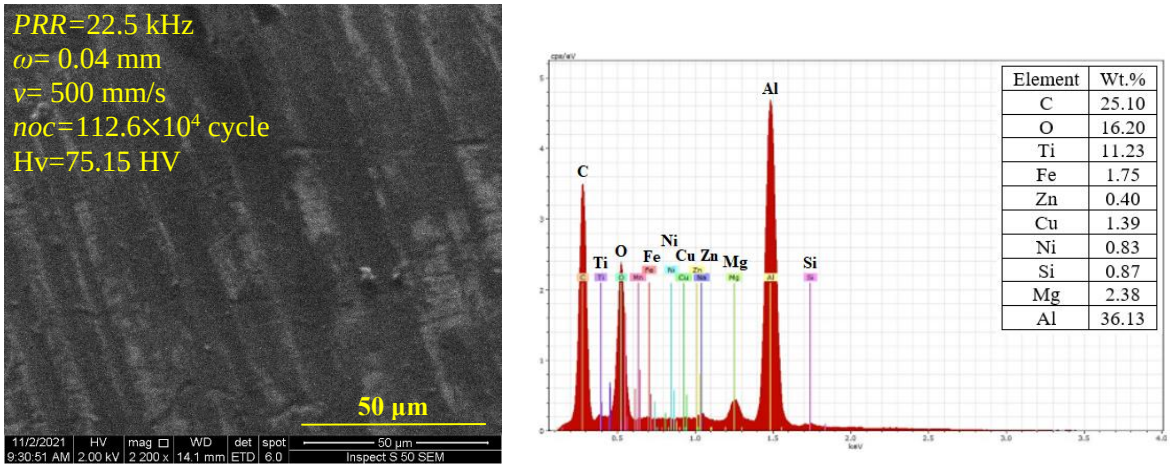

Element	Wt.%
C	25.10
O	16.20
Ti	11.23
Fe	1.75
Zn	0.40
Cu	1.39
Ni	0.83
Si	0.87
Mg	2.38
Al	36.13

(b) Optimum Peened Specimen

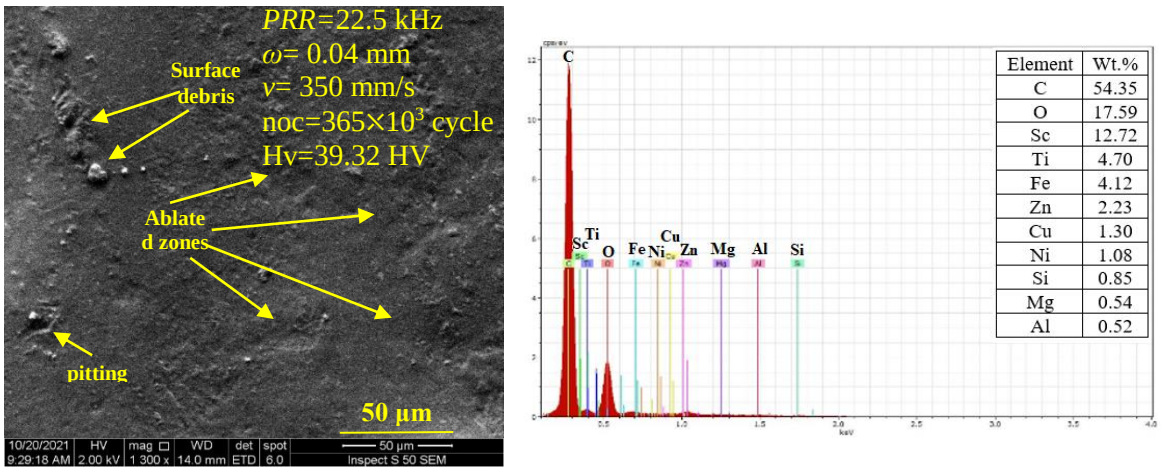

Element	Wt.%
C	54.35
O	17.59
Sc	12.72
Ti	4.70
Fe	4.12
Zn	2.23
Cu	1.30
Ni	1.08
Si	0.85
Mg	0.54
Al	0.52

(c) Inferior Peened Specimen

Figure 3.13: SEM images and EDS analysis for the surfaces of: a) untreated specimen, b) the optimum peened specimen, and c) The inferior peened specimen.

3.8 Structure Analysis, XRD and Residual Stresses

The obtained XRD results reveal narrow and broader diffraction peaks for the un-peened and the optimum peened specimens, respectively, as shown in Figure 3.14. The test indicates no new diffraction peaks due to the LSP process, which means no new diffraction peaks, new crystalline phases, and no new chemical composition. The latter with the peak position (2θ) was employed to study the modification in the structural characteristics such as grain size, lattice parameters (d spacing), dislocation, strain and residual stresses using the Williamson-Hall plot method From **Figure 3.15** plot $\beta T\, cos\, \Theta$ $y - axise$ with $4sin\theta$ X-axis untraded and trade specimens **m** is represent slop straight line it value $\boldsymbol{\varepsilon}$. Appendix C illustrates the XRD result sheets for the untreated and treated specimens. Table 3.3 tabulates the information calculated from the data of the XRD test based on a comparison between the un-peened and peened specimens that recorded the highest fatigue life. The effect of the sequential shots of laser pulses at the upper layers of the peened specimen causes a noticeable reduction in the grain size by a percentage of 28.56% and the induced strain of -634.9 and length dislocations.

LSP induces cold working and plastic deformation in the processed zones, creating beneficial compressive residual stresses in the optimum specimens. The induced residual stresses increase fatigue life and disrupt micro crack initiation and propagation. Figure 3.16 shows the residual stresses graphs as a function of depth for both un-peened specimens and peened specimens by the optimum process conditions. The graph reveals low value of compressive residual stresses of -29 MPa for the un-peened specimen. Compared with the latter, the peened specimen recorded noticeable compressive residual stresses at the surface of -370 MPa. At depth of 300 μm beneath the metal surface the compressive residual stresses were -342.6 MPa. The value of residual stresses reduces along the depth beneath the surface reaching to a total depth of 700 μm.

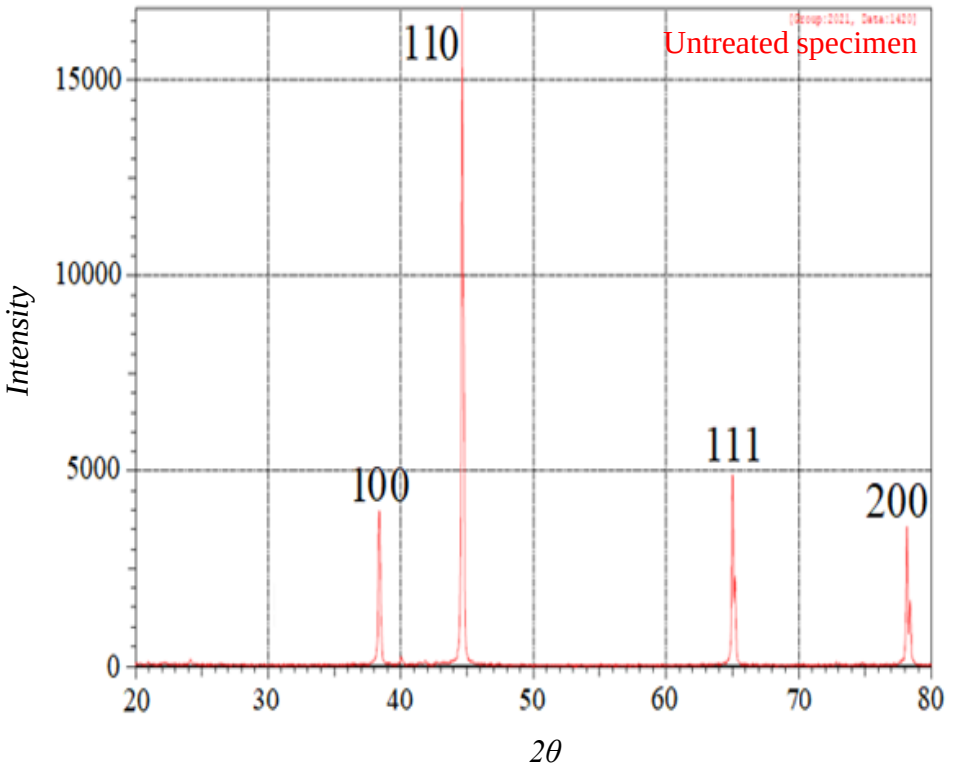

(a)

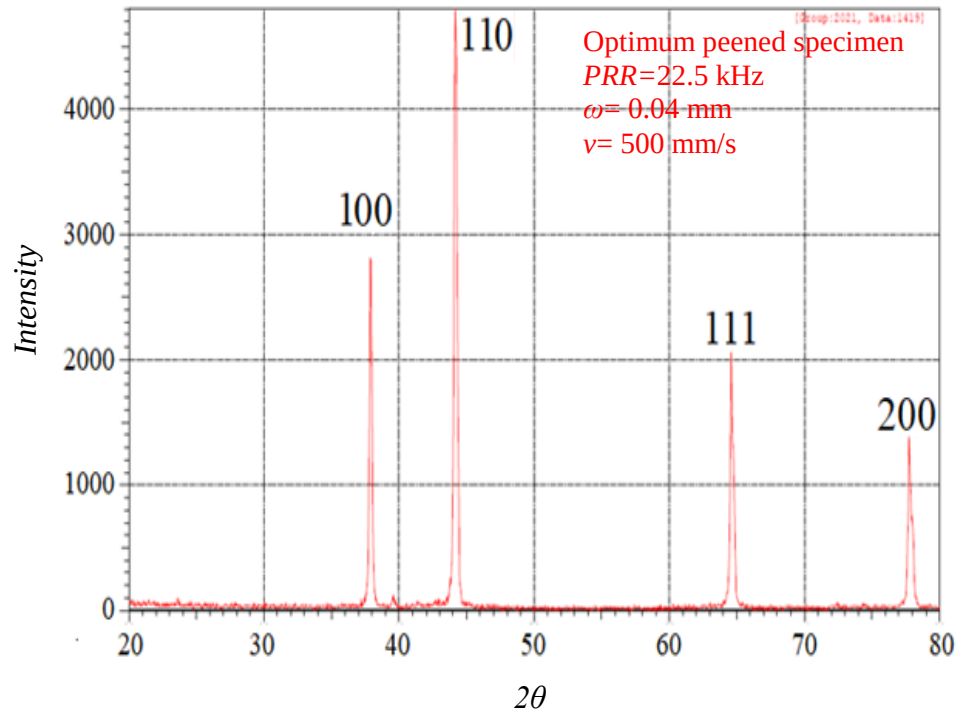

(b)

Figure 3.14: XRD results for: a) un-peened specimen and b) peened specimen at the optimum conditions (PRR=22.5 kHz, ω= 0.04 mm and v= 500 mm/s).

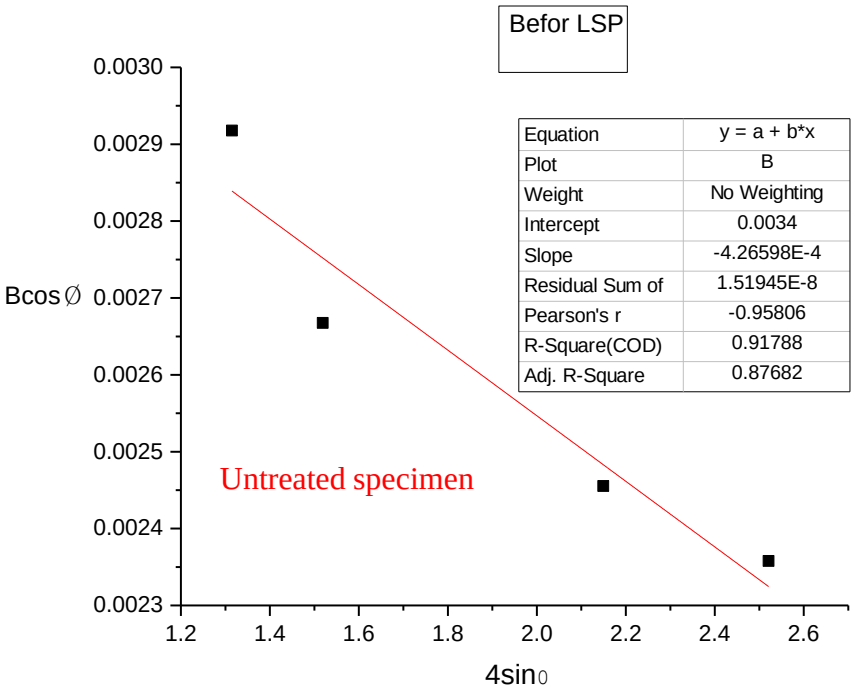

(a)

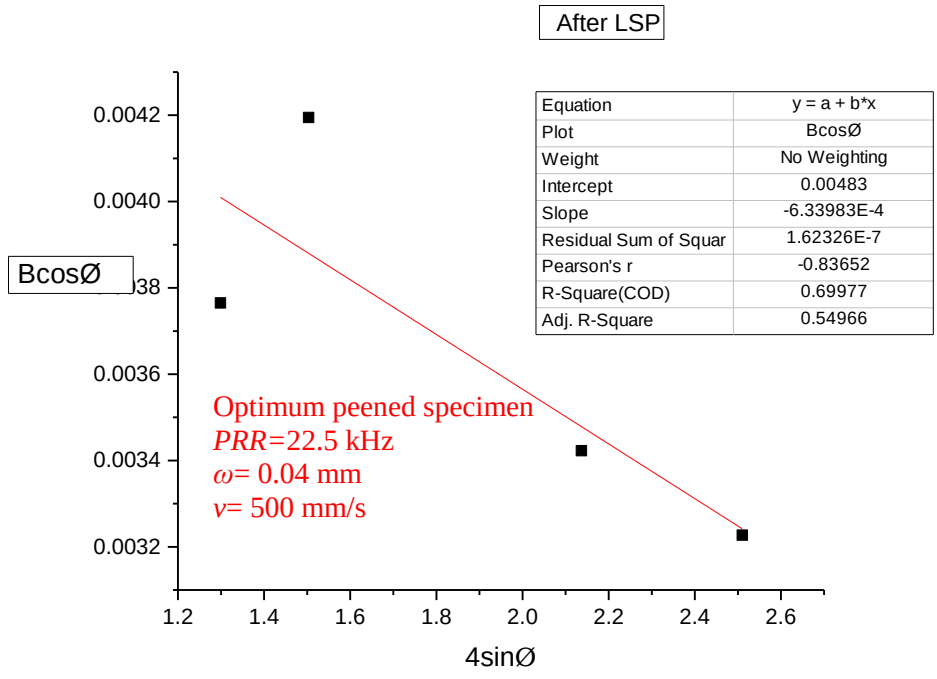

(b)

Figure 3.15: plot $\beta T\cos\theta$ $y-$ *axise* with $4\sin\theta$ X-axis

Residual stresses (σ_r) values were computed according to the following equation 2.4.

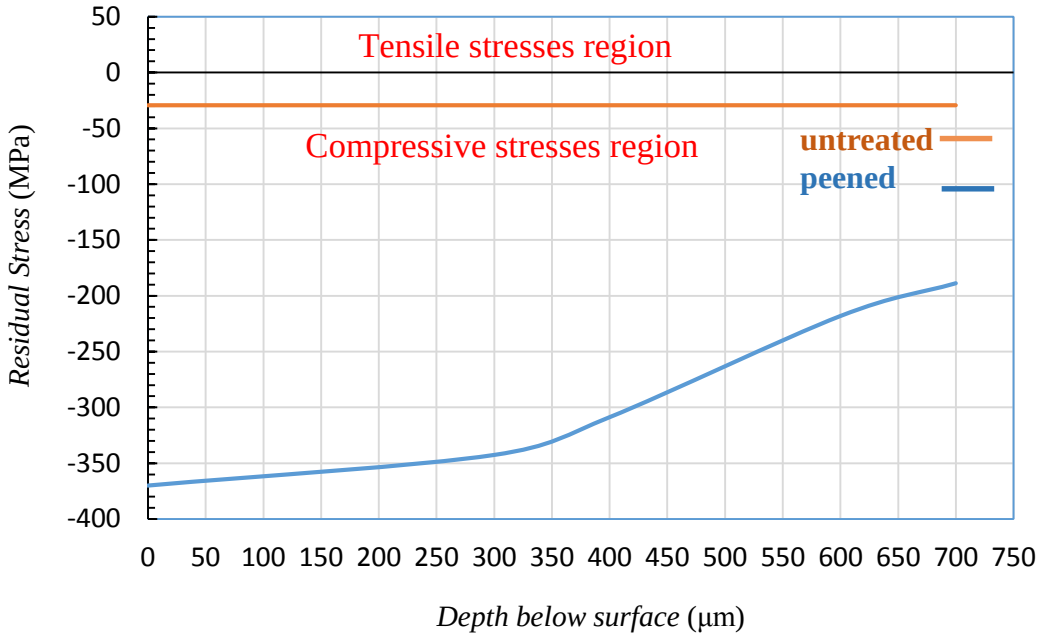

Figure 3.16: Compressive residual stress is induced on the subsurface layers of the peened specimen with optimum set of process parameters (PRR=22.5 kHz, ω= 0.04 mm and v= 500 mm/s).

Table 3.4: Information extracted from the XRD test data for an untreated specimen and peened specimen with the optimum process parameters.

	Before LSP (un-peened specimen)						
2θ (Deg)	**β (FWHM) (Deg)**	**β cos θ (rad)**	**4 sin θ**	**Average grain size (nm)**	**d-spacing (nm)**	**Average dislocation (nm^{-2})**	**Average strain (με)**
38.3915	0.1771	0.003276	1.314822	53.647	0.2366251	0.1771	- 426.6
44.6581	0.1653	0.003281	1.519012		0.2056480		
65.04672	0.1669	0.003648	2.149411		0.1433739		
78.20316	0.1741	0.004491	2.521085		0.1224063		
	After LSP (peened specimen with optimum conditions)						
37.90937	0.2282	0.0045910	1.29890487	38.322	0.2427877	0.3541	- 633.9
44.18646	0.2595	0.0050865	1.50360333		0.2052048		
64.64272	0.2321	0.0052192	2.13690904		0.1453710		
77.82179	0.2376	0.0055598	2.51024555		0.1237448		

3.9 Fractography Observations

Good resolution images were taken for the cross section of failed specimens using the optical microscope. Each fractured specimen showed a fracture plane perpendicular to the plane of the surface. Figure 3.17 shows a plane of fracture for an untreated specimen, the cracks initiate on the upper and lower surfaces, grow and propagate along the plane and this can be noticed on the rippled areas on the image. During the period of cyclic loading, cold work occurs at the uncleaved zones resulting in an increase in their brittleness. In addition, the continuous reduction in the rest of the area of the section accompanied with an increase in its brittleness due to strain hardening results in a sudden unpredictable fracture. Looking at the image gives a clear thought there is some symmetry in the process for the upper and lower areas and this can be proved by the direction of cracks propagation and the converging line which splits the upper and lower areas.

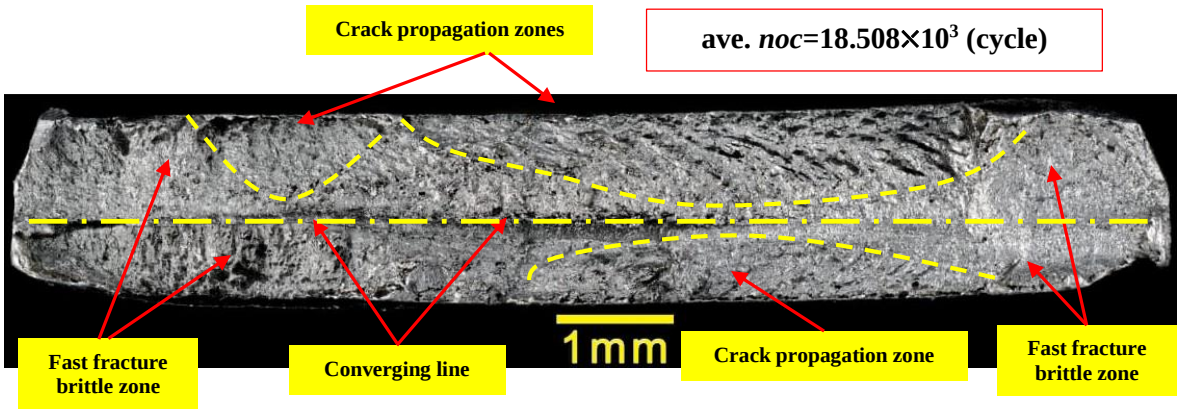

Figure 3.17: Microscopic images for the plane of fracture due fatigue failure for an untreated specimen loaded with a bending stress of 205 MPa.

As mentioned before LSP process was applied on specified areas for both sides, the upper and lower, of each specimen. Figure 3.18 shows the fracture plane for a treated specimen showed a percentage increase in fatigue life of 96.5 %

when processed with the following set of parameters: *PPR* of 25 kHz, ω of 0.03 mm and *v* of 200 mm/s. Although this specimen shows less enhancement in the fatigue life when compared with the optimum specimens it can be classified with the normal results of this study. The degradation in performance is related to the application effects discussed in Section 3.7. As shown in Figure 3.17 less significant is due to multiple fatigue cracks initiation and nucleation at pits roots. Cracks grow through the thickness of the upper and lower surfaces and meet at the middle forming a converging line. The fracture area is characterized by a finer and larger propagation area as well as a significant reduction in the fast fracture brittle zone. when compared with the untread specimen and this explains the larger number of cycles before failure. In addition, surface strengthening due to LSP results in types of cracks called thumbnail cracks as illustrated in the figure.

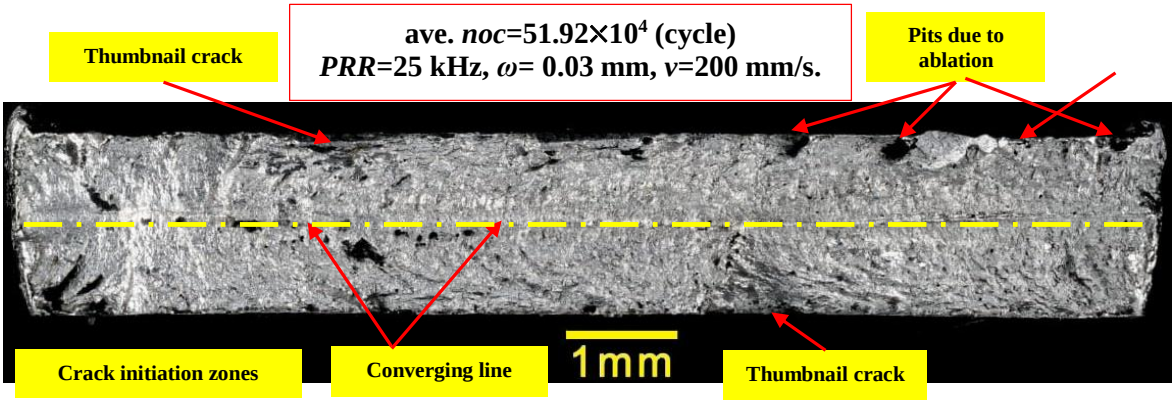

Figure 3.18: Microscopic images for the plane of fracture due fatigue failure for a treated specimen loaded with a bending stress of 205 MPa.

Figure 3.19 shows the fracture plane for an optimum specimen that recorded the greatest percentage increase in fatigue life of 505.25% when processes with *PRR* of 25 kHz, ω of 0.03 mm and *v* of 200 mm/s. It can be well seen the absence of ablative dots and homogeneity in the plane of fracture where most

of it is the cracks propagation rippled feature presents and this explains the longest fatigue period. The zones of rapid brittle fracture are limited where almost concentrated at the edges of the specimens.

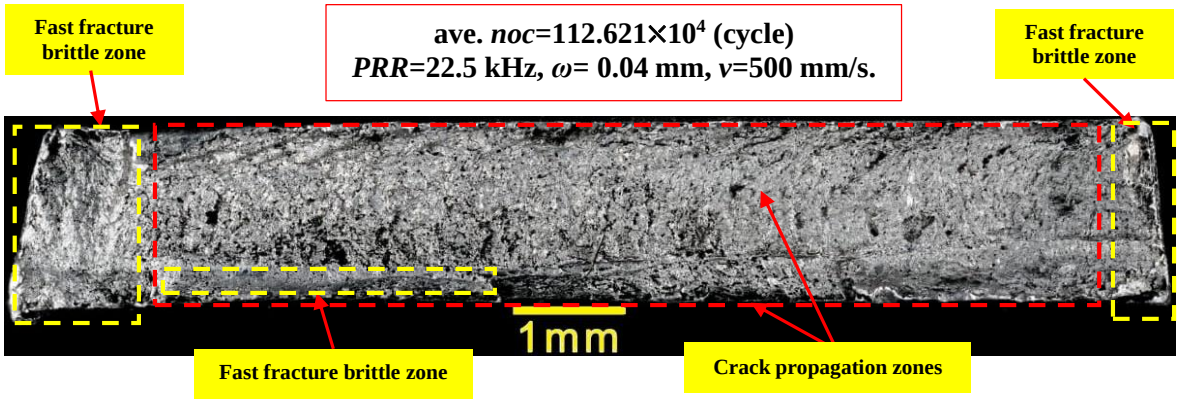

Figure 3.19: Microscopic images for the plane of fracture due fatigue failure for the optimum treated specimen loaded with a bending stress of 205 MPa.

3.10 Conclusions

LSP treatment for Aluminum 6061-T6 thin sheets reveals a significant improvement in fatigue life under cyclic loading. The following concluded remarks are extracted from the current study:

1. Enhancement the fatigue performance with LSP can be highly significant with sets of process parameters yields defects free surfaces after the process. Where two sets of input parameters done this when the *PRR* equals 22.5 kHz, and ω was 0.04 mm, the percentage increase in fatigue life was 505.25% and 477.81% at the minimum, and maximum scanning speeds 200 mm/s and 500 mm/s respectively.

2. XRD analysis test for the optimum specimens indicates the role of LSP in reducing the grain size, increasing in the length of dislocation and introducing effective residual stresses along depth of 700 μm.

3. The scanning speed is the cornerstone in avoiding defects creation at the surface, such as pitting, re-solidified debris and recast layers, which considered the sink for stresses concentrations, cracks initiations and propagation until failure. The conclusion was approved with the SEM images for different specimens.

4. The ideal LSP process is accomplished with cold process and not associated with phase transformation and this was approved from the conducted EDS test.

5. The model revealed that it is possible to make more informed decisions about the preferred settings of the controllable factors in order to achieve the best response

6. The data collected from the current LSP investigation gives technical expertise that has improved the comprehension of process behavior, as well as the ability to anticipate and monitor the process. The data collected from DOE is more trustworthy than that obtained by OFAT.

3.11 Future Works

The following points include some suggestions for future works in the field of LSP:

1. Explore the effect of other parameters in addition to PRR, ω, and v such as the pulse width and hatch (line spacing) on fatigue failure reduction.

2. Study the effect of changing the ablative layer on the quality of LSP output. Also this include using different confinement layers rather than water.

3. Study the effect of scanning pattern of laser spot such as zigzag, spiral and others.

4. Verify experimental result using finite element procedure.

References

References

[1] A. R. Alhamaoy, G. Sh. Sadiq, F. I. Hussein, and S. N. Ali, “The Cyclic Fatigue Behavior for 6061-T6 Al Alloy Shafts Processed by Laser Shock Peening,” Materials Science Forum, vol. 1002. Trans Tech Publications, Ltd., pp. 21–32, Jul. 2020. doi: 10.4028/www.scientific.net/msf.1002.21.

[2] B. Dhakal and S. Swaroop, “Effect of laser shock peening on mechanical and microstructural aspects of 6061-T6 aluminum alloy,” Journal of Materials Processing Technology, vol. 282. Elsevier BV, p. 116640, Aug. 2020. doi: 10.1016/j.jmatprotec.2020.116640.

[3] C. Montross, “Laser shock processing and its effects on microstructure and properties of metal alloys: a review,” International Journal of Fatigue, vol. 24, no. 10. Elsevier BV, pp. 1021–1036, Oct. 2002. doi: 10.1016/s0142-1123(02)00022-1.

[4] J. Z. Zhou et al., “Effect of repeated impacts on mechanical properties and fatigue fracture morphologies of 6061-T6 aluminum subject to laser peening,” Materials Science and Engineering: A, vol. 539. Elsevier BV, pp. 360–368, Mar. 2012. doi: 10.1016/j.msea.2012.01.125.

[5] M. B. Toparli, N. Smyth, and M. E. Fitzpatrick, “Effect of Treatment Area on Residual Stress and Fatigue in Laser Peened Aluminum Sheets,” Metallurgical and Materials Transactions A, vol. 48, no. 4. Springer Science and Business Media LLC, pp. 1519–1523, Jan. 18, 2017. doi: 10.1007/s11661-017-3962-8.

[6] Z. Hong and Y. Chengye, “Laser shock processing of 2024-T62 aluminum alloy,” Materials Science and Engineering: A, vol. 257, no. 2. Elsevier BV, pp. 322–327, Dec. 1998. doi: 10.1016/s0921-5093(98)00793-x.

[7]F. Zhao, W. Z. Bernstein, G. Naik, and G. J. Cheng, “Environmental assessment of laser assisted manufacturing: case studies on laser shock peening and laser assisted turning,” Journal of Cleaner Production, vol. 18, no. 13. Elsevier BV, pp. 1311–1319, Sep. 2010. doi: 10.1016/j.jclepro.2010.04.019.

[8] J. Sheng, S. Huang, J. Z. Zhou, J. Z. Lu, S. Q. Xu, and H. F. Zhang, “Effect of laser peening with different energies on fatigue fracture evolution of 6061-T6 aluminum alloy,” Optics & Laser Technology, vol. 77. Elsevier BV, pp. 169–176, Mar. 2016. doi: 10.1016/j.optlastec.2015.09.008.

[9] S. Gencalp Irizalp, N. Saklakoglu, and B. S. Yilbas, “Characterization of microplastic deformation produced in 6061-T6 by using laser shock

processing," The International Journal of Advanced Manufacturing Technology, vol. 71, no. 1–4. Springer Science and Business Media LLC, pp. 109–115, Nov. 20, 2013. doi: 10.1007/s00170-013-5481-0.

[10] B. S. Yilbas, A. F. M. Arif, C. Karatas, and K. Raza, "Laser treatment of aluminum surface: Analysis of thermal stress field in the irradiated region," Journal of Materials Processing Technology, vol. 209, no. 1. Elsevier BV, pp. 77–88, Jan. 2009. doi: 10.1016/j.jmatprotec.2008.01.047.

[11] X. D. Ren et al., "The effects of residual stress on fatigue behavior and crack propagation from laser shock processing-worked hole," Materials & Design, vol. 44. Elsevier BV, pp. 149–154, Feb. 2013. doi: 10.1016/j.matdes.2012.07.024.

[12] X. D. Ren et al., "Dislocation polymorphism transformation of 6061-T651 aluminum alloy processed by laser shock processing: Effect of tempering at the elevated temperatures," Materials Science and Engineering: A, vol. 578. Elsevier BV, pp. 96–102, Aug. 2013. doi: 10.1016/j.msea.2013.04.034.

[13] P. K. Sharp, Q. Liu, S. A. Barter, P. Baburamani, and G. Clark, "Fatigue life recovery in aluminium alloy aircraft structure," Fatigue & Fracture of Engineering Materials & Structures, vol. 25, no. 2. Wiley, pp. 99–110, Feb. 2002. doi: 10.1046/j.1460-2695.2002.00481.x.

[14] ASM International. "Elements of Metallurgy and Engineering Alloys". In: ASM International.
Ed. by F. Campbell. ASM International, 2008, pp. 252–254.

[15] Z. Wang and W. Wu, "Harmonic dissipative soliton resonance in an Yb doped fiber laser with 110 W all fiber polarization-maintaining amplifier," Optics & Laser Technology, vol. 133. Elsevier BV, p. 106503, Jan. 2021. doi: 10.1016/j.optlastec.2020.106503.

[16] Y. Yang, S. Yang, C. Li, and X. Lin, "Passively Q-switched and mode-locked Tm-Ho co-doped fiber laser using a WS2 saturable absorber fabricated by chemical vapor deposition," Optics & Laser Technology, vol. 111. Elsevier BV, pp. 571–574, Apr. 2019. doi: 10.1016/j.optlastec.2018.10.023.

[17] Business Case - Implementation of Laser Technologies at Scania Ferruform: Welding- and cutting applications for the manufacturing of banjo parts.

[18] Y. Wang et al., "3 kW, 0.2 nm narrow linewidth linearly polarized all-fiber laser based on a compact MOPA structure," Laser Physics Letters, vol. 17, no. 7. IOP Publishing, p. 075101, Jun. 01, 2020. doi: 10.1088/1612-202x/ab8e42.

[19] G. Casalino et al., “Mechanical and microstructure analysis of AA6061 and Ti6Al4V fiber laser butt weld,” Optik, vol. 148. Elsevier BV, pp. 151–156, Nov. 2017. doi: 10.1016/j.ijleo.2017.08.138.

[20] J. Yang et al., “Diode-pumped 10 W femtosecond Yb:CALGO laser with high beam quality,” High Power Laser Science and Engineering, vol. 9. Cambridge University Press (CUP), 2021. doi: 10.1017/hpl.2021.19.

[21] K. Cheng et al., “Ultrafast dynamics of single-pulse femtosecond laser-induced periodic ripples on the surface of a gold film,” Physical Review B, vol. 98, no. 18. American Physical Society (APS), Nov. 28, 2018. doi: 10.1103/physrevb.98.184106.

[22] Chapter 34 LASER MATERIALS PROCESSING Wenwu Zhang, Ph.D. General Electric Global Research Center Schenectady, New York Y. Lawrence Yao, Ph.D. Columbia University New York, New York.

[23] S. Liu, Z. Tian, L. Shen, and M. Qiu, “Numerical Simulation and Experimental Investigation of Laser Ablation of Al2O3 Ceramic Coating,” Materials, vol. 13, no. 23. MDPI AG, p. 5502, Dec. 02, 2020. doi: 10.3390/ma13235502.

[24] Han, J. and Y. Li, Interaction Between Pulsed Laser and Materials. Lasers-Applications in Science and Industry, K. Jakubczak, Ed. InTech, 2011. doi:10.5772/25061 .

[25] D. von der Linde, K. Sokolowski-Tinten, and J. Bialkowski, “Laser–solid interaction in the femtosecond time regime,” Applied Surface Science, vol. 109–110. Elsevier BV, pp. 1–10, Feb. 1997. doi: 10.1016/s0169-4332(96)00611-3.

[26] D. Aruri, K. Adepu, K. Adepu, and K. Bazavada, “Wear and mechanical properties of 6061-T6 aluminum alloy surface hybrid composites [(SiC+Gr) and (SiC+Al2O3)] fabricated by friction stir processing,” Journal of Materials Research and Technology, vol. 2, no. 4. Elsevier BV, pp. 362–369, Oct. 2013. doi: 10.1016/j.jmrt.2013.10.004.

[27] R. R. Ambriz, G. Barrera, R. García, and V. H. López, “The microstructure and mechanical strength of Al-6061-T6 GMA welds obtained with the modified indirect electric arc joint,” Materials & Design, vol. 31, no. 6. Elsevier BV, pp. 2978–2986, Jun. 2010. doi: 10.1016/j.matdes.2009.12.017.

[28] H. Springer, A. Kostka, E. J. Payton, D. Raabe, A. Kaysser-Pyzalla, and G. Eggeler, “On the formation and growth of intermetallic phases during interdiffusion between low-carbon steel and aluminum alloys,” Acta

Materialia, vol. 59, no. 4. Elsevier BV, pp. 1586–1600, Feb. 2011. doi: 10.1016/j.actamat.2010.11.023.

[29] Y. Takahashi et al., "Fatigue limit investigation of 6061-T6 aluminum alloy in giga-cycle regime," Materials Science and Engineering: A, vol. 614. Elsevier BV, pp. 243–249, Sep. 2014. doi: 10.1016/j.msea.2014.07.039.

[30] Introduction to Aluminum Alloys and Tempers, J. Gilbert Kaufman, SBN:0871708035, 9780871708038 . First printing, November 2000

[31] F. C. Campbell, "Ceramic Matrix Composites," Manufacturing Technology for Aerospace Structural Materials. Elsevier, pp. 459–493, 2006. doi: 10.1016/b978-185617495-4/50010-x.

[32] K. P. Soldatos, "On the dynamic dilatation of a compressible Rivlin cube beyond its elastic limit," International Journal of Non-Linear Mechanics, vol. 106. Elsevier BV, pp. 310–323, Nov. 2018. doi: 10.1016/j.ijnonlinmec.2018.04.002.

[33] X. Yu, J. Zhou, H. Liang, Z. Jiang, and L. Wu, "Mechanical metamaterials associated with stiffness, rigidity and compressibility: A brief review," Progress in Materials Science, vol. 94. Elsevier BV, pp. 114–173, May 2018. doi: 10.1016/j.pmatsci.2017.12.003.

[34] Method of Determination of Technological Durabilityof Plastically Deformed Sheet Parts of Vehicles Volodymyr Dragobetskii1 *, Mykhaylo Zagirnyak1 , Olena Naumova1 , Sergii Shlyk1 , Aleksandr Shapoval2018.

[35] Mechanical Properties of Materials: Definition, Testing and Application S. Senthil Murugan Department of Mechanical Engineering, Mepco Schlenk Engineering College (Autonomous), Sivakasi, India 2020.

[36]V. Gallicchio, V. Lodato, R. De Santis, and S. Rengo, "Fracture Strength and Failure Modes of Endodontically Treated Premolars Restored with Compact and Hollow Composite Posts Subjected to Cyclic Fatigue," Materials, vol. 15, no. 3. MDPI AG, p. 1141, Feb. 01, 2022. doi: 10.3390/ma15031141.

[37] A. Bhattacharya et al., "Irradiation hardening and ductility loss of Eurofer97 steel variants after neutron irradiation to ITER-TBM relevant conditions," Fusion Engineering and Design, vol. 173. Elsevier BV, p. 112935, Dec. 2021. doi: 10.1016/j.fusengdes.2021.112935.

[38] https://www.dpgpolytechnic.com/downloads/files/n5d68b2c8a6e32.pdf.

[39] Farah Behnam "Influence of hot dip galvanizing on fatigue behavior of welded steel joints " Espoo, 25th November 2019.

[40] Alexander BECKER The effect of laser shock peening and shot peening on the fatigue performance of aluminium alloy 7075 2017.

[41] J. Grum, “Book Review: Laser Shock Peening, Performance and Process Simulation by K. Ding and L. Ye,” International Journal of Microstructure and Materials Properties, vol. 3, no. 1. Inderscience Publishers, p. 179, 2008. doi: 10.1504/ijmmp.2008.018396.

[42] N. E. Dowling, “Mean Stress Effects in Stress-Life and Strain-Life Fatigue,” SAE Technical Paper Series. SAE International, Apr. 01, 2004. doi: 10.4271/2004-01-2227.

[43] I. Čular, K. Vučković, D. Žeželj, and S. Glodež, “Analytical approach for low and high cycle bending fatigue life prediction of carburized gear steel specimens,” Engineering Failure Analysis, vol. 108. Elsevier BV, p. 104328, Jan. 2020. doi: 10.1016/j.engfailanal.2019.104328.

[44] E. Ghafoori and M. Motavalli, “A Retrofit Theory to Prevent Fatigue Crack Initiation in Aging Riveted Bridges Using Carbon Fiber-Reinforced Polymer Materials,” Polymers, vol. 8, no. 8. MDPI AG, p. 308, Aug. 18, 2016. doi: 10.3390/polym8080308.

[45] N. Leuning, S. Steentjes, H. A. Weiss, W. Volk, and K. Hameyer, “Magnetic Material Deterioration of Non-Oriented Electrical Steels as a Result of Plastic Deformation Considering Residual Stress Distribution,” IEEE Transactions on Magnetics, vol. 54, no. 11. Institute of Electrical and Electronics Engineers (IEEE), pp. 1–5, Nov. 2018. doi: 10.1109/tmag.2018.2848365.

[46] C. LI, D. FAN, X. YU, and J. HUANG, “Residual stress and welding distortion of Al/steel butt joint by arc-assisted laser welding-brazing,” Transactions of Nonferrous Metals Society of China, vol. 29, no. 4. Elsevier BV, pp. 692–700, Apr. 2019. doi: 10.1016/s1003-6326(19)64979-4.

[47] M.-N. Avettand-Fènoël, T. Sapanathan, T. Pirling, G. Racineux, A. Simar, and J.-M. Drezet, “Investigation of residual stresses in planar dissimilar magnetic pulse welds by neutron diffraction,” Journal of Manufacturing Processes, vol. 68. Elsevier BV, pp. 1758–1766, Aug. 2021. doi: 10.1016/j.jmapro.2021.06.071.

[48] X. Shen et al., “Residual stresses induced by laser shock peening in orthopaedic Ti-6Al-7Nb alloy,” Optics & Laser Technology, vol. 131. Elsevier BV, p. 106446, Nov. 2020. doi: 10.1016/j.optlastec.2020.106446.

[49] T. T. P. Nguyen, R. Tanabe, and Y. Ito, “Comparative study of the expansion dynamics of laser-driven plasma and shock wave in in-air and underwater ablation regimes,” Optics & Laser Technology, vol. 100. Elsevier BV, pp. 21–26, Mar. 2018. doi: 10.1016/j.optlastec.2017.09.021.

[50] A.H. Clauer. “Laser Shock Peening for Fatigue Resistance”. In: Surface Performance of Titanium. Ed. by J.K. Gregory, H.J. rack, and D. Eylon. Warrendale: TMS, 1996, pp. 271–230.

[51] G. Singh. “Effective Simulation and Optimization of a Laser Peening Process”. Thesis. Dayton: Wright State University, 2006. URL: http://cecs.wright.edu/cepro/docs/thesis/Effective_Simulation_and_Optimization_of_a_Laser_Peening_ Process_SINGH.pdf.

[52] M. J. Shepard, P. R. Smith, and M. S. Amer, “Introduction of Compressive Residual Stresses in Ti-6Al-4V Simulated Airfoils via Laser Shock Processing,” Journal of Materials Engineering and Performance, vol. 10, no. 6. Springer Science and Business Media LLC, pp. 670–678, Dec. 01, 2001. doi: 10.1361/105994901770344539.

[53] L.-C. Zhang, L.-Y. Chen, and L. Wang, “Surface Modification of Titanium and Titanium Alloys: Technologies, Developments, and Future Interests,” Advanced Engineering Materials, vol. 22, no. 5. Wiley, p. 1901258, Jan. 09, 2020. doi: 10.1002/adem.201901258.

[54] V. Nelea et al., “Pulsed laser deposition of hydroxyapatite thin films on Ti-5Al-2.5Fe substrates with and without buffer layers,” Applied Surface Science, vol. 168, no. 1–4. Elsevier BV, pp. 127–131, Dec. 2000. doi: 10.1016/s0169-4332(00)00616-4.

[55] G. C.-Guillemette, “A Review of the Use of Lasers in Transformation Hardening.” Unpublished, 2016. doi: 10.13140/RG.2.1.3114.6642.

[56] R. Karimbaev, Y.-S. Pyun, E. Maleki, O. Unal, and A. Amanov, “An improvement in fatigue behavior of AISI 4340 steel by shot peening and ultrasonic nanocrystal surface modification,” Materials Science and Engineering: A, vol. 791. Elsevier BV, p. 139752, Jul. 2020. doi: 10.1016/j.msea.2020.139752.

[57] C. Wang et al., “Changes in surface integrity of cemented tungsten carbide with shot peening treatment,” Surface and Coatings Technology, vol. 425. Elsevier BV, p. 127710, Nov. 2021. doi: 10.1016/j.surfcoat.2021.127710.

[58] E. Maleki and O. Unal, “Optimization of Shot Peening Effective Parameters on Surface Hardness Improvement,” Metals and Materials

International, vol. 27, no. 9. Springer Science and Business Media LLC, pp. 3173–3185, Jun. 09, 2020. doi: 10.1007/s12540-020-00758-x.

[59] Y. Hua, Z. Liu, B. Wang, and X. Hou, "Surface modification through combination of finish turning with low plasticity burnishing and its effect on fatigue performance for Inconel 718," Surface and Coatings Technology, vol. 375. Elsevier BV, pp. 508–517, Oct. 2019. doi: 10.1016/j.surfcoat.2019.07.057.

[60] LPB as a Crack Initiation Resistant Process for Case Hardened Steels N. Jayaraman, Doug Christensen, Jeremy Scheel Lambda Research 5521 Fair Lane Cincinnati, Ohio 45227-3401

[61] J. A. Travieso-Rodríguez, R. Jerez-Mesa, G. Gómez-Gras, J. Llumà-Fuentes, O. Casadesús-Farràs, and M. Madueño-Guerrero, "Hardening effect and fatigue behavior enhancement through ball burnishing on AISI 1038," Journal of Materials Research and Technology, vol. 8, no. 6. Elsevier BV, pp. 5639–5646, Nov. 2019. doi: 10.1016/j.jmrt.2019.09.032.

[62] FOD RESISTANCE AND FATIGUE CRACK ARREST IN LOW PLASTICITY BURNISHED IN718 . Paul S. Prevéy Lambda Research, Cincinnati, OH Jack Telesman, Timothy Gabb and Peter Kantzos NASA Glenn Research Center, Cleveland, OH.

[63] J. Lago et al., "Fatigue Life Improvement of the High Strength Steel Welded Joints by Ultrasonic Impact Peening," Metals, vol. 9, no. 6. MDPI AG, p. 619, May 28, 2019. doi: 10.3390/met9060619.

[64] Methods to create compressive stress in high strength steel components Amir Abdin, Kaveh Feyzabi, Oskar Hellman, Henrietta Nordström, Dilman Rasa, Gustav Thaung Tolförs, Per-Olof Öqvist.

[65] X. Zhao et al., "Manufacturing of high-precision surface micro-structures on stainless steel by ultrasonic impact peening," The International Journal of Advanced Manufacturing Technology, vol. 116, no. 3–4. Springer Science and Business Media LLC, pp. 915–930, Jun. 25, 2021. doi: 10.1007/s00170-021-07528-y.

[66] H. Soyama, "Comparison between the improvements made to the fatigue strength of stainless steel by cavitation peening, water jet peening, shot peening and laser peening," Journal of Materials Processing Technology, vol. 269. Elsevier BV, pp. 65–78, Jul. 2019. doi: 10.1016/j.jmatprotec.2019.01.030.

[67] https://suginocorp.com/cwjp/

[68] G. Lu, J. Li, Y. Zhang, and D. W. Sokol, “A metal marking method based on laser shock processing,” Materials and Manufacturing Processes, vol. 34, no. 6. Informa UK Limited, pp. 598–603, Jan. 21, 2019. doi: 10.1080/10426914.2019.1566618.

[69] L. Lan, X. Jin, S. Gao, B. He, and Y. Rong, “Microstructural evolution and stress state related to mechanical properties of electron beam melted Ti-6Al-4V alloy modified by laser shock peening,” Journal of Materials Science & Technology, vol. 50. Elsevier BV, pp. 153–161, Aug. 2020. doi: 10.1016/j.jmst.2019.11.039.

[70] L. Tan, C. Yao, D. Zhang, J. Ren, X. Shen, and Z. Zhou, “Effects of different mechanical surface treatments on surface integrity of TC17 alloys,” Surface and Coatings Technology, vol. 398. Elsevier BV, p. 126073, Sep. 2020. doi: 10.1016/j.surfcoat.2020.126073.

[71] U. Trdan, M. Skarba, J. A. Porro, J. L. Ocaña, and J. Grum, “Application of massive laser shock processing for improvement of mechanical and tribological properties,” Surface and Coatings Technology, vol. 342. Elsevier BV, pp. 1–11, May 2018. doi: 10.1016/j.surfcoat.2018.02.084.

[72] L. Spadaro, S. Hereñú, R. Strubbia, G. Gómez Rosas, R. Bolmaro, and C. Rubio González, “Effects of laser shock processing and shot peening on 253 MA austenitic stainless steel and their consequences on fatigue properties,” Optics & Laser Technology, vol. 122. Elsevier BV, p. 105892, Feb. 2020. doi: 10.1016/j.optlastec.2019.105892.

[73] D. C. van Aswegen and C. Polese, “Experimental and analytical investigation of the effects of laser shock peening processing strategy on fatigue crack growth in thin 2024 aluminium alloy panels,” International Journal of Fatigue, vol. 142. Elsevier BV, p. 105969, Jan. 2021. doi: 10.1016/j.ijfatigue.2020.105969.

[74] S. R et al., “Laser Shock Peening and its Applications: A Review,” Lasers in Manufacturing and Materials Processing, vol. 6, no. 4. Springer Science and Business Media LLC, pp. 424–463, Oct. 23, 2019. doi: 10.1007/s40516-019-00098-8.

[75] S. Bovid, A. Clauer, M. Kattoura, A. Vivek, G. Daehn, and S. Niezgoda, “Measurement and characterization of nanosecond laser driven shockwaves utilizing photon Doppler velocimetry,” Journal of Applied Physics, vol. 129, no. 20. AIP Publishing, p. 205101, May 28, 2021. doi: 10.1063/5.0048610.

[76] S. Adu-Gyamfi, “Effects of Laser Shock Peening on Mechanical Properties and Surface Morphology of AA2024 Alloy,” American Journal of Mechanical and Materials Engineering, vol. 2, no. 2. Science Publishing Group, p. 15, 2018. doi: 10.11648/j.ajmme.20180202.11.

[77] S. Bovid, A. Clauer, M. Kattoura, A. Vivek, G. Daehn, and S. Niezgoda, “Measurement and characterization of nanosecond laser driven shockwaves utilizing photon Doppler velocimetry,” Journal of Applied Physics, vol. 129, no. 20. AIP Publishing, p. 205101, May 28, 2021. doi: 10.1063/5.0048610.

[78] B. Su, H. Wang, Y. Cao, X. Pei, and G. Hua, “Local deformation and macro distortion of TC4 titanium alloy during laser shock processing,” The International Journal of Advanced Manufacturing Technology, vol. 106, no. 11–12. Springer Science and Business Media LLC, pp. 5421–5428, Feb. 2020. doi: 10.1007/s00170-020-05058-7.

[79] K. S. Joshi, G. Rajyalakshmi, G. Ranjith, S. Kalainathan, and S. Prabhakaran, “Optimization of Laser Shock Peening For Titanium,” Materials Today: Proceedings, vol. 5, no. 5. Elsevier BV, pp. 12174–12186, 2018. doi: 10.1016/j.matpr.2018.02.195.

[80] K. Gurusami, D. Chandramohan, S. Dinesh Kumar, M. Dhanashekar, and T. Sathish, “Strengthening mechanism of Nd: Yag laser shock peening for commercially pure titanium (CP-TI) on surface integrity and residual stresses,” Materials Today: Proceedings, vol. 21. Elsevier BV, pp. 981–987, 2020. doi: 10.1016/j.matpr.2019.09.141.

[81] Y. Jing, X. Fang, N. Xi, X. Feng, and K. Huang, “Investigation of microstructure and mechanical properties evolution in 7050 aluminum alloy and 316L stainless steel treated by laser shock peening,” Materials Characterization, vol. 182. Elsevier BV, p. 111571, Dec. 2021. doi: 10.1016/j.matchar.2021.111571.

[82] N. Maharjan, S. Y. Chan, T. Ramesh, P. G. Nai, and D. T. Ardi, “Fatigue performance of laser shock peened Ti6Al4V and Al6061- T6 alloys,” Fatigue & Fracture of Engineering Materials & Structures, vol. 44, no. 3. Wiley, pp. 733–747, Nov. 30, 2020. doi: 10.1111/ffe.13390.

[83] A. S. Gill, A. Telang, C. Ye, S. R. Mannava, D. Qian, and V. K. Vasudevan, “Localized plastic deformation and hardening in laser shock peened Inconel alloy 718SPF,” Materials Characterization, vol. 142. Elsevier BV, pp. 15–26, Aug. 2018. doi: 10.1016/j.matchar.2018.05.010.

[84] D. Karthik, K. U. Yazar, A. Bisht, S. Swaroop, C. Srivastava, and S. Suwas, “Gradient plastic strain accommodation and nanotwinning in multi-pass laser shock peened 321 steel,” Applied Surface Science, vol. 487. Elsevier BV, pp. 426–432, Sep. 2019. doi: 10.1016/j.apsusc.2019.05.130.

[85] M. Munther, T. Martin, A. Tajyar, L. Hackel, A. Beheshti, and K. Davami, “Laser shock peening and its effects on microstructure and properties of additively manufactured metal alloys: a review,” Engineering Research Express, vol. 2, no. 2. IOP Publishing, p. 022001, Jun. 01, 2020. doi: 10.1088/2631-8695/ab9b16.

[86] Y. Jing, X. Fang, N. Xi, X. Feng, and K. Huang, “Investigation of microstructure and mechanical properties evolution in 7050 aluminum alloy and 316L stainless steel treated by laser shock peening,” Materials Characterization, vol. 182. Elsevier BV, p. 111571, Dec. 2021. doi: 10.1016/j.matchar.2021.111571.

[87] A. Chattopadhyay, G. Muvvala, S. Sarkar, V. Racherla, and A. K. Nath, “Effect of laser shock peening on microstructural, mechanical and corrosion properties of laser beam welded commercially pure titanium,” Optics & Laser Technology, vol. 133. Elsevier BV, p. 106527, Jan. 2021. doi: 10.1016/j.optlastec.2020.106527.

[88] M. John, P. R. Kalvala, M. Misra, and P. L. Menezes, “Peening Techniques for Surface Modification: Processes, Properties, and Applications,” Materials, vol. 14, no. 14. MDPI AG, p. 3841, Jul. 09, 2021. doi: 10.3390/ma14143841.

[89] B. Starman, H. Hallberg, M. Wallin, M. Ristinmaa, and M. Halilovič, “Differences in phase transformation in laser peened and shot peened 304 austenitic steel,” International Journal of Mechanical Sciences, vol. 176. Elsevier BV, p. 105535, Jun. 2020. doi: 10.1016/j.ijmecsci.2020.105535.

[90] Montross CS, Wei T, Ye L, Clark G, Mai Y-W. Laser shock processing and its effects on microstructure and properties of metal alloys: a review. Int J Fatigue 2002;24:1021– 36. doi: 10.1016/S0142-1123(02)00022-1.

[91] A. H. Clauer, “Laser Shock Peening, the Path to Production,” Metals, vol. 9, no. 6. MDPI AG, p. 626, May 29, 2019. doi: 10.3390/met9060626.

[92] M. J. Yadav, A. N. Jinoop, C. Danduk, and S. K. Subbu, “Laser Shock Processing: Process Physics, Parameters, and Applications,” Materials Today: Proceedings, vol. 4, no. 8. Elsevier BV, pp. 7921–7930, 2017. doi: 10.1016/j.matpr.2017.07.128.

[93] SAI, Rhoda Ayorkor. The Improvement of the Cavitation Resistance of Technical Surfaces Using High Power Laser Pulses [online]. 2021-02-04T18:39:42Z [cit. 2022-02-22]. Dostupné z: https://dspace.tul.cz/handle/15240/159720. Diplomová práce..

[94] C. Wang, L. Wang, C.-L. Wang, K. Li, and X.-G. Wang, "Dislocation density-based study of grain refinement induced by laser shock peening," Optics & Laser Technology, vol. 121. Elsevier BV, p. 105827, Jan. 2020. doi: 10.1016/j.optlastec.2019.105827.

[95] J. Wu, X. Liu, J. Zhao, H. Qiao, Y. Zhang, and H. Zhang, "The online monitoring method research of laser shock processing based on plasma acoustic wave signal energy," Optik, vol. 183. Elsevier BV, pp. 1151–1159, Apr. 2019. doi: 10.1016/j.ijleo.2019.01.092.

[96] O. O. Versolato, "Physics of laser-driven tin plasma sources of EUV radiation for nanolithography," Plasma Sources Science and Technology, vol. 28, no. 8. IOP Publishing, p. 083001, Aug. 01, 2019. doi: 10.1088/1361-6595/ab3302.

[97] L. Zhou et al., "Deforming TC6 titanium alloys at ultrahigh strain rates during multiple laser shock peening," Materials Science and Engineering: A, vol. 578. Elsevier BV, pp. 181–186, Aug. 2013. doi: 10.1016/j.msea.2013.04.070.

[98] R. K. Nalla, I. Altenberger, U. Noster, G. Y. Liu, B. Scholtes, and R. O. Ritchie, "On the influence of mechanical surface treatments—deep rolling and laser shock peening—on the fatigue behavior of Ti–6Al–4V at ambient and elevated temperatures," Materials Science and Engineering: A, vol. 355, no. 1–2. Elsevier BV, pp. 216–230, Aug. 2003. doi: 10.1016/s0921-5093(03)00069-8.

[99] C. Montross, "Laser shock processing and its effects on microstructure and properties of metal alloys: a review," International Journal of Fatigue, vol. 24, no. 10. Elsevier BV, pp. 1021–1036, Oct. 2002. doi: 10.1016/s0142-1123(02)00022-1.

[100] Y. Zhao, Y.-L. Zhao, and L.-K. Wang, "Application of femtosecond laser micromachining in silicon carbide deep etching for fabricating sensitive diaphragm of high temperature pressure sensor," Sensors and Actuators A: Physical, vol. 309. Elsevier BV, p. 112017, Jul. 2020. doi: 10.1016/j.sna.2020.112017.

[101] Q. Wu, L. Weng, Y. Zhao, B. Guo, and T. Luo, “On the tensile mechanical characteristics of fine-grained granite after heating/cooling treatments with different cooling rates,” Engineering Geology, vol. 253. Elsevier BV, pp. 94–110, Apr. 2019. doi: 10.1016/j.enggeo.2019.03.014.

[102] S. Adu-Gyamfi, X. D. Ren, E. A. Larson, Y. Ren, and Z. Tong, “The effects of laser shock peening scanning patterns on residual stress distribution and fatigue life of AA2024 aluminium alloy,” Optics & Laser Technology, vol. 108. Elsevier BV, pp. 177–185, Dec. 2018. doi: 10.1016/j.optlastec.2018.06.036.

[103] Y. Geng et al., “Effect of Laser Shock Peening on Residual Stress, Microstructure and Hot Corrosion Behavior of Damage-Tolerant TC21 Titanium Alloy,” Journal of Materials Engineering and Performance, vol. 27, no. 9. Springer Science and Business Media LLC, pp. 4703–4713, Aug. 13, 2018. doi: 10.1007/s11665-018-3575-4.

[104] Y. Fang, “Strengthening characteristics in TC17 titanium alloy treated during LSP,” Optik, vol. 226. Elsevier BV, p. 165895, Jan. 2021. doi: 10.1016/j.ijleo.2020.165895.

[105] Pulsed Lasers Introduction to Power and Energy Calculations

[106] M. El-Khoury, B. Voisiat, T. Kunze, and A. F. Lasagni, “Utilizing a Diffractive Focus Beam Shaper to Enhance Pattern Uniformity and Process Throughput during Direct Laser Interference Patterning,” Materials, vol. 15, no. 2. MDPI AG, p. 591, Jan. 13, 2022. doi: 10.3390/ma15020591.

[107] Z. Hong and Y. Chengye, “Laser shock processing of 2024-T62 aluminum alloy,” Materials Science and Engineering: A, vol. 257, no. 2. Elsevier BV, pp. 322–327, Dec. 1998. doi: 10.1016/s0921-5093(98)00793-x.

[108] G. Schnell, U. Duenow, and H. Seitz, “Effect of Laser Pulse Overlap and Scanning Line Overlap on Femtosecond Laser-Structured Ti6Al4V Surfaces,” Materials, vol. 13, no. 4. MDPI AG, p. 969, Feb. 21, 2020. doi: 10.3390/ma13040969.

[109] V. Martín, J. Vázquez, C. Navarro, and J. Domínguez, “Effect of shot peening residual stresses and surface roughness on fretting fatigue strength of Al 7075-T651,” Tribology International, vol. 142. Elsevier BV, p. 106004, Feb. 2020. doi: 10.1016/j.triboint.2019.106004.

[110] P. P. Shukla, P. T. Swanson, and C. J. Page, “Laser shock peening and mechanical shot peening processes applicable for the surface treatment of technical grade ceramics: A review,” Proceedings of the Institution of

Mechanical Engineers, Part B: Journal of Engineering Manufacture, vol. 228, no. 5. SAGE Publications, pp. 639–652, Dec. 05, 2013. doi: 10.1177/0954405413507250.

[111] K. Dalaei, B. Karlsson, and L.-E. Svensson, "Stability of residual stresses created by shot peening of pearlitic steel and their influence on fatigue behaviour," Procedia Engineering, vol. 2, no. 1. Elsevier BV, pp. 613–622, Apr. 2010. doi: 10.1016/j.proeng.2010.03.066.

[112] Nasma, A., Aishath, N., *Azilah, A. and Sulaiman, A.Z. Optimization of vitexin and isovitexin compounds extracted from dried Mas Cotek leaves using one-factor-at-a-time (OFAT) approach in aqueous extraction (December 2018) .

[113] 1Z. Wahid and 2N. Nadir Improvement of One Factor at a Time through Design of Experiments 2013.

[114] X. Lai, S. Wang, S. Ma, J. Xie, and Y. Zheng, "Parameter sensitivity analysis and simplification of equivalent circuit model for the state of charge of lithium-ion batteries," Electrochimica Acta, vol. 330. Elsevier BV, p. 135239, Jan. 2020. doi: 10.1016/j.electacta.2019.135239.

[115] P. M. Murray, F. Bellany, L. Benhamou, D.-K. Bučar, A. B. Tabor, and T. D. Sheppard, "The application of design of experiments (DoE) reaction optimisation and solvent selection in the development of new synthetic chemistry," Organic & Biomolecular Chemistry, vol. 14, no. 8. Royal Society of Chemistry (RSC), pp. 2373–2384, 2016. doi: 10.1039/c5ob01892g.

[116] R. Leardi, "Experimental design in chemistry: A tutorial," Analytica Chimica Acta, vol. 652, no. 1–2. Elsevier BV, pp. 161–172, Oct. 2009. doi: 10.1016/j.aca.2009.06.015.

[117] D. W. Lendrem et al., "Lost in space: design of experiments and scientific exploration in a Hogarth Universe," Drug Discovery Today, vol. 20, no. 11. Elsevier BV, pp. 1365–1371, Nov. 2015. doi: 10.1016/j.drudis.2015.09.015.

[118] B. Dejaegher and Y. Vander Heyden, "Experimental designs and their recent advances in set-up, data interpretation, and analytical applications," Journal of Pharmaceutical and Biomedical Analysis, vol. 56, no. 2. Elsevier BV, pp. 141–158, Sep. 2011. doi: 10.1016/j.jpba.2011.04.023.

[119] Afsaneh Morshedi and Mina Akbarian application of response surface methodology: design of experiments and optimization: A mini review www.cibtech.org/sp.ed/jls/2014/04/jls.htm

[120] Montgomery Douglas C (2005). Design and Analysis of Experiments Response Surface Method and Designs (New Jersey, John Wiley and Sons, Inc).

[121] Oehlert GW (2000). Design and Analysis of Experiments: Response Surface Design (New York: W.H. Freeman and Company).

[122] K. TARAMAN, “Multi machining output—multi independent variable turning research by response surface methodology,” International Journal of Production Research, vol. 12, no. 2. Informa UK Limited, pp. 233–245, Jan. 1974. doi: 10.1080/00207547408919552.

[123] M Manohar1 Jomy Joseph2 T Selvaraj3 D Sivakumar1 Application of Box Behnken design to optimize the parameters for turning Inconel 718 using coated carbide tools Issue 4, April-2013.

[124] R. Straetemans et al., “Design and Analysis of Drug Combination Experiments,” Biometrical Journal, vol. 47, no. 3. Wiley, pp. 299–308, Jun. 2005. doi: 10.1002/bimj.200410124.

[125] X. Nie, W. He, L. Zhou, Q. Li, and X. Wang, “Experiment investigation of laser shock peening on TC6 titanium alloy to improve high cycle fatigue performance,” Materials Science and Engineering: A, vol. 594. Elsevier BV, pp. 161–167, Jan. 2014. doi: 10.1016/j.msea.2013.11.073.

[126] X. D. Ren, J. J. Huang, W. F. Zhou, S. D. Xu, and F. F. Liu, “Surface nano-crystallization of AZ91D magnesium alloy induced by laser shock processing,” Materials & Design, vol. 86. Elsevier BV, pp. 421–426, Dec. 2015. doi: 10.1016/j.matdes.2015.07.039.

[127] [1]J. Z. Lu et al., “Microstructural response and grain refinement mechanism of commercially pure titanium subjected to multiple laser shock peening impacts,” Acta Materialia, vol. 127. Elsevier BV, pp. 252–266, Apr. 2017. doi: 10.1016/j.actamat.2017.01.050.

[128] Marco Pavan Laser Shock Peening for Fatigue Life enhancement of Aerospace Components 2017.

[129] J. T. Wang et al., “Effect of laser shock peening on the high-temperature fatigue performance of 7075 aluminum alloy,” Materials Science and Engineering: A, vol. 704. Elsevier BV, pp. 459–468, Sep. 2017. doi: 10.1016/j.msea.2017.08.050.

[130] H. Wang, C. Ning, Y. Huang, Z. Cao, X. Chen, and W. Zhang, “Improvement of abrasion resistance in artificial seawater and corrosion resistance in NaCl solution of 7075 aluminum alloy processed by laser shock peening,” Optics and Lasers in Engineering, vol. 90. Elsevier BV, pp. 179–185, Mar. 2017. doi: 10.1016/j.optlaseng.2016.10.016.

[131] Boopa Nandhini Aravamudhan Study of the effects of laser shock peening on corrosion behavior of aluminum alloy 7075. 2018.

[132] P. Liu, S. Sun, S. Xu, Y. Li, and G. Ren, “Microstructure and properties in the weld surface of friction stir welded 7050-T7451 aluminium alloys by laser shock peening,” Vacuum, vol. 152. Elsevier BV, pp. 25–29, Jun. 2018. doi: 10.1016/j.vacuum.2018.03.002.

[133] J. T. Wang et al., “Improving creep properties of 7075 aluminum alloy by laser shock peening,” Surface and Coatings Technology, vol. 349. Elsevier BV, pp. 725–735, Sep. 2018. doi: 10.1016/j.surfcoat.2018.06.061.

[134] L. Chen et al., “Evolution of microstructure and grain refinement mechanism of pure nickel induced by laser shock peening,” Materials Science and Engineering: A, vol. 728. Elsevier BV, pp. 20–29, Jun. 2018. doi: 10.1016/j.msea.2018.04.105.

[135] Gaurav Vilas Inamke the investigation of warm laser shock peening as a post processing technique to improve joint strength of laser welded materials. 2019.

[136] J. Park, I. Yeo, I. Jang, and S. Jeong, “Improvement of friction characteristics of cast aluminum-silicon alloy by laser shock peening,” Journal of Materials Processing Technology, vol. 266. Elsevier BV, pp. 283–291, Apr. 2019. doi: 10.1016/j.jmatprotec.2018.11.007.

[137] B. Dhakal and S. Swaroop, “Effect of laser shock peening on mechanical and microstructural aspects of 6061-T6 aluminum alloy,” Journal of Materials Processing Technology, vol. 282. Elsevier BV, p. 116640, Aug. 2020. doi: 10.1016/j.jmatprotec.2020.116640.

[138] X. Meng, H. Wang, W. Tan, J. Cai, J. Zhou, and L. Liu, “Gradient microstructure and vibration fatigue properties of 2024-T351 aluminium alloy treated by laser shock peening,” Surface and Coatings Technology, vol. 391. Elsevier BV, p. 125698, Jun. 2020. doi: 10.1016/j.surfcoat.2020.125698.

[139] A. R. Alhamaoy, G. Sh. Sadiq, F. I. Hussein, and S. N. Ali, “The Cyclic Fatigue Behavior for 6061-T6 Al Alloy Shafts Processed by Laser Shock Peening,” Materials Science Forum, vol. 1002. Trans Tech Publications, Ltd., pp. 21–32, Jul. 2020. doi: 10.4028/www.scientific.net/msf.1002.21.

[140] American Society for Testing and Materials (ASTM), “Standard test method for tensile properties /D638,” Annual Book of ASTM Standard, 2003.

[141] Standard Test Methods for Tension Testing of Metallic Materials ASTM-E8

[142] P. K. Mandal, M. Sam Mathews, B. A. Daniel, and J. Devasia, “Effect of ageing treatment on microstructure and mechanical properties of α+β type titanium alloy used for biomaterials,” IOP Conference Series: Materials Science and Engineering, vol. 561, no. 1. IOP Publishing, p. 012060, Oct. 01, 2019. doi: 10.1088/1757-899x/561/1/012060.

[143] P. K. Park, D. H. Cho, E. Y. Kim, and K. H. Chu, “Optimization of carotenoid production by Rhodotorula glutinis using statistical experimental design,” World Journal of Microbiology and Biotechnology, vol. 21, no. 4. Springer Science and Business Media LLC, pp. 429–434, Jun. 2005. doi: 10.1007/s11274-004-1891-3.

[144] L. M. Collins, J. J. Dziak, and R. Li, “Design of experiments with multiple independent variables: A resource management perspective on complete and reduced factorial designs.,” Psychological Methods, vol. 14, no. 3. American Psychological Association (APA), pp. 202–224, 2009. doi: 10.1037/a0015826

[145] S. L. C. Ferreira et al., “Box-Behnken design: An alternative for the optimization of analytical methods,” Analytica Chimica Acta, vol. 597, no. 2. Elsevier BV, pp. 179–186, Aug. 2007. doi: 10.1016/j.aca.2007.07.011 .

[146] S. Sathyajith and S. Kalainathan, “Effect of laser shot peening on precipitation hardened aluminum alloy 6061-T6 using low energy laser,” Optics and Lasers in Engineering, vol. 50, no. 3. Elsevier BV, pp. 345–348, Mar. 2012. doi: 10.1016/j.optlaseng.2011.11.002.

[147] A. Salimianrizi, E. Foroozmehr, M. Badrossamay, and H. Farrokhpour, “Effect of Laser Shock Peening on surface properties and residual stress of Al6061-T6,” Optics and Lasers in Engineering, vol. 77. Elsevier BV, pp. 112–117, Feb. 2016. doi: 10.1016/j.optlaseng.2015.08.001.

[148] M. J. Yadav, A. N. Jinoop, C. Danduk, and S. K. Subbu, “Laser Shock Processing: Process Physics, Parameters, and Applications,” Materials Today: Proceedings, vol. 4, no. 8, pp. 7921–7930, 2017, doi: 10.1016/j.matpr.2017.07.128

[149] A. Vaziri, H. R. Shahverdi, S. G. Shabestari, and M. J. Torkamany, “Effect of beam interaction time on laser alloying with pulsed Nd–YAG laser,” Materials Science and Technology, vol. 25, no. 10, pp. 1234–1237, Oct. 2009, doi: 10.1179/174328408x372065

[150] C. Montross, “Laser shock processing and its effects on microstructure and properties of metal alloys: a review,” International Journal of Fatigue, vol. 24, no. 10. Elsevier BV, pp. 1021–1036, Oct. 2002. doi: 10.1016/s0142-1123(02)00022-1.

Appendices

Appendix (A)

PROCEDURE

The Fatigue test was carried out for the specimens using the alternating bending fatigue machine type HI-TECH HSM20\ England. The applied load in fatigue testing was utilized according to the requirements of the employed fatigue test machine in terms of determining the specimen dimensions for aluminum material and selecting the range of deflection values at the free end of the specimen. The applied bending loads and stresses are extracted from their equation as follows:

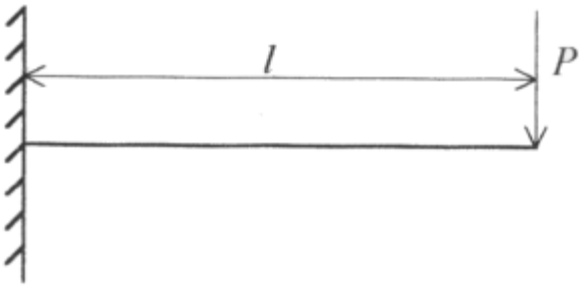

Max. bending moment = Pl

$$\text{Max. bending stress } \sigma = \frac{Pl}{Z} = \frac{6Pl}{bt^2}$$

Where the strip cantilever is b wide and t thick

$$\text{Free end deflection } \delta = \frac{Pl^3}{3EI} = \frac{4Pl^3}{Ebt^3}$$

$$\text{Hence } l^2 = \frac{1.5Et\delta}{\sigma}$$

$$l^3 = \frac{E * b * t^3 * \delta}{4p} \dots\dots\dots\dots (1)$$

$$\sigma = \frac{6\ P\ l}{b\ t^2} \dots\dots\dots\dots\dots\dots\dots (2)$$

Where:

P: *is the applied load (N)*

δ: is the deflection (mm)

E: is the Modulus of elasticity (GPa)

b: is the specimen's width (mm)

t: is the specimen's thickness (mm)

l*:* is a selected fixed distance from the clamping jaw and the free end of the specimen, and σ in applied bending stress (MPa).

Example:

From mechanical properties find E, has been used p (Load) ranges between 15-20 (N) in this example used 15N

$$l^3 = \frac{68.9 * 10^3 * 10 * 1.6^3 * 4.25}{4 * 15} = 58.4\text{mm}$$

$$\sigma = \frac{6 * \ 15 * 58.4}{10\ 1.6^2} = 205\ MPa$$

Not: $(205 < \sigma y = 275 MPa)$

Appendix (B)

noc at 263 Mpa

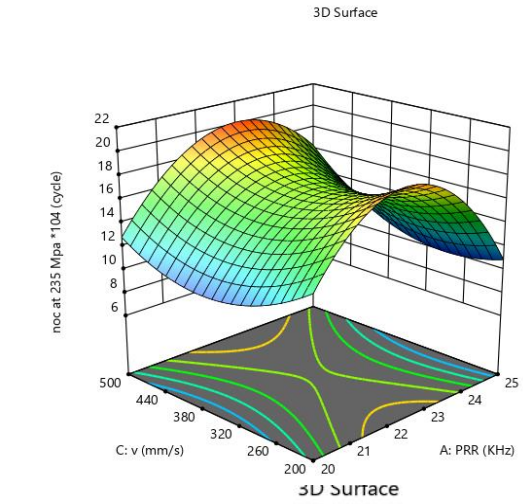

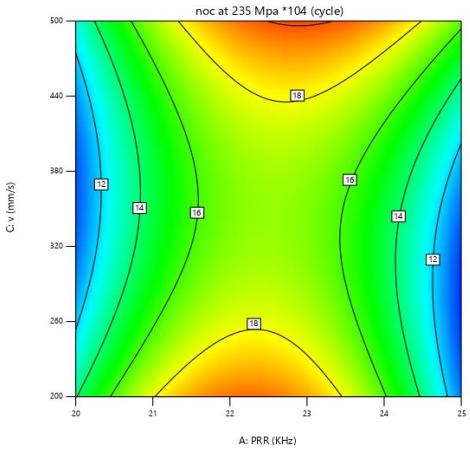

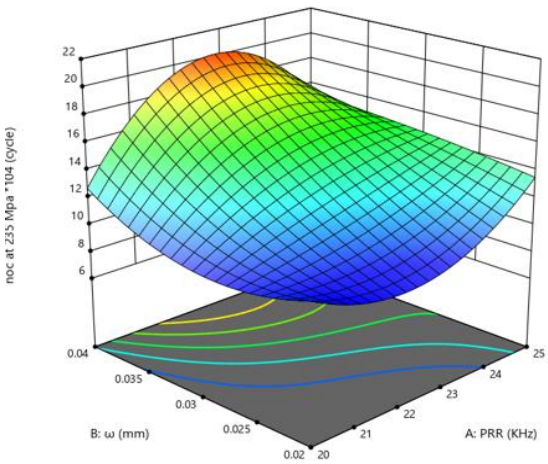

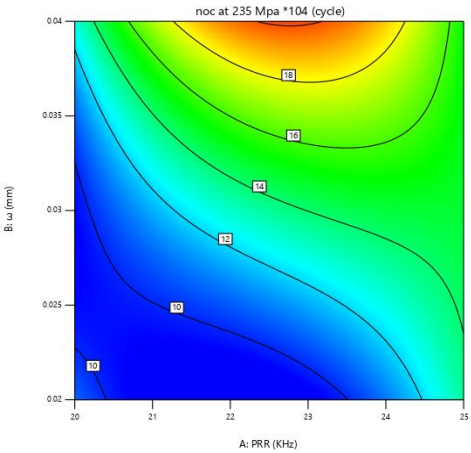

3D Surface

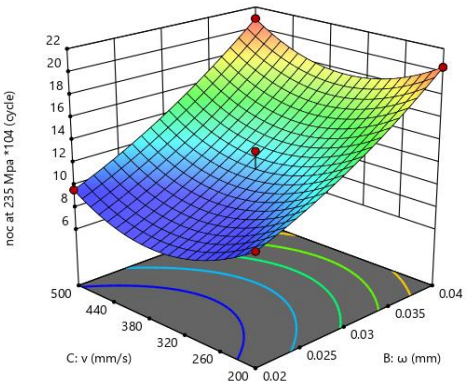

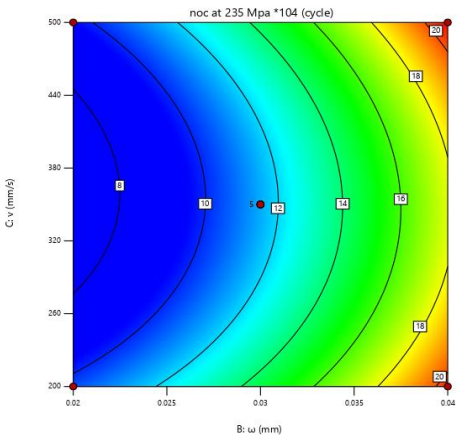

noc at 235 Mpa .

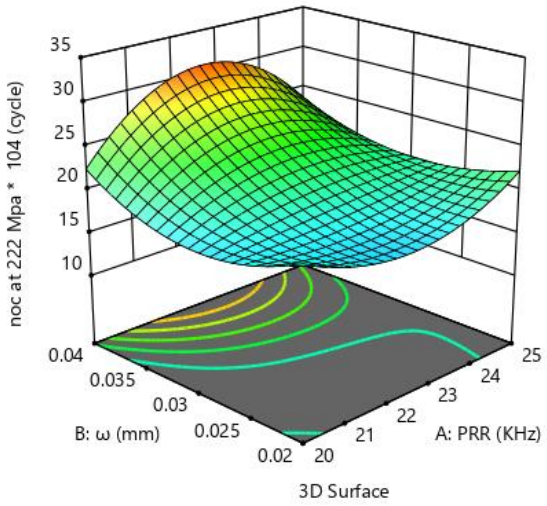

3D Surface

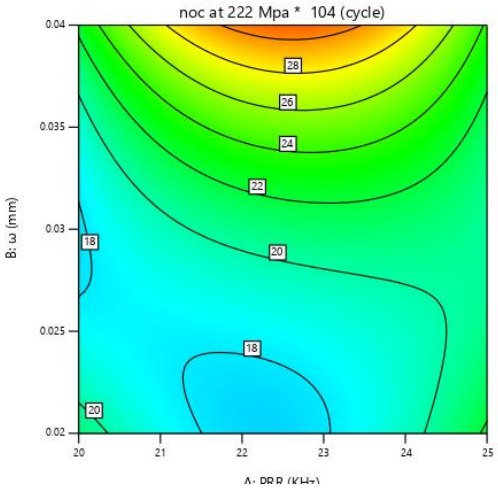

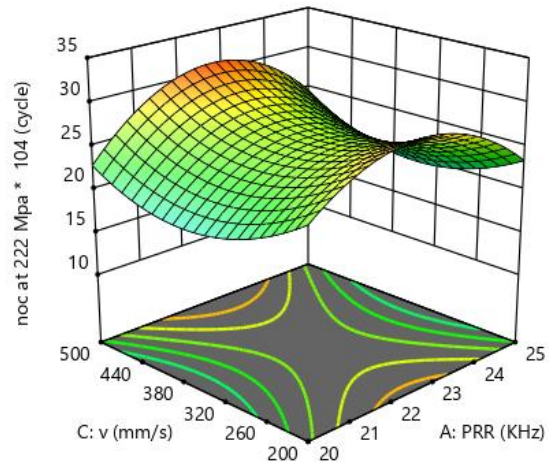

3D Surface

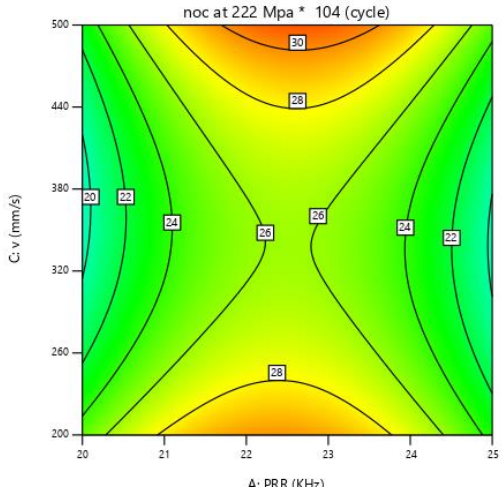

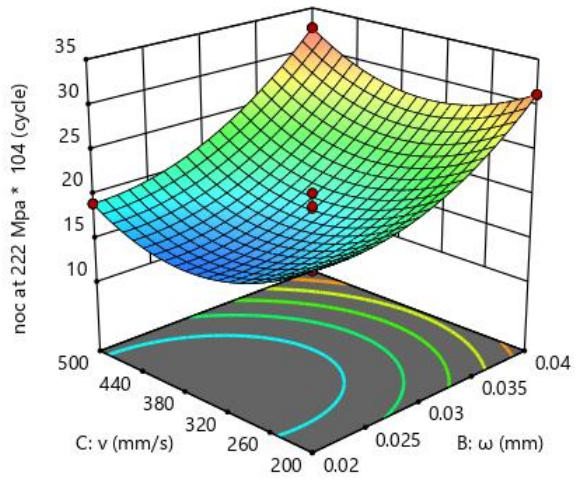

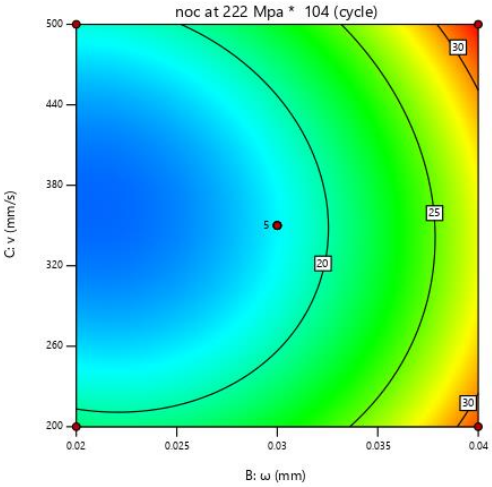

noc at 222 Mpa

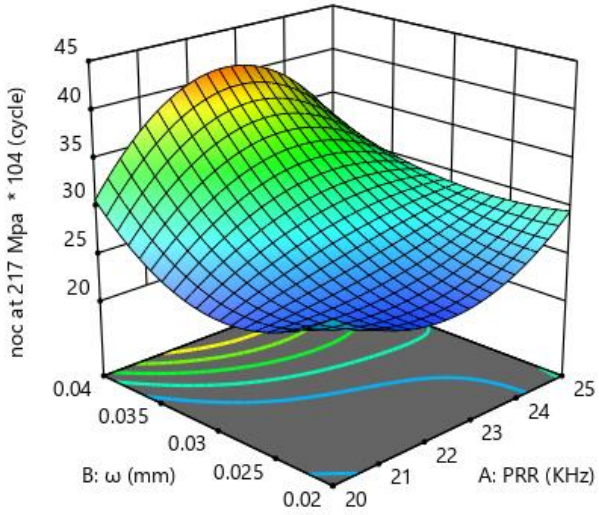

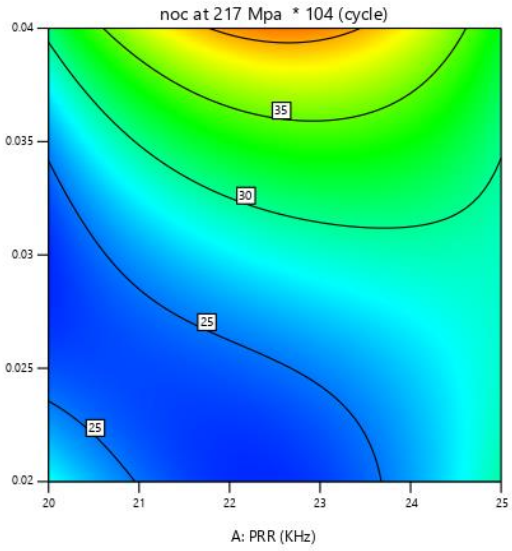

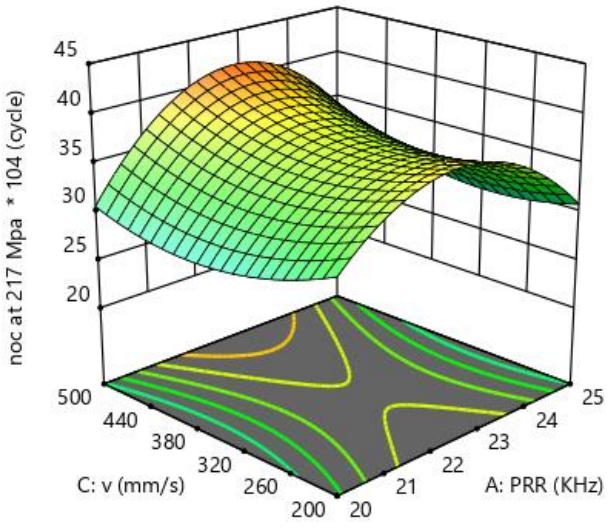

3D Surface

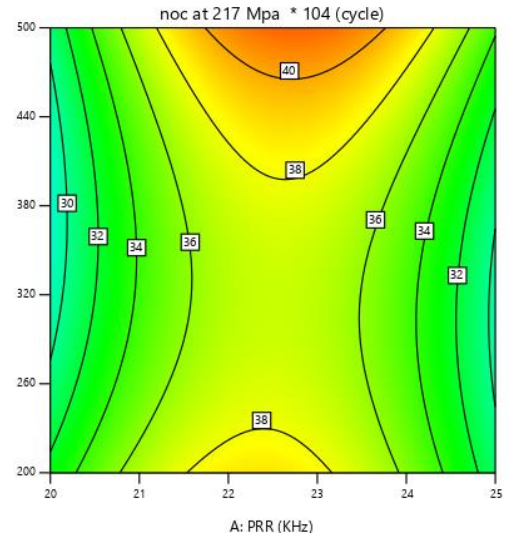

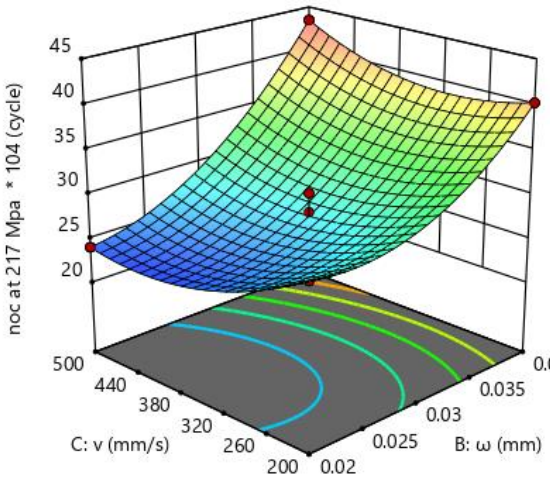

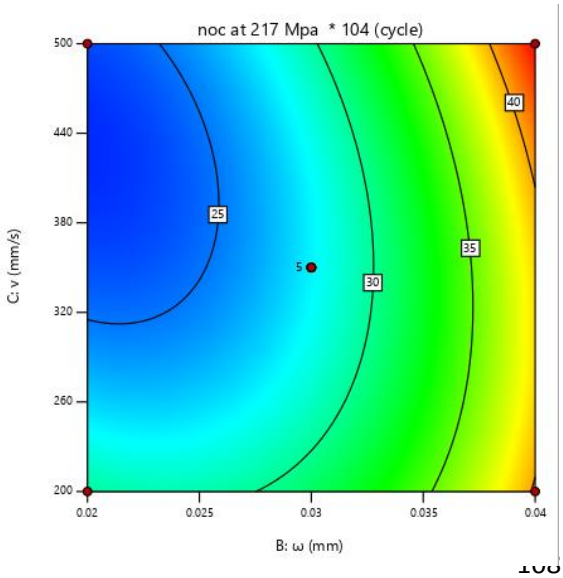

noc at 217 Mpa

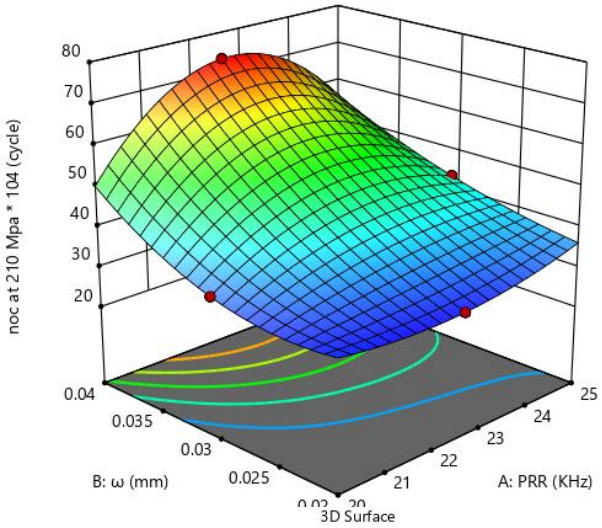

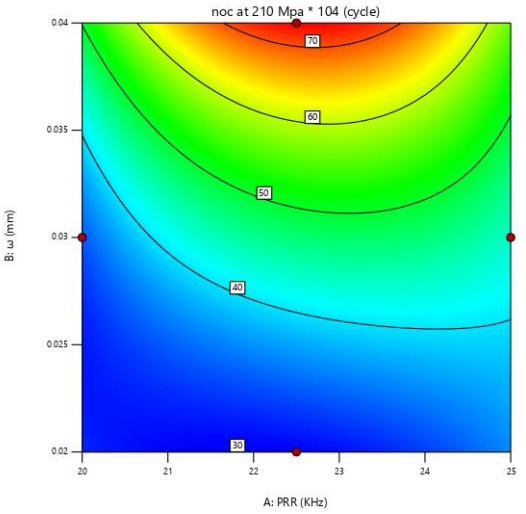

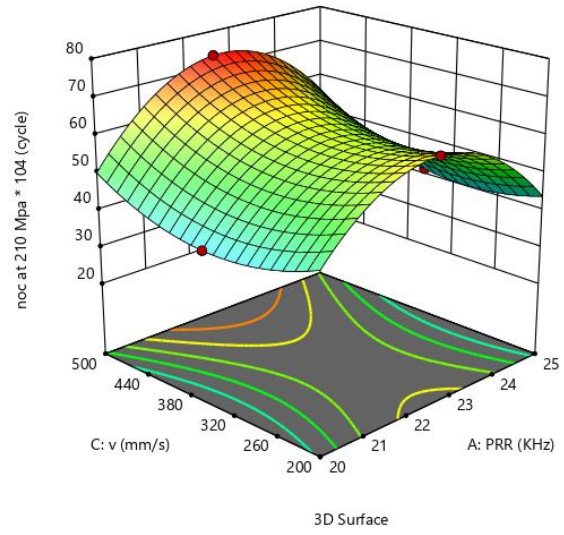

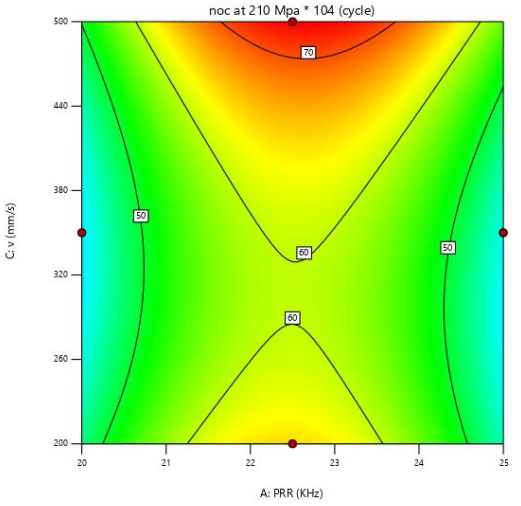

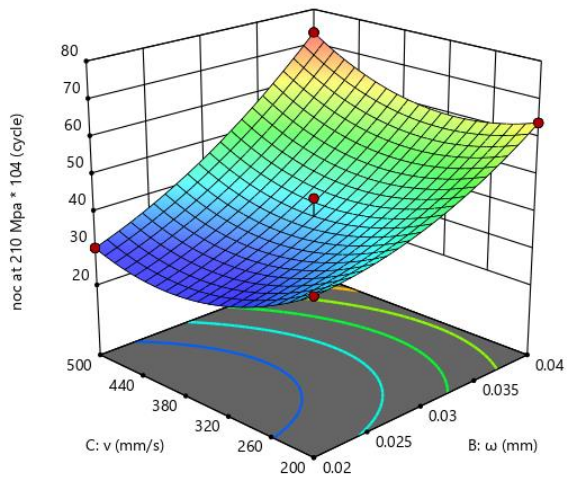

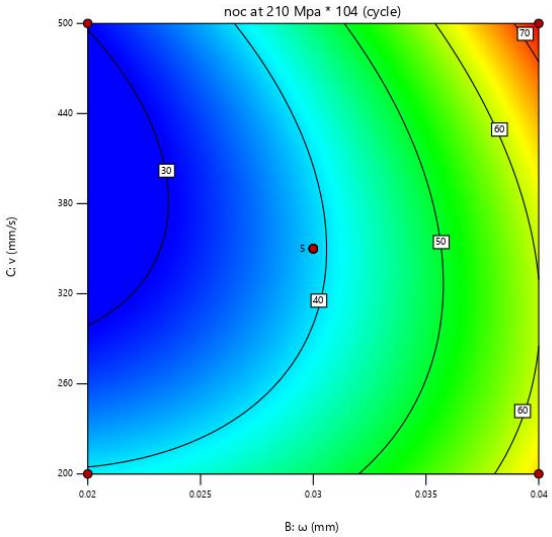

noc at 210 Mpa

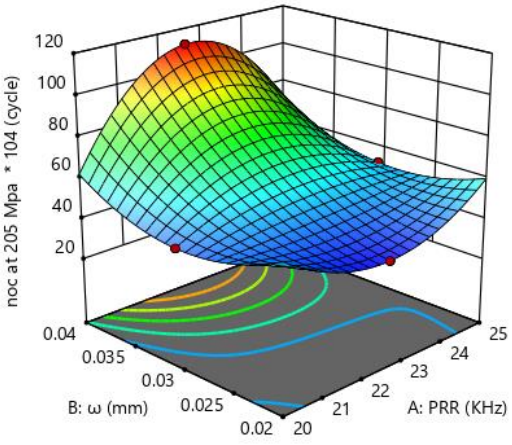

3D Surface

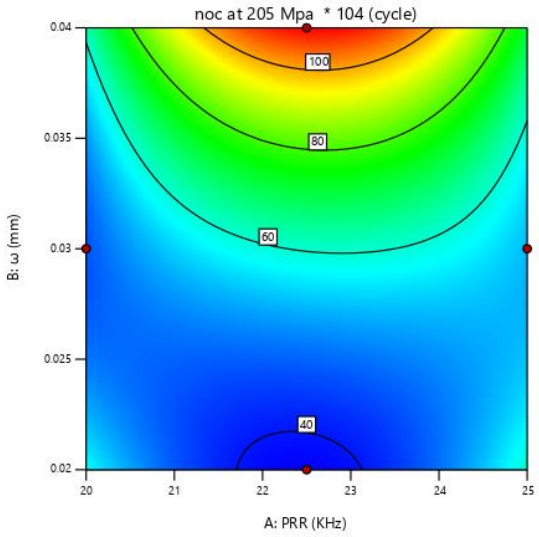

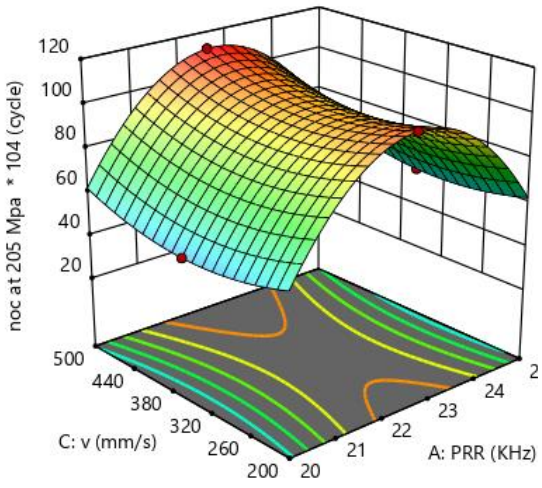

3D Surface

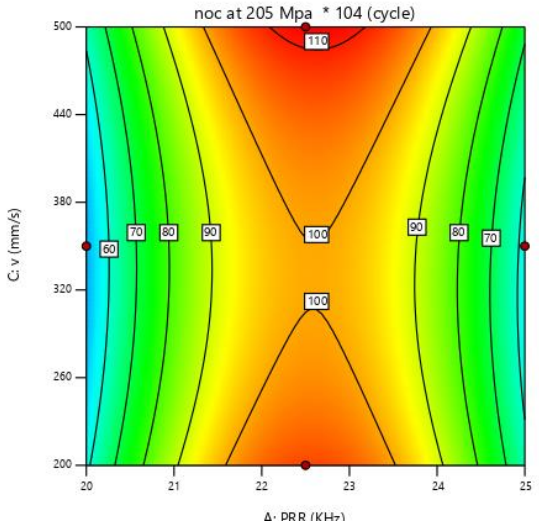

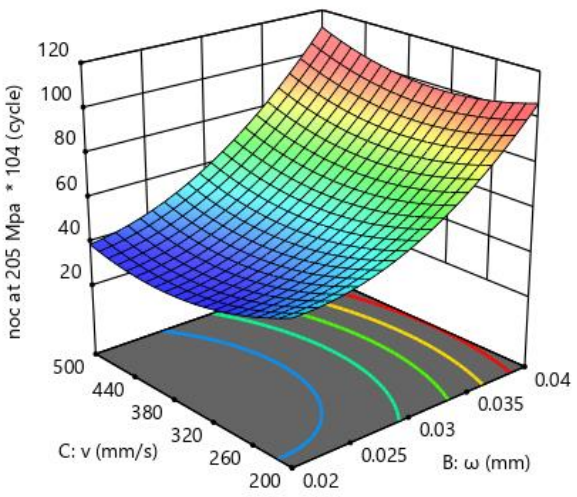

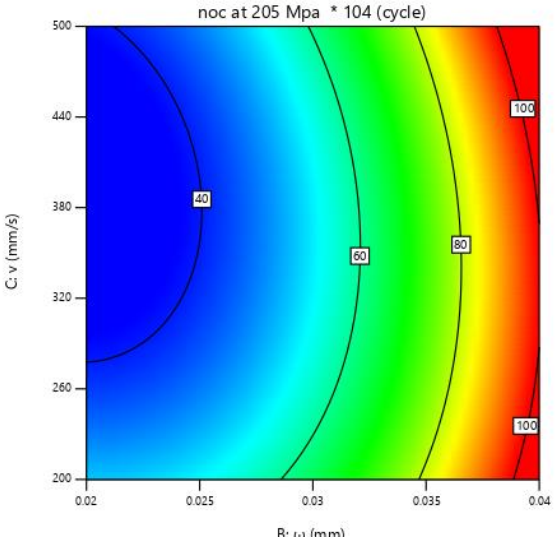

Appendix (C)

[XRDresult sheet]

I :

```
                    ***   Multi Plot  ***

File Name    : 2021\1420
Sample Name  :                          Comment :
Date & Time  : 10-23-09 03:24:53
Condition
  X-ray Tube : Cu(1.54060 A)   Voltage : 40.0 kV   Current : 30.0 mA
  Scan Range : 20.0000 <-> 80.0000 deg   Step Size : 0.0400 deg
  Count Time : 0.24 sec    Slit  DS : 1.00 deg  SS : 1.00 deg  RS : 0.30 mm
```

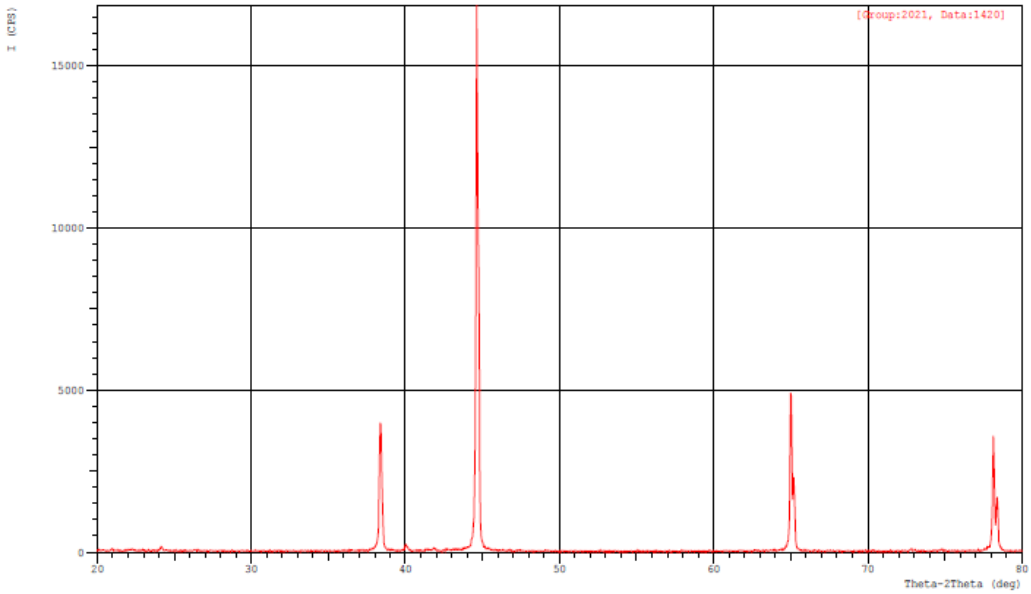


```
          ***  Basic Data Process  ***

Group      : 2021
Data       : 1420

# Strongest 3 peaks
  no. peak    2Theta       d        I/I1   FWHM      Intensity  Integrated Int
       no.    (deg)        (A)             (deg)      (Counts)   (Counts)
   1    2     44.6594    2.02745   100    0.16530       3008       13460
   2    3     65.0402    1.43286    31    0.16690        944        4391
   3    1     38.3999    2.34229    24    0.17710        732        3565

# Peak Data List
      peak    2Theta       d        I/I1   FWHM      Intensity  Integrated Int
       no.    (deg)        (A)             (deg)      (Counts)   (Counts)
        1     38.3999    2.34229    24    0.17710        732        3565
        2     44.6594    2.02745   100    0.16530       3008       13460
        3     65.0402    1.43286    31    0.16690        944        4391
        4     78.1799    1.22165    22    0.17410        674        3320
```

```
         ***  Basic Data Process  ***

# Data Infomation
          Group               : 2021
          Data                : 1420
          Sample Nmae         :
          Comment             :
          Date & Time         : 10-23-09 03:24:53

# Measurement Condition
    X-ray tube
          target              : Cu
          voltage             : 40.0 (kV)
          current             : 30.0 (mA)
    Slits
          Auto Slit           : not Used
          divergence slit     :   1.00000 (deg)
          scatter slit        :   1.00000 (deg)
          receiving slit      :   0.30000(mm)
    Scanning
          drive axis          : Theta-2Theta
          scan range          :   20.0000 - 80.0000 (deg)
          scan mode           : Continuous Scan
          scan speed          :   10.0000 (deg/min)
          sampling pitch      :    0.0400 (deg)
          preset time         :    0.24 (sec)

# Data Process Condition
    Smoothing                 [ AUTO ]
          smoothing points    : 7
    B.G.Subtruction           [ AUTO ]
          sampling points     : 7
          repeat times        : 30
    Kal-a2 Separate           [ MANUAL ]
          Kal a2 ratio        : 50 (%)
    Peak Search               [ AUTO ]
          differential points : 5
          FWHM threhold       : 0.050 (deg)
          intensity threhold  : 30 (par mil)
          FWHM ratio  (n-1)/n : 2
    System error Correction   [ YES ]
    Precise peak Correction   [ NO ]
```

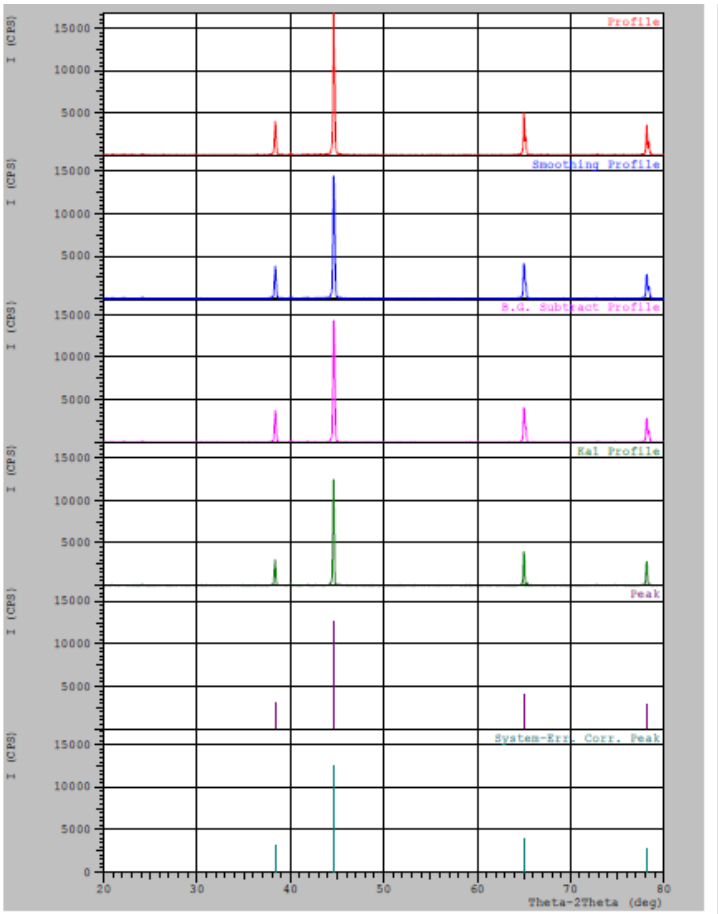

[XRD result sheet]

2-trated metal

```
                    ***   Multi Plot  ***

File Name    : 2021\1419
Sample Name  :                          Comment :
Date & Time  : 10-23-09 03:11:05
Condition
  X-ray Tube : Cu(1.54060 A)   Voltage : 40.0 kV   Current : 30.0 mA
  Scan Range : 20.0000 <-> 80.0000 deg   Step Size : 0.0400 deg
  Count Time : 0.24 sec    Slit  DS : 1.00 deg  SS : 1.00 deg  RS : 0.30 mm
```

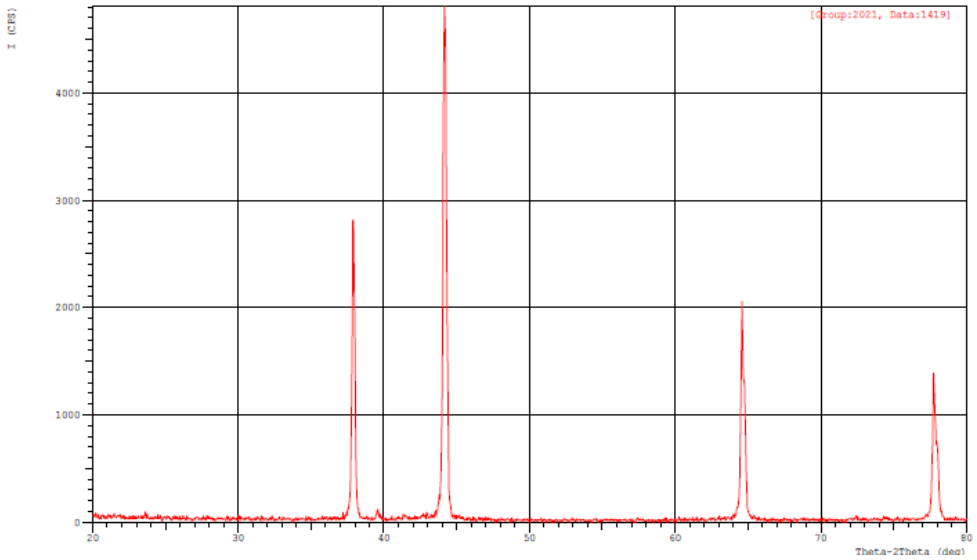

=

```
          ***  Basic Data Process  ***

Group      : 2021
Data       : 1419

# Strongest 3 peaks
  no. peak     2Theta        d        I/I1    FWHM       Intensity   Integrated Int
        no.    (deg)         (A)             (deg)       (Counts)    (Counts)
   1     2     44.1824    2.04822    100    0.25950         840         5906
   2     1     37.9172    2.37099     54    0.22820         454         2797
   3     3     64.6158    1.44124     45    0.23210         376         2461

# Peak Data List
       peak    2Theta        d        I/I1    FWHM       Intensity   Integrated Int
        no.    (deg)         (A)             (deg)       (Counts)    (Counts)
         1     37.9172    2.37099     54    0.22820         454         2797
         2     44.1824    2.04822    100    0.25950         840         5906
         3     64.6158    1.44124     45    0.23210         376         2461
         4     77.7803    1.22693     33    0.23760         279         1896
```

```
        ***  Basic Data Process  ***

# Data Infomation
          Group                 : 2021
          Data                  : 1419
          Sample Nmae           :
          Comment               :
          Date & Time           : 10-23-09 03:11:05

# Measurement Condition
    X-ray tube
          target                : Cu
          voltage               : 40.0 (kV)
          current               : 30.0 (mA)
    Slits
          Auto Slit             : not Used
          divergence slit       :   1.00000 (deg)
          scatter slit          :   1.00000 (deg)
          receiving slit        :   0.30000 (mm)
    Scanning
          drive axis            : Theta-2Theta
          scan range            :   20.0000 - 80.0000 (deg)
          scan mode             : Continuous Scan
          scan speed            :   10.0000 (deg/min)
          sampling pitch        :    0.0400 (deg)
          preset time           :    0.24 (sec)

# Data Process Condition
    Smoothing                   [ AUTO ]
          smoothing points      : 9
    B.G.Subtruction             [ AUTO ]
          sampling points       : 9
          repeat times          : 30
    Kal-a2 Separate             [ MANUAL ]
          Kal a2 ratio          : 50 (%)
    Peak Search                 [ AUTO ]
          differential points   : 9
          FWHM threhold         : 0.050 (deg)
          intensity threhold    : 30 (par mil)
          FWHM ratio  (n-1)/n   : 2
    System error Correction     [ YES ]
    Precise peak Correction     [ NO ]
```

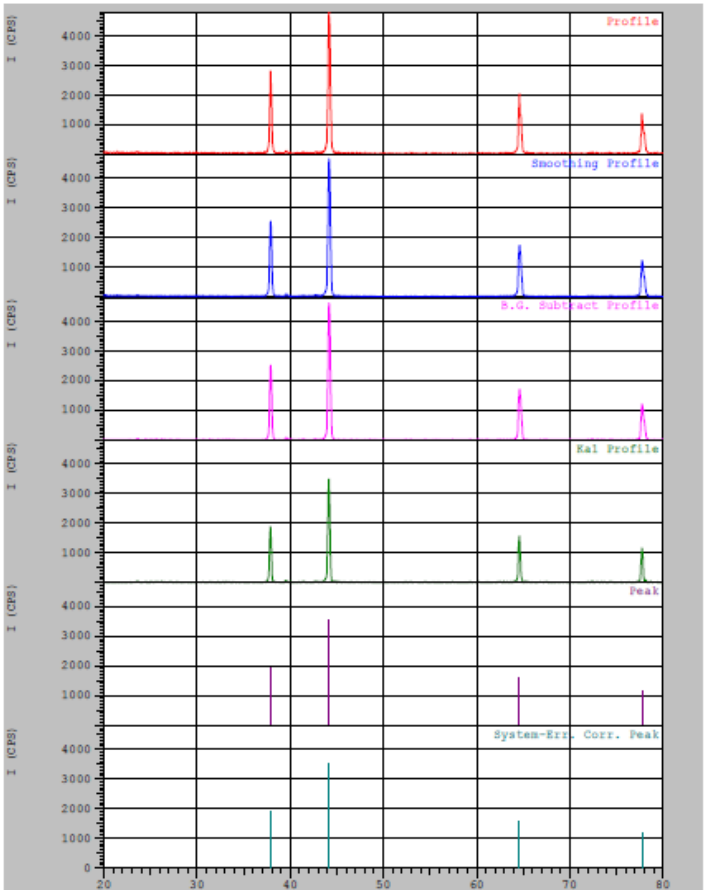

الخلاصة

السفع بالليزر (LSP) هو تقنية لمعالجة سطح المواد على البارد لتحسين خصائصها مثل مقاومة الكلال والتآكل والأنقاص بالحك. وجدت هذه التقنية تطبيقاتها في مجالات مختلفة مثل التوربينات والمراوح وشفرات الضاغط والطائرات ، كما يتم التعامل مع بعض الأجزاء والسيارات. في عملية LSP يتم احداث تشوه دائمي على سطح المادة إلى عمق معين كنتيجة للتفاعل الحاصل بين الليزر والمادة والعديد من الظواهر الفيزيائية المرافقة لها. بعبارات بسيطة ، يغطى سطح المادة بطبقة تضحية والتي بدورها مغطاة بطبقة حبس شفافة لطول الليزر الموجي. يعمل شعاع الليزر ذات الشدة العالية على تبلية الطبقة الماصة للإشعاع مكونًا سحابة من البلازما محصورة بين سطح المادة و الطبقة الشفافة. نتيجة لذلك، تسلط البلازما المتولدة ضغطًا هائلاً على سطح المادة مما يتسبب في تشوه دائمي محلي مسببا اجهادات ضغطية داخلية على طول معين في مقطع المادة.

وفقًا للأدبيات العلمية، تساهم العديد من معلمات عملية السفع بالليزر على جودتها مثل شدة الليزر وطول النبضة والطول الموجة ومعدل تكرار النبضات والشكل الهندسي لبقعة الليزر. الهدف من الدراسة الحالية هو تطبيق تقنية السفع بالليزر على صفائح رقيقة ناعمة من معدن الألمنيوم نوع ٦٠٦١-T6 من أجل تحسين أداء الكلال تحت التحميل الدوري. يتم تطبيق هذه العملية باستخدام ليزر الالياف النبضي ذو الطول الموجي ١٠٦٤ نانومتر. تتمثل حداثة هذا العمل في استخدام ليزر الالياف بحجم بقعة الليزر الصغيرة ٢٠ ميكرومتر وسرعة مسح عالية جدًا في نطاق ٢٠٠-٥٠٠ مم \ ثانية. نظام الليزر المستخدم هو نوع ليزر الألياف النانومتري نوع Q-switched RFL-P (الصين) ذو المواصفات التالية: أقصى متوسط القدرة هو ١٠٠ واط ، وطول نبضة ٨١ نانوثانية ، ومعدل تكرار النبضات من ٢٠ الى ٣٠ كيلو هرتز. لتحسين النتائج ، استخدمت الدراسة تقنية تصميم التجارب (DOE) بناءً على تصميم Box Behnken (BBD) لتحسين نتائج LSP التي يتم إجراؤها بواسطة التقنية التقليدية العامل واحد في كل مرة (OFAT). بالإضافة إلى ذلك ، من خلال تقنية تصميم التجارب ، تم تطوير نموذج احصائي قادر على عرض العلاقة بين معلمات العملية وهي معدل تكرار النبضات (PRR) ، ومساحة بقعة الليزر (ω) ، وسرعة المسح (v) وتفاعلاتها مع بعضها على المخرجات (الاستجابة) . يتم تمثيل الأخير من خلال عدد الدورات (noc) التي تتحملها العينة تحت التحميل الدوري بحمل معين حتى الفشل عن طريق الكسر. يشير النموذج إلى العديد من الخيارات التي يمكن للعمليات أن تتحسن فيها.

تظهر نتائج العينات المعالجة بواسطة السفع بالليزر درجتين من التحسين في عمر التعب يمثلهما عدد الدورات اللازمة لحدوث الكسر مقارنة بالعينات غير المعالجة. يمكن اعتبار الدرجة الأولى طبيعية

لمعظم العينات المعالجة لمجموعات مختلفة من المعلمات حيث تم تسجيل متوسط زيادة في عمر الكلال بنسبة ١٧٥ ٪ تقريبًا. تظهر الدرجة الثانية من النتائج لمجموعتين من العينات حيث تكون الزيادة في عمر الكلال ذات دلالة كبيرة ممثلة بأعلى رقم عند معدل تكرار النبضات يبلغ ٢٢,٥ كيلو هرتز و مساحة بقعة الليزر بمقدار 0.04 مم وكلاهما عند سرعتي مسح لبقعة الليزر عند ٢٠٠ و ٥٠٠ مم \ ثانية. مع هاتين المجموعتين من المعلمات المذكورتين ، تكون النسبة المئوية القصوى للزيادة في عمر الكلال هي ٥٠٥,٢٥٪ عند سرعة مسح تساوي 500 مم \ ثانية و ٤٧٧,٨١٪ عند سرعة مسح ٢٠٠ مم \ ثانية. تُظهر هاتان المجموعتان عينات ذات اسطح خالية من العيوب المختلفة عند تصويرها باستخدام المجهر الإلكتروني الماسح (SEM). يشير تحليل حيود الأشعة السينية (XRD) إلى انخفاض في حجم الحبيبات ، وزيادة في أطوال الانخلاعات بنسبة ٢٨,٥٦٪ ، وتشكيل ضغوط داخلية متبقية فعالة على السطح وتحته الى عمق يصل إلى ٧٠٠ ميكرومتر.

وزارة التعليم العالي والبحث العلمي

جامعة بغداد

معهد الليزر للدراسات العليا

تأثير تغيير معلمات العمل على كفاءة عملية السفع بالليزر على سبيكة الالمنيوم 6061-T6

رسالة مقدمة

إلى معهد الليزر للدراسات العليا / جامعة بغداد كجزء من متطلبات نيل

شهادة ماجستير علوم في الليزر / الهندسة الميكانيكية

من قبل

علي محمد خضير

بكالوريوس هندسة ميكانيكية ٢٠٠٢

بإشراف

أ.م. د. فرات ابراهيم حسين النجار

١٤٤٣ هـ

٢٠٢٢ م